UNIVERSITAT DE BARCELONA

Improving the Reliability of Conductive Atomic Force Microscopy

Jonas Weber

ADVERTIMENT. La consulta d'aquesta tesi queda condicionada a l'acceptació de les següents condicions d'ús: La difusió d'aquesta tesi per mitjà del servei TDX (**www.tdx.cat**) i a través del Dipòsit Digital de la UB (**diposit.ub.edu**) ha estat autoritzada pels titulars dels drets de propietat intel·lectual únicament per a usos privats emmarcats en activitats d'investigació i docència. No s'autoritza la seva reproducció amb finalitats de lucre ni la seva difusió i posada a disposició des d'un lloc aliè al servei TDX ni al Dipòsit Digital de la UB. No s'autoritza la presentació del seu contingut en una finestra o marc aliè a TDX o al Dipòsit Digital de la UB (framing). Aquesta reserva de drets afecta tant al resum de presentació de la tesi com als seus continguts. En la utilització o cita de parts de la tesi és obligat indicar el nom de la persona autora.

ADVERTENCIA. La consulta de esta tesis queda condicionada a la aceptación de las siguientes condiciones de uso: La difusión de esta tesis por medio del servicio TDR (**www.tdx.cat**) y a través del Repositorio Digital de la UB (**diposit.ub.edu**) ha sido autorizada por los titulares de los derechos de propiedad intelectual únicamente para usos privados enmarcados en actividades de investigación y docencia. No se autoriza su reproducción con finalidades de lucro ni su difusión y puesta a disposición desde un sitio ajeno al servicio TDR o al Repositorio Digital de la UB. No se autoriza la presentación de su contenido en una ventana o marco ajeno a TDR o al Repositorio Digital de la UB (framing). Esta reserva de derechos afecta tanto al resumen de presentación de la tesis como a sus contenidos. En la utilización o cita de partes de la tesis es obligado indicar el nombre de la persona autora.

WARNING. On having consulted this thesis you're accepting the following use conditions: Spreading this thesis by the TDX (**www.tdx.cat**) service and by the UB Digital Repository (**diposit.ub.edu**) has been authorized by the titular of the intellectual property rights only for private uses placed in investigation and teaching activities. Reproduction with lucrative aims is not authorized nor its spreading and availability from a site foreign to the TDX service or to the UB Digital Repository. Introducing its content in a window or frame foreign to the TDX service or to the UB Digital Repository is not authorized (framing). Those rights affect to the presentation summary of the thesis as well as to its contents. In the using or citation of parts of the thesis it's obliged to indicate the name of the author.

Tesi doctoral

Improving the Reliability of Conductive Atomic Force Microscopy

Autor: Jonas Weber

Director: Dr. Mario Lanza Martinez

UNIVERSITAT DE BARCELONA

Tesi doctoral

Improving the Reliability of Conductive Atomic Force Microscopy

Memòria presentada per optar al grau de doctor per la Universitat de Barcelona

Programa de doctorat en Nanociències

Jonas Weber

Autor: Jonas Weber

Director: Dr. Mario Lanza Martinez

Tutor: Dr. Juan Marcos Fernandez Pradas

LIBERTAS PERFVNDET
OMNIA LVCE

UNIVERSITAT DE
BARCELONA

This research was carried out in cooperation with the University of Applied Sciences Deggendorf, Germany

Aquesta investigació es va dur a terme en cooperació amb la Universitat de Ciències Aplicades de Deggendorf, Alemanya

Abstract

Owing to its exceptional topographical resolution and electrical sensitivity, Conductive Atomic Force Microscopy (C-AFM) has become an essential tool for nanoscale material analysis. However, achieving reproducible data in C-AFM remains a challenge, primarily due to the multitude of factors influencing the stability of the tip-sample contact. Among these, tip degradation stands out as a particularly critical issue. To attain high topographical resolution, C-AFM probes are designed with small tip radii, but this makes them more susceptible to degradation. Such degradation primarily manifests in two forms. Firstly, since C-AFM measurements are commonly performed in contact mode, mechanical abrasion due to lateral frictions. Secondly, exposure to high current densities, an inherent consequence of the small tip radii, can lead to partial or complete melting of the probe's conductive coating. While the issue of mechanical abrasion has been mitigated to some extent by performing C-AFM measurements in intermittent contact mode – a recent advancement in the field – this thesis concentrates on developing strategies to minimize tip degradation caused by high current densities. To ascertain the current status quo, an in-depth analysis of the degradation dynamics of Pt/Ir-coated Si probes, currently predominant in C-AFM applications, is conducted. In the course of this research, solid Pt probes are examined as a promising alternative. While they exhibit a slightly lower topographical resolution compared to Pt/Ir-coated probes, their superior endurance through numerous scans and enhanced electrical durability are significant advantages. Beyond utilizing more durable probes, another approach discussed in this thesis is the active limitation of resulting currents, such as through software-based current limitation. This technique allows for extended use of metal-coated probes (by approximately a factor of 50, as detailed in Chapter 4.2.1), while also protecting the sample from current-induced damage. However, it is noted that software-based current limitation does not achieve absolute current limitation. A major contribution of this thesis is the introduction of a novel current-limiting sample holder that achieves true current limitation. Unlike software-based methods, this holder restricts currents in both sweep directions through the integration of a MOSFET. This thesis not only deepens our understanding of probe performance in C-AFM but also enhances the reliability and cost-effectiveness of C-AFM studies. Additionally, it opens new avenues for application by providing the ability to precisely control currents during measurements. This is particularly beneficial for analyzing sensitive samples, a need that is becoming increasingly critical with the trend towards smaller device dimensions in recent technology developments.

Resum

Degut de la seva excepcional resolució topogràfica i sensibilitat elèctrica, la microscòpia de força atòmica conductora (C-AFM, per les seves sigles en anglès) s'ha convertit en una eina essencial per a l'anàlisi de materials a escala nanomètrica. Tanmateix, aconseguir dades reproduïbles en C-AFM continua sent un repte, principalment a causa de la multitud de factors que influeixen en l'estabilitat del contacte punta-mostra. Entre aquests, la degradació de les puntes destaca com un tema especialment crític. Per aconseguir una alta resolució topogràfica, les puntes de C-AFM estan dissenyades amb radis molt petits, però això les fa més susceptibles a la degradació. Aquesta degradació es manifesta principalment de dues formes. En primer lloc, com que les mesures amb C-AFM es realitzen habitualment en mode contacte, l’abrasió mecànica causa friccions laterals. En segon lloc, l'exposició a altes densitats de corrent, una conseqüència inherent dels petits radis de punta, pot conduir a la fusió parcial o completa del recobriment conductor de la sonda. Tot i que el problema de l'abrasió mecànica s'ha mitigat fins a cert punt mitjançant la realització de mesures C-AFM en mode de contacte intermitent, un avenç recent en el camp, aquesta tesi se centra a desenvolupar estratègies per minimitzar la degradació de la punta causada per altes densitats de corrent. Per conèixer l'estat actual, realitzo una anàlisi en profunditat de la dinàmica de degradació de les sondes de silici recobertes de platí, que són les més comuns en les aplicacions C-AFM. En el transcurs d'aquesta investigació, examino sondes sòlides de platí com una alternativa prometedora. Tot i que presenten una resolució topogràfica lleugerament inferior en comparació amb les sondes de silici recobertes de platí, la seva resistència superior a través de nombroses exploracions i una durabilitat elèctrica millorada són avantatges significatius. Més enllà d'utilitzar sondes més duradores, un altre enfocament analitzat en aquesta tesi és la limitació activa dels corrents resultants, com ara mitjançant la limitació de corrent basada en programari. Aquesta tècnica permet un ús prolongat de sondes de silici recobertes de metall (incremental la vida útil en un factor al voltant de 50, tal com es detalla al capítol 4.2.1), alhora que protegeix la mostra dels danys induïts pel corrent. Tanmateix, cal assenyalar que la limitació actual basada en programari no aconsegueix limitar la corrent perfectament. Una contribució important d'aquesta tesi és la introducció d'un nou suport de mostres que aconsegueix limitar la corrent de forma gairebé ideal. A diferència dels mètodes basats en programari, aquest suport restringeix els corrents en ambdues direccions d'escombrat mitjançant la integració d'un transistor. Aquesta tesi no només aprofundeix en la nostra comprensió del rendiment de les puntes per a C-AFM, sinó que també millora la fiabilitat de les dades aconseguides mitjançant C-AFM. A més, obre noves vies d'aplicació proporcionant la capacitat de controlar amb precisió els corrents durant les mesures. Això és particularment beneficiós per analitzar mostres sensibles, una necessitat que és cada cop més crítica amb la tendència a dimensions més petites dels dispositius en els últims desenvolupaments tecnològics.

List of content

1 Introduction

The Complementary Metal Oxide Semiconductor (CMOS) transistor - the predominant type of electrical switches used in digital integrated circuit chips - has yielded continual improvements in the performance and cost-per-function of electronic devices over the past four decades (see Figure 1). Nowadays it represents the backbone of modern-day electronics and plays a crucial role in powering a wide range of devices that are integral to modern society, including laptops, smartphones, automobiles, and satellites amongst many more, thereby impacting almost every facet of daily life [1]. As technologies such as Artificial Intelligence (AI) [2], the Internet of Things (IoT) [3], and 5G [4] continue to advance and expand, the demand for increased numbers of transistors is anticipated to persist in the coming years.

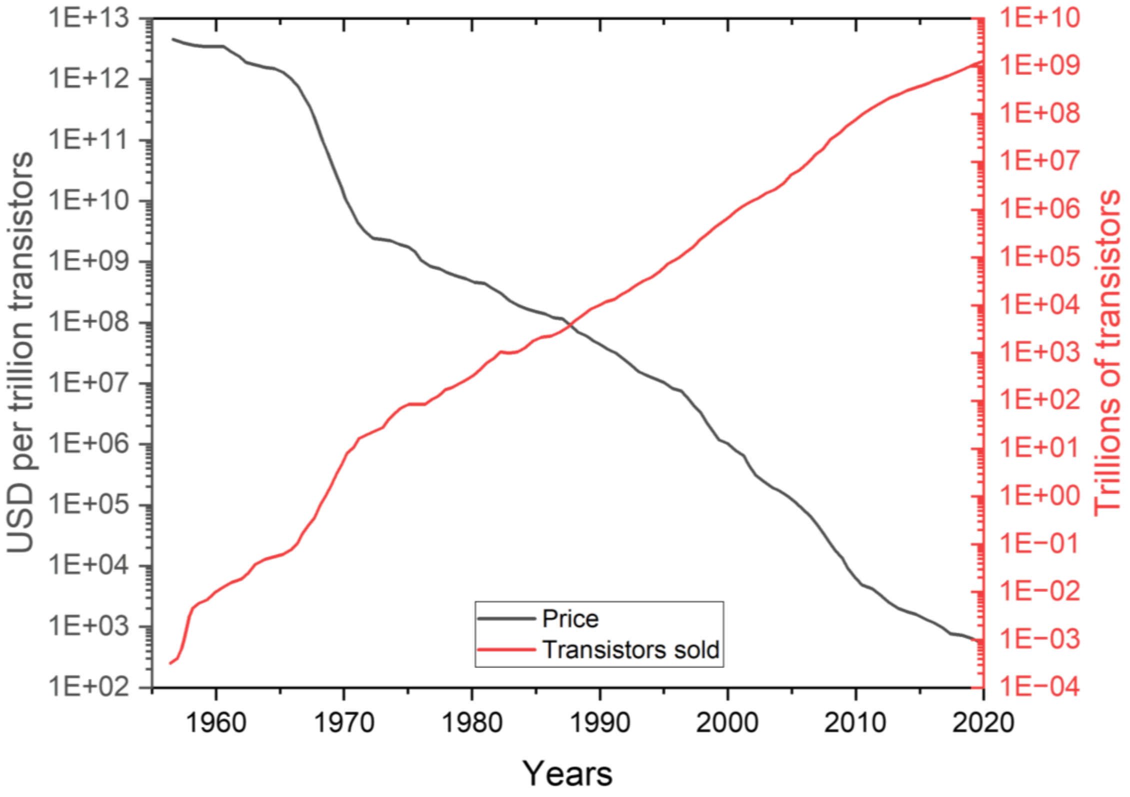

Figure 1: Evolution of transistor pricing and sales volume over the years. Adapted from [5], copyright IEEE Spectrum, 2022.

Beginning as a germanium (Ge) transistor, invented by Walter Brattain, John Bardeen, and William Shockley at Bell Labs in 1947, the evolution of the transistor has been remarkable [6]. It progressed into a planar silicon (Si) MOSFET and later advanced to incorporate Source and Drain regions from strained silicon germanium (SiGe) in the 90 nm and 65 nm technology nodes. The transition continued with the introduction of high-κ/metal gate stacks at the 45 nm and 32 nm nodes, eventually leading to the current state-of-the-art three-dimensional (3D) Fin field-effect transistors (FinFETs), which were introduced at the 22 nm node in 2011. For more than four decades its scaling trend has been following Moore's law, which predicts that the number of transistors per chip roughly doubles every 18–24 months at a constant cost [7]. As device dimensions reduce, the switching speed of the transistor increases. This enhancement is primarily due to the reduced carrier transit time across the diminished channel length. Additionally, this miniaturization allows for a greater number of components to be integrated into a single chip, enhancing its functionality and efficiency (see Figure 2) [8, 9].

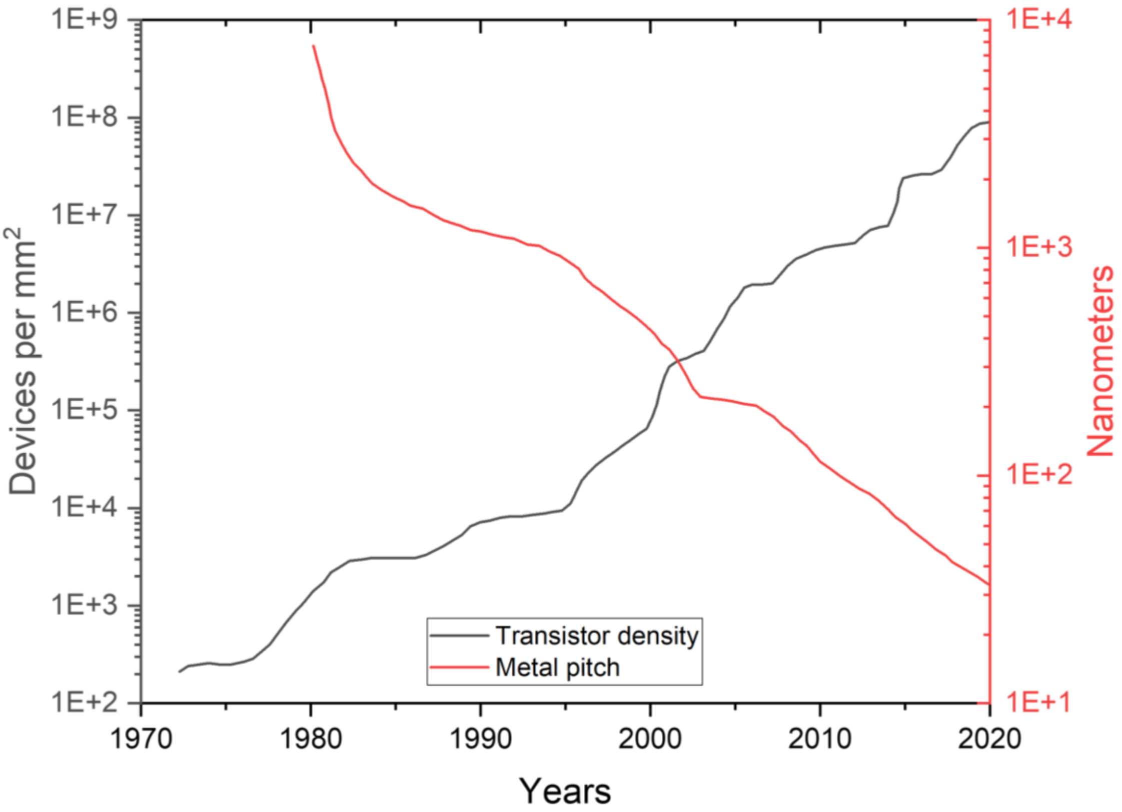

Figure 2: Evolution of transistor density in devices per mm^2 and transistor size, as measured by the metal pitch (the minimum distance between two horizontal interconnects). Adapted from [5], copyright IEEE Spectrum, 2022.

With the gate length of the transistor approaching around 10 nm, however, prohibitively large off-leakage currents between source and drain and increasing manufacturing costs may put an end to transistor scaling. Current estimates suggest that this limitation could be reached in approximately the next 10 years [10].

Consequently, various strategies are being pursued to meet the future demand for high-performance electronic devices. Among these approaches are “More Moore” and “More than Moore”. “More Moore” represents the pursuit of increased transistor density and enhanced chip functionality through traditional miniaturization and scaling methods, by advancements in lithography, new materials, and novel three-dimensional transistor architectures like FinFETs and, more recently, Gate-All-Around (GAA) transistors [11]. “More than Moore” focuses on incorporating additional functionalities like analog, Radio frequency (RF) communications, sensors, and actuators into CMOS technology, which do not necessarily involve making transistors smaller but rather add more capabilities to the chips [10, 12].

Both scenarios point towards a future trend of either smaller or more complex devices, consequently placing greater demands on failure analysis techniques. A prominent contender to keep up with these elevated requirements is Conductive Atomic Force Microscopy (C-AFM). Its capability to monitor topography and electrical resistivity simultaneously and independently with high resolution has promoted C-AFM to an indispensable tool for nano-scaled material analysis and defect analysis [13].

Despite its precision and effectiveness, a major challenge in C-AFM is ensuring data reproducibility. This issue stems from the numerous factors, that contribute to establishing and maintaining a constant tip-sample contact during measurements. A key concern among these is tip degradation [14]. Modern C-AFM probes typically exhibit a tip radius of about 25 nm [15-17], representing a balance between achieving high topographical resolution and maintaining robust electrical conductivity. However, this specification makes them vulnerable to degradation. This degradation can primarily be traced back to two sources. Firstly, since most C-AFM measurements occur in contact mode, mechanical abrasion from lateral frictions is a common cause [18]. To mitigate this, the scientific community has recently shifted towards using intermittent contact mode for measuring local currents [19]. In this mode, the probe tip is retracted during lateral movements, which significantly reduces mechanical wear. The second significant factor is the exposure to high current densities during the application of a bias voltage [18]. C-AFMs are generally used to measure currents above a few picoamperes, the typical noise level, which means the current densities affecting the C-AFM tips are always at least 1 A/cm² [14]. In some experimental scenarios, these densities can escalate substantially, potentially reaching as high as 10^8 A/cm² [20]. This intense exposure can lead to partial or complete melting of the probe's coating, thereby dramatically impacting its electrical conductivity.

Since intermittent contact mode already provides an effective way of reducing tip degradation caused by mechanical abrasion, this thesis focuses on strategies aimed at minimizing tip degradation due to high current densities. The objective is to thoroughly evaluate the extent of degradation experienced by metal-coated probes, which are predominantly used in C-AFM, across various measurement scenarios. Additionally, the potential of alternatives like solid Pt probes and software-based current limitation techniques will be extensively explored. The primary aim is to devise a robust solution that effectively protects C-AFM probes from high current density-induced damage. Ultimately, this research endeavors to advance the C-AFM technique by enhancing its reliability, thereby ensuring more consistent and reliable outcomes in the analysis of nanoscale materials.

To fulfill the objectives outlined above, this thesis is structured into four comprehensive chapters beyond this introduction.

Chapter 2 provides the theoretical background, elucidating the working principles of C-AFM under various measurement scenarios, detailing the manufacturing processe, the key attributes, and the most common degradation mechanisms of C-AFM probes, and introducing an array of electrical tests. It also sheds light on the electrical conduction mechanisms that are crucial to C-AFM research.

Chapter 3 offers a summary of the thesis's objectives, outlines the key findings, and presents a detailed list of the author's publications with specific contributions.

Chapter 4 constitutes the core experimental section, divided into two primary segments: the influence of the tip (Chapter 4.1) and the impact of current limitation (Chapter 4.2). Within Chapter 4.1, there are two subchapters: one conducting an in-depth analysis of the degradation of metal-coated probes (Chapter 4.1.1) and the other rigorously examining the viability of solid Pt probes as a potential alternative (Chapter 4.1.2). Similarly, Chapter 4.2 is split up into two parts. Chapter 4.2.1 delves into the functionality, benefits, and limitations of software-based current limitation, while Chapter 4.2.2 introduces a novel current-limiting sample holder designed to provide true current limitation and thereby effectively shield both the probe and the sample from current-induced damage.

Finally, Chapter 5 culminates the thesis by summarizing the experimental findings and offering an outlook on how these results could influence the future trajectory of C-AFM research.

2 Literature survey

In this chapter, the fundamental operating principles of the AFM are explored. A comprehensive overview of its primary operational modes is provided, and distinctions between the AFM and C-AFM are drawn. Electrical conduction mechanisms inherent to various material classes are elucidated. The specific materials investigated in this thesis are then introduced, and two prominent applications are highlighted. Subsequently, the phenomena of degradation and dielectric breakdown are discussed in detail.

2.1 The Atomic Force Microscopy

On the constant pursue of resolving ever smaller details, the Abbes' Limit represented a significant obstacle that had to be overcome. Abbes' Limit [21] defines the resolution limit for optical systems and can be calculated according to (1) and (2).

$$R_{x,y} = \frac{\lambda}{2 \cdot (\eta_R \cdot sin\,\alpha_l)} \tag{1}$$

$$R_z = \frac{2 \cdot \lambda}{(\eta_R \cdot sin\,\alpha)^2} \tag{2}$$

With λ being the wavelength of light, η_R the index of refraction between point source and lens, relative to free space, and α_l the cone half angle of light from the specimen plane accepted by the objective. The term $\eta \cdot \sin\alpha_l$ is often expressed as numerical aperture (NA). Modern optics exhibit an NA below 1.5, thus, when considering visible light in the UV spectra (e.g., 400 nm) and assuming an NA of 1.4, the resolution limit in the x- and y-direction results in approximately 143 nm, and in the z-direction approximately 480 nm. By using electrons instead of light Ernst Ruska surpassed this limit in 1934 with the invention of the first electron microscope [22]. The first representative of the scanning probe microscope (SPM) family to do so was demonstrated in 1981. By scanning a sharp conductive probe very close to the surface of a conductive specimen and forcing electrons to traverse the gap between them, Gerd Binning and Heinrich Rohrer invented the Scanning Tunneling Microscope (STM) [23]. A schematic is provided in Figure 3 a). In 1986 they were awarded the Nobel Prize in Physics for their invention. When the probe tip approaches the specimen to a distance typically less than 1 nm, there is an overlap between the electron clouds of the foremost atoms of the tip and the surface. Applying a bias between the tip and the surface induces a current due to electrons that are driven to tunnel through the potential barrier from the tip to the surface via the overlapping electron cloud. This tunneling current is highly sensitive to the gap between the probe tip and surface, varying exponentially with the tip-sample distance. STM can be operated in constant height mode and constant current mode [24]. In constant height mode, the tip keeps a predefined distance from the sample. Variations in the tunneling current are recorded based on the x- and y-positions, yielding a spatial map of electronic properties. This mode however requires a flat sample surface. In contrast, constant current mode ensures a steady tunneling current by adjusting the tip height through the system's feedback mechanism, generating a detailed three-dimensional topographic representation. Though STM offers an x- and y-resolution of a few Angstroms and a sub-Angstrom resolution in z-direction, its use is limited to conductive samples only. Moreover, when scanning in constant current mode, it is challenging to determine if alterations in the topography map are genuinely due to the sample's topographical variations or are influenced by factors such as defects or electrically weak sites.

Based on the STM Gerd Binning, Calvin Quate, and Christoph Gerber developed the first AFM [25] in 1986. The corresponding schematic is given in Figure 3 b).

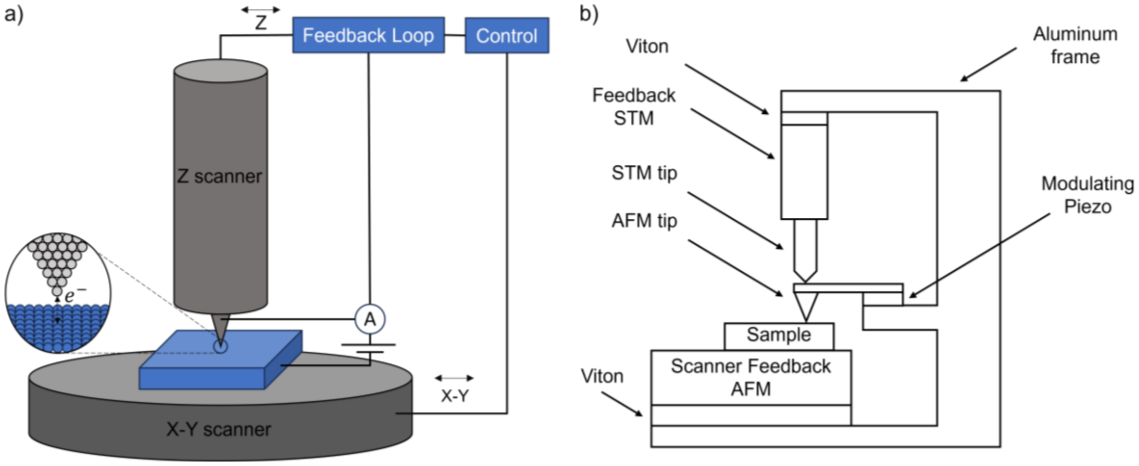

Figure 3: a) STM schematic. b) Schematic of the first AFM by Gerd Binning, Calvin Quate, and Christoph Gerber. Adapted from [25], copyright American Phyical Society, 1986.

In their setup, the AFM tip is positioned between the sample and the STM tip. The cantilever, which supports the AFM tip, is linked to a modulating piezo, enabling it to oscillate at its resonant frequency. The STM tip is connected to a piezoelectric element, which allows to maintain the tunneling current at a constant level. The sample is connected to a three-dimensional piezoelectric drive, the x-, y-, and z-scanner. To minimize mechanical vibrations due to high-frequencies, Viton spacers are employed to decouple cantilever, STM tip, and sample. When the AFM tip encounters a step on the sample, the interaction force between the tip and the sample F_c causes a deflection of the cantilever according to Hooke's law [26] (see (3)).

$$F_c = -k_c \cdot \delta_c \tag{3}$$

With k_c being the spring constant of the cantilever and δ_c the deflection. The associated bending of the cantilever decreases the gap between the STM tip and the cantilever, leading to increased tunneling currents. In response, the feedback system adjusts by retracting the sample and elevating the STM tip by a factor α (which typically ranges from 10 to 1000, with the lower amplitude for the STM tip). These feedback adjustments facilitate the creation of a three-dimensional topographic map, even for non-conductive samples. Reported resolutions in air were 30 Angstroms in lateral and below one Angstrom in vertical direction [23].

Nowadays the most common method to detect cantilever deflection is an optical system [27]. In this setup, a laser beam (originating from the laser source, Figure 4 component 8) is focused through a converging lens (Figure 4 component 6) onto the backside of the cantilever (Figure 4 component 9). Its reflection is then redirected through a mirror system (Figure 4 component 4) towards the center of a photodiode (Figure 4 component 3).

In the absence of any proximity between the tip and the sample (Figure 4 component 7), there is a negligible interaction force, resulting in a static cantilever position, with the laser beam remaining centered on the photodiode. Conversely, when the tip is in close proximity to the sample, the resultant interaction forces cause the cantilever to bend. This bending affects the reflection path of the laser beam, altering its position on the photodiode. By analyzing the shift in position of the laser spot on the photodiode, one can quantitatively determine the force causing such a deflection. Given that the exerted force is a function of the deflection distance as given by (3), one can deduce changes in the topography of the sample under investigation. Following this principle, movement of the AFM tip across the sample surface in x- and y-direction allows for topographic data acquisition across multiple point locations. Such data are then transmitted to a computer (Figure 4 component 1) and converted into a three-dimensional (3D) topographical representation.

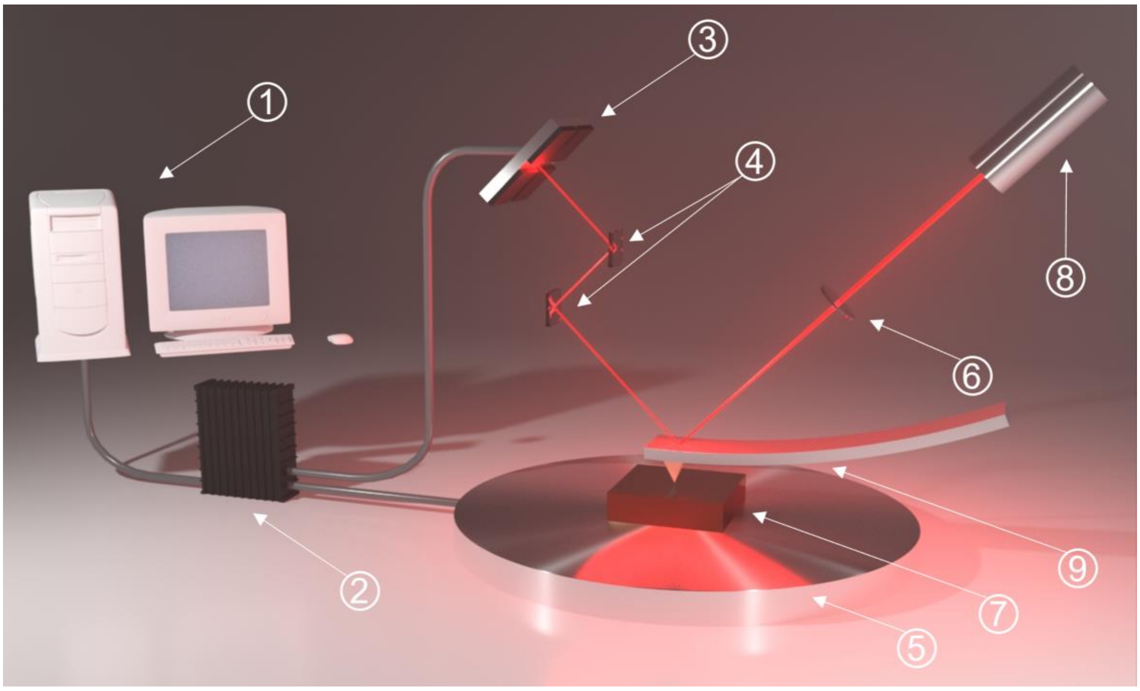

Figure 4: AFM schematic consisting of the following components. 1 Computer, 2 Controller, 3 Photodiode, 4 Mirror System, 5 Piezo tube, 6 Converging lens, 7 Sample, 8 Laser source, and 9 Cantilever with tip at its end.

In this approach, as the tip maintains a constant z-height during scanning, there is a possibility of not resolving deep trenches, or collisions with elevated features on the sample surface. Such collisions could potentially lead to critical tip and/or sample damage. To circumvent these obstacles, the AFM incorporates an electronic feedback mechanism that steadily adjusts the tip-to-sample distance along the z-axis following the height assessment of each pixel within the topographic map thereby ensuring a constant cantilever deflection throughout the whole scan (incorporated in the controller, Figure 4 component 2). The user can define the cantilever deflection, often referred to as the deflection setpoint, individually through the associated software. The movement of the tip and/or sample along the x-, y-, and z-axes is typically facilitated by piezoelectric actuators. A majority of AFMs integrate a piezo tube (Figure 4 component 5), which grants three-dimensional motion capabilities to either the tip or the sample. Additionally, an AFM requires a sophisticated mechanical anti-vibration system to insulate it from external vibrations. Such precautionary measures enable resolutions as precise as 1 nm in the x- and y-axes and 0.1 nm in the z-axis [28]. Based on the tip-sample distance one distinguishes between two different regimes. At distances exceeding 0.5 nm, the predominant forces detected include electrostatic, magnetic, and van der Waals interactions, which collectively contribute to an attractive regime. Conversely, at distances less than 0.3 nm, due to electron cloud overlapping, the tip-sample interaction transitions to a repulsive regime. Within this regime, it is generally accepted that the tip is in physical contact with the sample [29, 30].

2.2 Operation Modes

Based on the previously described force regimes, one commonly distinguishes between the following basic AFM operation modes.

2.2.1 Contact Mode

In contact mode, which operates in the repulsive regime, the AFM tip consistently maintains physical contact with the sample. The predominant approach in this mode is the constant-force technique, where an electronic feedback loop sustains a stable cantilever deflection, resulting in a consistent mechanical force applied to the sample through the tip. The operator can set the deflection setpoint, which determines the cantilever deflection and is typically measured in Volts, reflecting the laser spot's vertical deflection on the photodiode [31]. Although the applied force can be theoretically adjusted and quantified, it requires an elaborate calibration procedure with precise knowledge about the cantilever's spring constant to account for thermal drift and potential inaccuracies in laser alignment. Moreover, factors such as ambient conditions or existing electrical stresses can impact the tip's behavior [32, 33].

In contact mode, striking a balance between reliable tip-sample contact and minimized contact forces is crucial. Lower contact forces reduce lateral friction, which is a primary source of wear and potential damage to both the tip and sample. However, a baseline force is vital to ensure a stable tip-sample contact during scanning. Excessive contact forces during scanning can induce detrimental effects, including nano-scratching on the sample, alteration of the tip's geometry, and/or wear of a potential tip coating. Due to the comparable high forces exerted on the tip and sample, contact mode is not recommended for sensitive samples or fragile tips. Nevertheless, it offers simplicity and, relative to non-contact mode in air, provides enhanced resolution [33, 34].

2.2.2 Non–Contact Mode

In this mode, the cantilever tip is positioned approximately 50–150 Å above the sample surface to sense the attractive van der Waals forces between the tip and the sample [35]. Since these forces are weak (10 – 12 pN) in comparison to the ones within the repulsive regime, the tip is commonly brought into vibration so that changes in amplitude, or resonant frequency because of tip-sample interaction can be monitored instead of classical cantilever deflection [35]. When the amplitude is maintained at a constant level by the AFM's feedback loop, the mode is designated as amplitude modulation (AM-AFM). Conversely, when the resonant frequency is conserved, the mode is identified as frequency modulation (FM-AFM). The paramount advantages of employing this mode include its resilience against tip degradation and its applicability to assessing soft and/or elastic samples, attributed to the minimal forces that are exerted on the sample surface [31]. However, this mode also presents certain limitations, such as a relative reduction in resolution when compared to contact mode [32]. Additionally, the depiction of sample topography may be compromised in instances where rigid surfaces are enveloped in humidity, resulting in representations of the liquid layer rather than the actual surface topography [31]. In ultra-high vacuum (UHV) conditions, this mode has demonstrated the capability to deliver atomic resolution [36].

2.2.3 Tapping Mode

Tapping mode combines the advantages of contact mode and non-contact mode by intermittently allowing the tip to make contact with the surface for high-resolution imaging and then retracting it to prevent surface drag. This technique uses a piezoelectric crystal to oscillate the cantilever assembly close to or at the cantilever’s resonant frequency [37]. It is mostly employed in ambient atmosphere, though successful application in liquid has been demonstrated, too [38]. The induced piezo motion initiates cantilever oscillation in the absence of surface contact. Subsequently, the oscillating tip approaches the surface until it gently "taps" it. During the scanning process, the tip sporadically engages with and disengages from the surface, typically oscillating at a frequency between 50 to 500 kHz. The intermittent contact between the oscillating cantilever and the surface results in energy loss, diminishing the oscillation amplitude which is utilized to identify and gauge surface characteristics. When traversing a protrusion, the available oscillation space for the cantilever is restricted, causing a reduction in oscillation amplitude. Conversely, at a cavity, the cantilever finds more space, leading to an increase in oscillation amplitude, approaching the maximum free air amplitude. The feedback loop maintains the oscillation amplitude of the tip and steadily adjusts the separation between the tip and the sample to ensure constant amplitude and force on the sample [32]. Tapping mode is capable of penetrating liquid layers on the sample surface due to humidity [31] and reduces tip wear caused by lateral friction. It provides comparable resolution to contact mode in air, thus higher resolution than non-contact mode in air [38], and is particularly suited for the investigation of hard surfaces.

2.2.4 Peakforce Tapping Mode

A more recent technique, termed PeakForce Tapping mode, is particularly useful for probing delicate specimens, including carbon nanotubes [39], nanowires [40], or polymer blends utilized in charge transport for organic solar cells [41]. Similar to Tapping mode PeakForce Tapping mode minimizes lateral forces by intermittently contacting the sample. However, in contrast to Tapping mode, it operates in a non-resonant mode with frequencies significantly below the cantilever resonance. This bypasses the filtering effect and the typical dynamics of a resonating system. Peakforce Tapping modulates the AFMs z-Piezo sinusoidal with a frequency of ~2 kHz and a default Peak Force Amplitude of 150 nm to record Force-Distance curves (see Figure 5) at every pixel of the scan. Using a sinusoidal piezo excitation instead of a triangular one, like in regular Force-Distance curves, avoids unwanted resonances at the turnaround points. Continuous force curves can be recorded at 1 or 10 kHz, which facilitates comparable imaging speeds to Tapping Mode. In Figure 5 the upper curve delineates the tip trajectory as it approaches the sample. The black vertical line serves as the zero-force reference, established when the tip is not interacting with the sample. As the tip approaches the sample surface, it encounters long-range van der Waals attraction (A) until such forces surpass the cantilever’s spring constant, causing the tip to snap into contact (B). Post-contact, the interaction is predominantly governed by short-range repulsive forces, culminating in the peak point at the approaching curve (C). As the tip commences unloading, it traverses an adhesion minimum (D), typically induced by a capillary meniscus, before breaking free (E) from the sample surface [42]. The maximum force, which can be specified by the user, is kept constant for each individual pixel of the scan and should be adjusted in such a way that sufficient deformation of the sample is achieved [33, 43, 44].

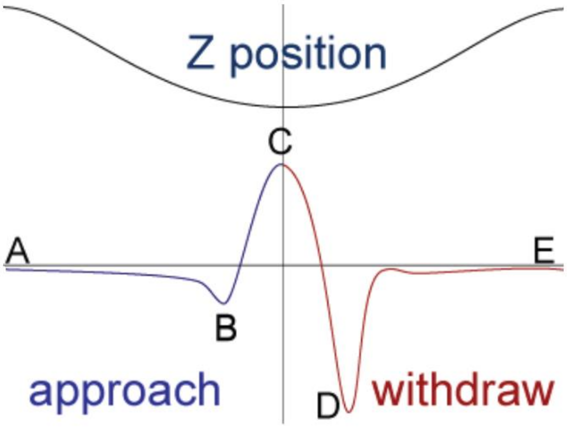

Figure 5: The "heartbeat". Force as a function of time during one Peak Force Tapping cycle. Blue indicates the tip approaching, red the tip retracting and the black curve at the top the z-Piezo extension. . Adapted from [42], copyright Bruker, 2013.

Using the Derjaguin Muller Toporov (DMT) or Sneddon model to analyze the resulting Force-Distance curves allows to additionally extract information about the samples' local adhesion, deformation, or Young's modulus [45, 46]. Peakforce Tapping mode therewith combines the reduced lateral friction of tapping with the direct force control of contact mode. It can be operated using ScanAsyst, a sophisticated algorithm by Bruker to continuously monitor the cantilever deflection signal and adapt deflection setpoint, gains, and scan rate in real-time. This ensures optimum parameters that are dynamically adapted for each pixel of the scan. The result is a high-resolution image with nanomechanical properties at minimum peak force settings [43].

2.3 The Conductive Atomic Force Microscope

In 1993, M.P. Murrel pioneered the first C-AFM by evaporating 100 nm of titanium onto a standard silicon cantilever, utilizing a picoammeter, and a homemade digital-signal-processor-based AFM control system to measure and record currents. This invention was designed to measure tunneling currents across 12 nm thick silicon dioxide (SiO_2)

films [47]. Since then, the C-AFM has undergone continuous improvements [48, 49] and delivered valuable insights into the reliability and breakdown behavior of thin dielectric films [50, 51], the characteristics of resistive switching in transition metal oxides [52-54], or the tunneling and breakdown behavior of 2D materials like hexagonal boron nitride (h-BN) [55-57].

The relentless advancement of commercial high-performance AFM systems has propelled the expansion of C-AFM applications. It now encompasses a wide range of fields including, but not limited to, nanolithography through local oxidation yielding in for example 2 nm organic structures with a periodicity of 6 nm on silicon surfaces [58], biology for example to analyze the modulation of protein conductance with high-resolution compressional force [59], photoelectricity [60], and piezoelectricity [61].

C-AFM is an AFM-based technique that records local electrical and topographical properties simultaneously and independently. It features the same components as a standard AFM with three additions. (i) A voltage source, (ii) a conductive probe tip, and (iii) a preamplifier. The voltage source is usually integrated into the controller and enables applying a potential difference between tip and sample. For the conductive probes nowadays a wide range of material choices is commercially available at competitive prices from manufactures like Bruker [62], Nanosensors [63], or Budgetsensors [64], amongst others. Preamplifiers to convert the analog current signals into computer-compatible digital voltages may be purchased as accessories from the corresponding AFM manufacturer. Depending on the sample C-AFM measurements can encompass current ranges from picoamperes to microamperes. This large dynamic range has led to a differentiation into two classes, C-AFM which covers the sub-nA to µA range and Tunneling AFM (TUNA), which covers the sub-pA to nA range [19]. Therefore, preamplifiers are required to provide high sensitivity and low noise across six orders of magnitude of current. Since standard single-gain amplifiers however cover mostly up to 4 orders of magnitude, logarithmic preamplifiers [65] may be deployed. They offer a broader current range but with a compromise in resolution at lower currents. To overcome this limitation modern preamplifiers feature a multitude of gain settings, or even a combination of two separate amplifiers with different gain settings [66].

In a typical C-AFM experiment, the sample is secured on the chuck using silver paint or carbon tape. Using carbon tape enables an easier removal of the sample; however, it introduces a risk. Due to its inherent softness, carbon tape may permit minor shifts of the sample during the measurements. In contrast, silver paint, once adequately cured, ensures the sample remains stable throughout the experiment. However, the subsequent removal of the sample is more intricate and poses a risk of damaging or fracturing it. When a potential is applied between the tip and the sample in this configuration, it generates an electric field, inducing a current flow either from the sample to the tip or vice versa. The current I follows (4).

$$I = J \cdot A_{eff} \tag{4}$$

J is a measure of the voltage-dependent conductivity of the tip/sample system and is highly sensitive to intrinsic inhomogeneities within the sample such as defects, thickness fluctuations, or doping. A_{eff} represents the effective emission area. Note that A_{eff} does not necessarily equal the physical contact area between tip and sample since the electrical field may also propagate laterally (see also Chapter 2.5.3.) [28].

When a constant voltage is applied between tip and sample while scanning, C-AFM delivers topography and the corresponding locally resolved electrical conductivity for each pixel, also referred to as current map. This enables the correlation of electrically weak locations with topographical features, or the detection of sub-surface defects [67] which are crucial for the reliability of gate oxides in MOSFETs for example. Moreover, C-AFM enables the application of spectroscopic stress tests. In this approach, the tip is positioned at a user-defined location, and typically, either ramped voltage stress (RVS) or constant voltage stress (CVS) is performed. This procedure yields locally resolved I-V or I-t characteristics, providing detailed insights into the electrical behavior of the specified location on the sample [34].

C-AFM is predominantly implemented in contact mode. Beyond its uncomplicated operation, contact mode ensures a continuous and stable tip-sample interaction, which is beneficial for recording currents. However, to circumvent potential damage to the tip or sample due to elevated contact forces and lateral frictions, it can also be combined with PeakForce Tapping mode, subsequently referred to as PeakForce TUNA. Note an application in regular tapping mode is not feasible, since the operation in the resonant regime implies a too short tip sample contact to extract reliable current values. In Peakforce Tapping mode however, due to the operation in the non-resonant regime with frequencies between 1 and 2 kHz, it is a manageable challenge. A general guideline states that the bandwidth of the deployed TUNA module must be 10 times greater than the chosen tapping frequency. Bruker’s Peakforce TUNA module for example offers a bandwidth of ~15 kHz, with gains from 10^7 V/A to 10^{10} V/A while maintaining a noise level below 100 fA on cycle-averaged current. In PeakForce TUNA one differentiates between three different currents, i) Peak current, ii) TUNA current, and iii) contact current. When referring back to Figure 5, Peak current represents the current at point C, which coincides with the Peak Force and therewith represents the measured current at a defined force. Due to possible input lags of the Peakforce TUNA module or parasitic capacitances inherent to the tip sample system, Peak current does not necessarily have to be the maximum current. TUNA current is calculated as the average current throughout a complete tapping cycle, from point A to point E. It encompasses both the current measured while the tip is in contact with the surface and while it is not. Conversely contact current is the average current measured exclusively when the tip is in contact with the surface, ranging from the snap-in at point B to the pull-off at point D [19].

In C-AFM, the voltage typically spans from -10 V to 10 V, with a current range approximately between 1 pA to 10 µA [28]. Though these ranges and the capability to record current maps, and apply RVS and CVS, are sufficient for many experiments, some experiments might require constant current stress (CCS), or broader voltage and current ranges, e.g., when studying the breakdown behavior of thicker dielectric films. For such instances, a semiconductor parameter analyzer (SPA) might be connected to the AFM probe tip to combine the high spatial resolution of the AFM with the sophisticated analysis capabilities of the SPA [68].

2.4 C-AFM Probes and Tip Degradation

A key component to obtain spatially highly resolved topography images is the AFM probe tip. Early AFM works utilized probes constructed from electrochemically etched sharp metal wires or metal foils, with diamond fragments adhered as tips. These manual fabrication methods were cumbersome and yielded significant variability in tip structures, rendering them unsuitable for large-scale production. Thus, batch-processing methodologies were developed. Based on existing techniques Albrecht et al. [69] introduced a batch fabrication method for silicon nitride (Si_3N_4) arrays. They etched an array of square openings in an SiO_2 mask layer over a (100) silicon surface, creating pyramidal etch pits in the silicon surface using potassium hydroxide (KOH) as an anisotropic etchant. Subsequently, the Si wafer was coated with a low-stress Si_3N_4 layer by low-pressure chemical vapor deposition (LPCVD), using the etch pit as a mold to form a pyramidal tip. In the final step, the silicon was etched away so that Si_3N_4 probes were released. A depiction of the process is given in Figure 6 a. The resultant pyramidal tips exhibited high symmetry and a tip radius of less than 30 nm. Wolter et al. [70] proposed methods to batch fabricate single-crystal Si cantilevers with integrated tips. Microfabricated Si cantilevers were first prepared using previously described methods, and a small mask was formed at the end of the cantilever. The Si around the mask was etched by KOH, which caused an undercut of the mask. This resulted in a pyramidal silicon tip beneath the mask, which was then removed. The process is illustrated in Figure 6 b. This method, with further refinements, produced silicon tips in high yield with curvature radii of less than 10 nm [71].

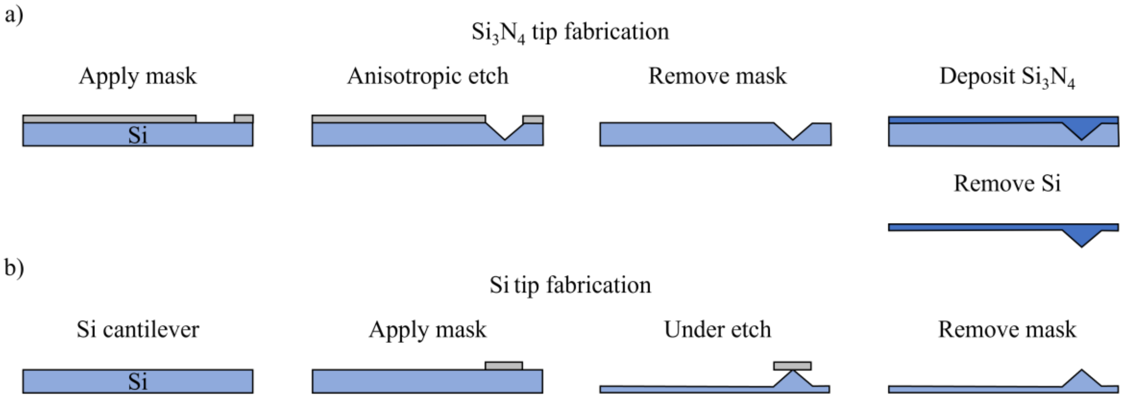

Figure 6: AFM probe manufacturing processes. Adapted from [71], copyright Springer, 2005. a) Si_3N_4. b) Si.

With pure diamond and Si_3N_4 being insulators and Si a semiconductor, one or combinations out of the three following methods could be used to obtain a conductive AFM tip. i) Coating of the previously fabricated AFM probe with a conductive film, ii) replacement of the tip and cantilever material through a conductive one, and iii) conversion of the tip and cantilever material into a (more) conductive one [18]. Coating an existing probe is relatively straightforward, thus etched Si probes coated with various metals (such as gold (Au), silver (Ag), titanium (Ti), or nickel (Ni)), alloys (like titanium nitride (TiN), or cobalt chromium (CoCr)), or carbides (including tungsten carbide (WC), and boron carbide (B_4C)) have already been demonstrated. These materials are typically deposited using sputtering or evaporation techniques. However, introducing an additional material layer, occasionally with an underlying adhesion layer, inevitably enlarges the tip's radius of curvature [18]. The resulting tip radii typically range from 25 nm to

100 nm [62]. Today, the most prevalent metal-coated probes are Si probes with a thin platinum iridium (Pt/Ir) coating [72]. While these metal-coated probes provide excellent conductivity, they tend to wear out rapidly and may experience melting of the conductive layer under high current densities [73, 74]. Chemical vapor deposition (CVD) allows for the growth of diamond layers on AFM probes [75]. However, since diamond layers begin their growth from a seed layer of nanocrystallites [76], a minimum grain size of approximately 100 nm is necessary to ensure a continuous coating. Thus, the resulting tip radii are typically larger than 100 nm [75]. Pure diamond is non-conductive, therefore doping elements have to be introduced during the deposition process. While increasing the number of dopants enhances electrical conductivity, it also reduces the diamond's hardness by decreasing the number of sp^3-bindings [77]. The probe’s resulting conductivity is constrained by the deposition process and is relatively low compared to metal-coated probes. Moreover, it can vary over one order of magnitude [78].

Replacing the tip and cantilever material with a more conductive one usually employs a molding process similar to Figure 6 a, in which the Si_3N_4 is replaced by a conductive material [18]. Through this approach, solid diamond [76] and solid metal [79] tips have been crafted on diamond [18], silicon [80], or metal [81] cantilevers. A critical issue during mold processing of C-AFM probes is ensuring that the deepest part of the etched tip pyramid is completely filled during the thin-film deposition process. Incomplete filling leads to blunt tips with large tip radii [74]. The conversion of the tip and cantilever material silicon into a more conductive one is for example facilitated by the deposition of platinum (Pt) and subsequent high-temperature annealing [18]. This process results in platinum silicide, which exhibits much better conductivity than silicon and higher hardness than pure metal [82].

As illustrated in Figure 7, a conventional C-AFM probe is typically segmented into three components: i) the support chip (1), ii) the cantilever (2), and iii) the probe tip (3). The support chip facilitates manipulating the C-AFM probe with tweezers and ensures the secure attachment of the probe to the AFM’s probe holder. Typically constructed from silicon, it can also be fabricated from other materials such as ceramics. However, to ensure a low-resistance connection from the tip to the clip of the cantilever holder, a conductive coating is usually applied. For ceramic support chips, gold pads are often employed [83]. The cantilever, attached to the support chip at one end, houses the tip at its opposite end. Commonly there is an offset between the tip position and the outer edge of the cantilever. This is helpful to compensate for variabilities within the manufacturing process and supports structural integrity.

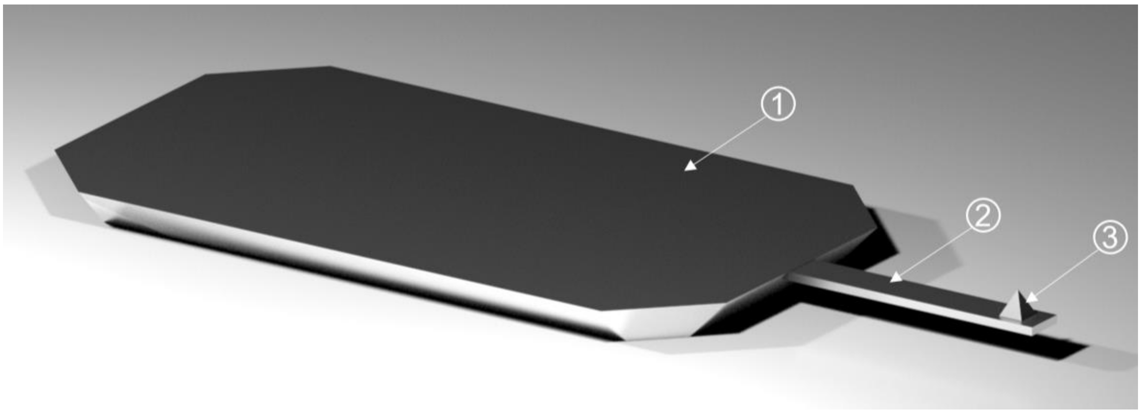

Figure 7: Typical AFM probe schematic consisting of support chip (1), cantilever (2), and tip (3).

When mounted to the probe holder however the top-down optics of the AFM solely provide an image of the backside of the cantilever. Consequently, the exact position of the tip remains speculative, complicating the task of navigating to the area of interest. To address this issue, innovative probes with the tip located directly at the end of the cantilever [84] have been developed (see Figure 8 a). Given the limited range of the AFM photodetector, the cantilever's primary function is the control of the applied contact force. A soft cantilever is comparably easy to bend, causing the laser reflection to utilize the full range of the photodetector at a low contact force already. A cantilever with a stiffer spring constant however, requires higher forces in order to bend and therefore enables larger contact forces. Cantilevers commonly exhibit a beam or V-shape and differ in length, width, and thickness. Their backside is usually coated with a highly reflective material like aluminum to optimize laser reflectivity. Meanwhile the frontside is usually coated with a thin metallic film or highly doped to ensure low resistivity. The contact force must be adapted carefully with respect to the deployed tip and the sample under investigation. Insufficient contact force can lead to unstable electrical contact, while excessive force risks damaging both the tip and the sample [18]. The tip is situated at the end of the cantilever and is ideally shaped like a cone with a hemisphere at its apex. The half-cone angle Θ represents the tip’s capability to trace steep sidewalls, and the tip's radius of curvature, denoted as R_{TIP} and corresponding to the hemisphere's radius, sets the resolution boundary. An AFM image is essentially a convolution of the sample's topography with the tip's geometry. Therefore, a smaller tip radius and half-cone angle are advantageous for distinguishing finer features on the sample surface, see Figure 8 b.

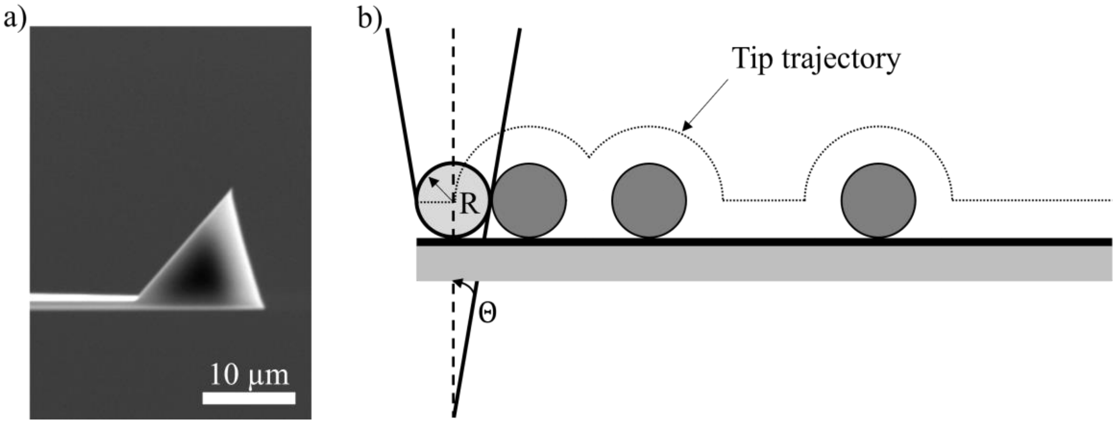

Figure 8: a) Nanoworld Arrow^{TM} UHF probe featuring a tip precisely positioned at the very end of the cantilever. Adapted from [84] copyright NanoWorld®, 2023. b) Impact of the tip’s radius of curvature on the AFM image resolution. Adapted from [30]. copyright Universitat Autònoma de Barcelona, 2013.

C-AFM Probes are commonly affected by multiple types of wear. Though the community has recently implemented C-AFM measurements in Peakforce Tapping mode [19], contact mode remains the prevalent measurement mode. Contact mode necessitates a specific force to establish stable electrical contact between the tip and sample. The optimal force varies based on factors such as sample material, surface roughness, tip radius, tip material, and cantilever spring constant among others. During lateral movements across the sample mechanical abrasion occurs, leading to the removal of tip coating and base material. This results in tip bluntness, potentially causing a decrease in topographical resolution and, in some cases, partial or complete loss of electrical conductivity if the conductive coating is affected [18].

To assess the impact of mechanical tip degradation three Pt/Ir-coated C-AFM probes have been engaged with different contact forces and scanned for a total tip travel distance of 5 mm. Before and after the measurement SEM images of the tip apices were recorded and superimposed to visually highlight the loss of tip material. For the 200 nN scan in Figure 9 a, only minor material removal is visible. The reduction in tip height is less than 10 nm. In the 500 nN scan, see Figure 9 b, the height of the tip apex is reduced by about 40 nm, and in the 1000 nN force scan, see Figure 9 c, by about 130 nm. The larger the contact force, the more tip material is removed [18].

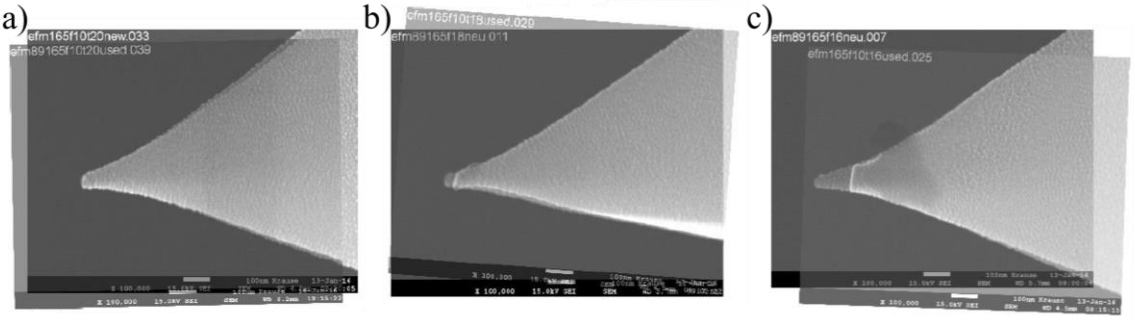

Figure 9: Impact of mechanical degradation on Pt/Ir coated C-AFM probes with different contact forces while scanning a total tip travel distance of 5 mm. Adapted from [18], copyright Wiley-VCH Verlag GmbH & Co. KGaA, 2017. a) With 200 nN. b) With 500 nN. c) With 1000 nN.

Note that that excessive contact forces, in addition to potentially damaging the sample surface, can lead to tip rupture, as illustrated in Figure 10 b. Choosing probes with harder conductive coatings, such as platinum silicide (PtSi) [85] or conductive-doped diamond [86, 87], or entirely made of Pt [88], or conductive doped diamond [89] can help to minimize tip material removal when high contact forces are required. To ensure minimal loss of topographical resolution, particularly when scanning an unknown sample, it is advisable to scan a known reference sample before and after scanning the unknown sample. Comparing the obtained results can help to identify significant deviations.

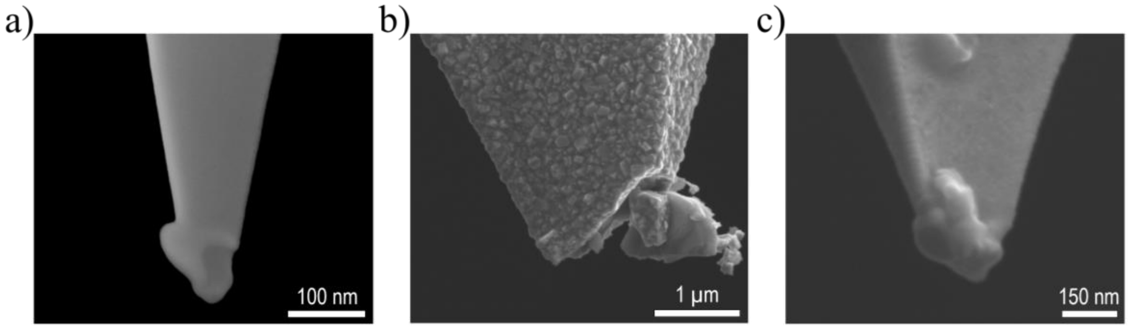

Figure 10: Selected C-AFM tip degradation mechansims. a) Melting of conductive varnish due to high current densities. Adapted from [90], copyright The Royal Society of Chemistry, 2016. b) Mechanical abrasion of tip coating and base material. c) Severe tip particle contamination.

Another degradation mechanism is electrical wear, attributed to the currents that flow between the sample and the tip upon the application of voltage. Due to the relatively small contact area (in the range of 10^{-3} to 10^{-2} μm^2), even low currents in the nano and micro ampere region will lead to substantially high current densities. These elevated current densities can generate exceptionally high temperatures in the tip–sample contact area, potentially causing the conductive coating of the tip to melt [18]. In most C-AFM modules, the voltages and currents are limited (about ±10 V, up to 10 µA) [28]. However, even these limits may already cause tip damage or even the destruction of the tip apex [18].

Consequently, caution is imperative when connecting an external voltage source to the C-AFM [68]. An example of molten off Pt/Ir coating as a consequence of four RVS from -4 to 4 V on a conductive substrate is provided in Figure 10 a [90]. A strategy to reduce the effects of conductive varnish melting as a consequence of high current densities is to deploy probes that feature a more durable coating (PtSi [85] or conductive-doped diamond [86, 87]), or that are made entirely of Pt (see Chapter 4.1.2), or boron doped solid diamond [89]. Note that though boron doped solid diamond probes exhibit exceptional hardness and feature the lowest loss of conductivity per scan, they feature a significantly lower initial conductivity and come at an elevated price [18, 89]. Alternative strategies include limiting the generated currents through software-based methods (refer to Chapter 4.2.1) or employing hardware-based solutions (refer to Chapter 4.2.2).

Moreover, a C-AFM probe may also be contaminated by attached particles [91]. These particles may contribute to an increase in tip radius, subsequently reducing topographical resolution. Additionally, if the particles are insulating, they can diminish the electrical conductivity of the tip. They may originate from airborne debris [92], residues from the sample manufacturing process, or material from the sample that was scratched-off mechanically during tip-sample interaction [93]. An example of an extreme HfO_x particle contamination of a boron doped diamond coated tip is given in Figure 10 c. In cases where the sample surface is unknown, detecting tip particle contamination can be challenging due to dynamic adhesion and removal of particles during the scanning process. Hence, ruling out potential tip particle contamination solely through post-scan SEM analysis of the tip is not feasible [31].

Accurate exclusion of tip particle contamination can only be achieved by in situ SEM monitoring of the tip during the entire scanning process [94]. Occasionally attached particles may be removed by scanning in tapping mode with low amplitude setpoint [31],plasma treatment [95], or scanning samples with sharp features [96].

2.5 Conduction Mechanisms

C-AFM allows the characterization of a wide range of material types. Depending on the material under investigation various conduction mechanisms apply. One commonly classifies the following three scenarios.

2.5.1 C-AFM on Metals

The most basic scenario arises when the C-AFM tip is brought into contact with a metal. Given that metals, under ideal conditions, cannot sustain electrical fields and exhibit a zero voltage drop in all directions [97], the tip is theoretically connected to every point of the sample. Thus, the electrically effective area is equivalent to the entire area of the metallic sample. Measurement scenarios in which the pure metal is directly probed by C-AFM are rather uncommon, mostly a metallic electrode or pad situated on top of a semiconductor or insulator substrate is probed. Analogous to probe-station-based measurements the C-AFM tip then captures the current flowing across the entire region between the electrode and the substrate. However, due to the C-AFM tip featuring a significantly smaller tip radius compared to the probe-station, it can probe nanosized, densely packed electrode arrays, for example, Au-capped nickel oxide (NiO) nanowires [98], which would be unattainable with a probe-station tip. The electron transport between the tip and the metallic sample or electrode follows the principles of electronic transport in metals [99]. When an electric field is applied to a pure metal, charge transport can occur in either a ballistic or diffusive manner, depending on the scale. In the ballistic regime, electrons traverse without scattering, and the resultant current is solely influenced by the conductor's geometry. This ballistic conduction concept is contemporary in micro- and nanoelectronics, describing electron flow in structures like nanowires, carbon nanotubes, two-dimensional materials, and electrically fractured dielectrics, as outlined by the quantum point contact model [100]. However, at larger scales, electron-atom collisions in the material induce scattering, which reduces transmission and leads to the diffusive regime. It's crucial to note that metal conduction is significantly impacted by factors like distorted interfaces, impurities, and various interlayer interfaces [99]. Moreover, the interface between the tip and the sample presents challenges in charge transport. Amongst those are the formation of a metallic heterojunction due to differing tip and sample work functions and the interposition of water molecules and impurities. This can be attributed to factors such as the emergence of a metallic heterojunction due to varying work functions of the tip and sample, and the presence of water molecules and impurities, which can introduce an intermediate layer of uncertain composition and thickness, which significantly raises the resistance at the junction. For instance, Budget Sensors evaluated the contact resistance of their conductive AFM tips (model: ElectriTrap-300-G [101]) on a platinum film. These silicon tips, coated with 5 nm of chromium and 25 nm of platinum, demonstrated resistances of 300 Ω in the best cases [33]. Spectroscopic I-V curves obtained with these tips on conductive samples, generally show linear characteristics, as long as the tip's conductive coating remains intact [102].

2.5.2 C-AFM on Semiconductors

When a metallic C-AFM tip makes contact with a semiconductor, two distinct types of contacts can be identified. A Schottky contact is formed if the metal's work function ϕ_m is greater than the semiconductor's electron affinity χ (for n-type, as illustrated in Figure 11 b,c) or, for p-type, if it is less than the sum of the electron affinity and the band gap E_g. This results in the formation of a depletion barrier within the semiconductor, which works similarly to a diode and establishes a potential barrier between the tip and the base of the sample [33]. If the metal’s work function is lower than the electron affinity of the semiconductor, the conduction and valence bands of the semiconductor bend downward in the contact region (for n-type semiconductors), positioning the Fermi level near the junction even below the conduction band (see Figure 11 d). Conversely, for p-type semiconductors, the conduction and valence bands bend upward, placing the Fermi level near the junction below the valence band. In both scenarios, a depletion region is avoided, ensuring no abrupt transition, and facilitating effective conduction in both polarities. This type of connection is termed ohmic contact [103]. In Figure 11 E_C represents the conduction band, E_F the Fermi level, E_V the valence band, q the electron charge, V_{bi} the build in voltage, and ϕ_B the barrier height. Applying a voltage allows switching between both contact types. If the voltage has the same polarity as the depletion layer (forward bias V_f) an ohmic contact is formed and the current rises exponentially with the voltage (see (6)). On the contrary, when a reverse bias V_r is applied a Schottky contact results and the current is dominated by Schottky Emission [33, 104].

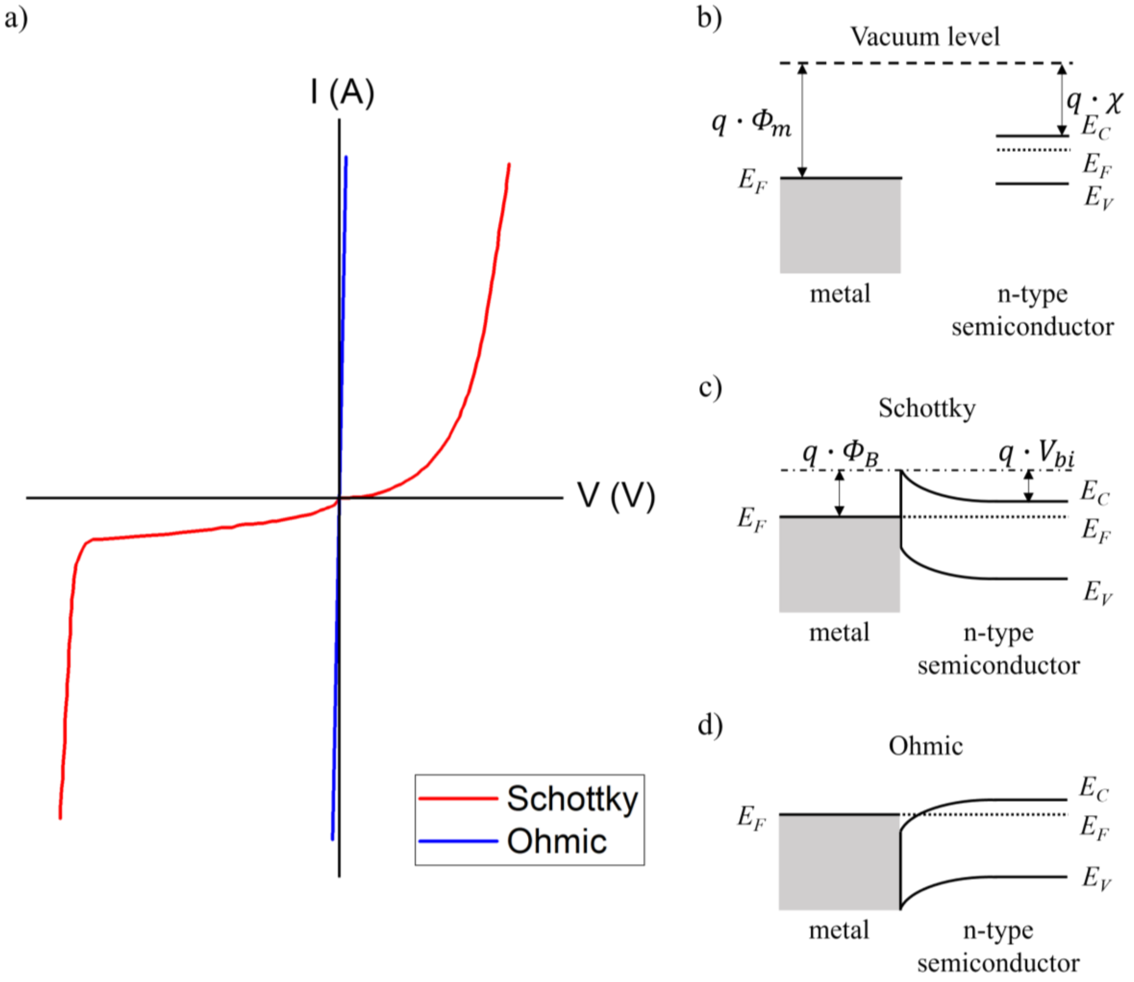

Figure 11: Schematic I-V characteristic of a Schottky contact (red). Adapted from [105], copyright Electronic-notes.com, 2023. Schematic I-V characteristic of an ohmic contact (blue). Adapted from [106], copyright LibreTexts, 2023. Energy band diagrams of metal semiconductor contacts. Adapted from [107], copyright Springer 2001. b) Metal and n-type semiconductor before contact. c) Schottky contact between metal and n-type semiconductor. c) Ohmic contact between metal and n-type semiconductor.

When dealing with an n-type semiconductor, applying a forward bias decreases the barrier by V_f, facilitating easier electron movement compared to the thermal equilibrium state. Conversely, applying a reverse bias heightens the barrier, hindering electron transition from the semiconductor to the metal. For p-type semiconductors, the dynamics are similar, but the polarities are inverted.

Schottky emission is based on thermionic emission, implying that the current is controlled by carriers overcoming the metal-insulator potential barrier. Under forward bias the current rises exponentially according to (5). Under reverse bias the depletion region acts as insulator causing comparatively low currents until dielectric breakdown (see (6) and Figure 11 a) [33].

Schottky
diode
(forward)

$$I = I_0 \cdot \exp\left(\frac{q \cdot V_f}{\eta \cdot k \cdot T} - 1\right) \tag{5}$$

Schottky
Emission
(reverse)

$$I_0 = A_{eff} \cdot A^{**} \cdot T^2 \cdot \exp\left(-\frac{q}{k \cdot T} \cdot \left(\phi_B - \sqrt{\frac{q \cdot E_m}{4 \cdot \pi \cdot \epsilon_s}}\right) - 1\right) \tag{6}$$

$$E_m = \sqrt{\frac{2 \cdot q \cdot N}{\epsilon_s} \cdot \left(V_r + V_{bi} - \frac{kT}{q}\right)}$$

With I being the current, I_0 the Schottky saturation current, q the electron charge, V_f the forward bias, η the ideality factor, k the Boltzmann constant, T the absolute temperature, A_{eff} the electrically effective area, A^{**} the effective Richardson constant, ϕ_B the barrier height, E_m the electrical field maximum, N the doping density of the semiconductor, ϵ_s the permittivity of the semiconductor, V_r the reverse bias, and V_{bi} the built in voltage.

In C-AFM investigations of metal semiconductor junctions, determining the effective contact area (A_{eff}) is more complex than in metal metal or metal insulator interfaces. While extensive research has examined Schottky junctions in C-AFM tip semiconductor interfaces, the focus has primarily been on charge transport, and not on A_{eff}. For many semiconductors, such as silicon, a typically insulating native oxide layer exists on the surface. This layer prevents lateral current spread, confining it to the area directly beneath the tip. However, it's important to note that A_{eff} becomes less critical in semiconductor measurements. This is because the resistivity at the junction can be significantly altered by the inherent properties of the materials involved and the applied voltages [33].

2.5.3 C-AFM on Insulators

The most common scenario for C-AFM investigations is the application on insulating materials, for example on gate oxides for MOSFETs in which high spatial resolution is crucial to ensure electrical integrity [108]. Amongst them are ultra-thin dielectrics [109, 110], high-k dielectrics [111, 112], or two-dimensional dielectrics [113, 114]. In insulating materials, various conduction mechanisms can be observed. The corresponding band diagrams for these mechanisms are provided in Figure 12. q represents the electron charge, ϕ_B the barrier height, d_{ox} the oxide thickness, E_F the Fermi level, E_C the conduction band, and E_V the valence band.

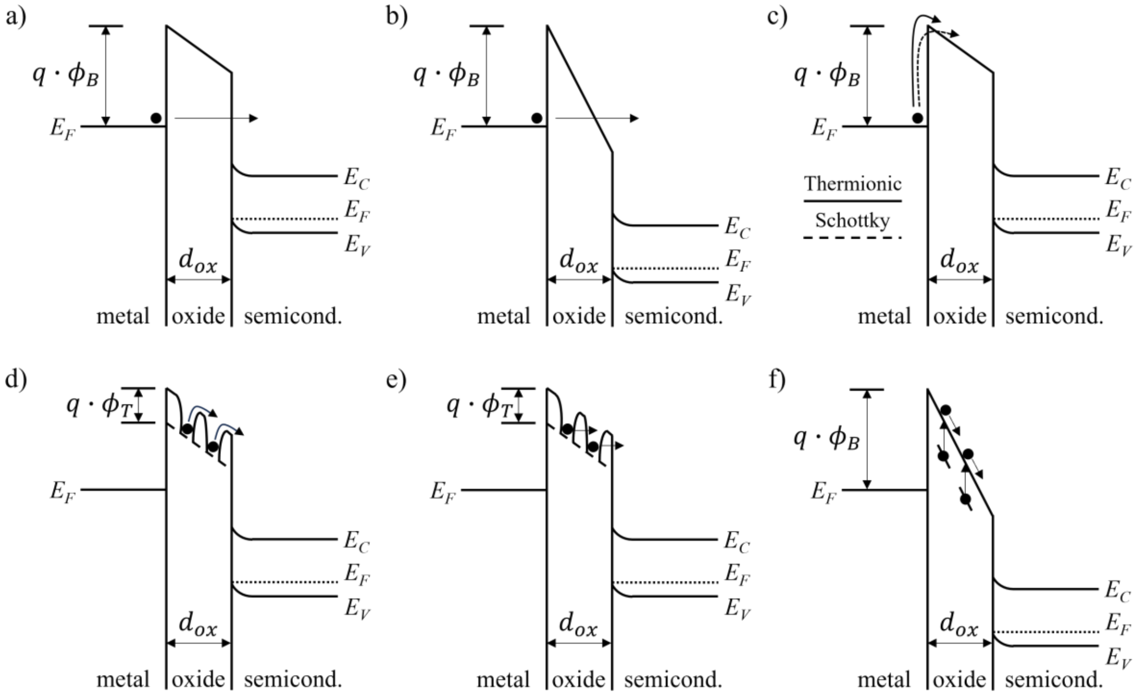

Figure 12: Band diagrams of various conduction mechanisms in MOS structures. Adapted from [115], copyright Fu-Chien Chiu, 2014. a) Direct Tunneling. b) Fowler-Nordheim Tunneling. c) Thermionic & Schottky Emission. d) Frenkel-Pole emission. e) Hopping conduction. f) Ohmic conduction.

For nearly ideal insulators, such as SiO_2, electrical conduction primarily results from tunneling. While classical physics suggests that electrons with energy less than the barrier will be reflected, quantum mechanics predicts that the electron wave function can penetrate through the potential barrier, especially when the barrier is sufficiently thin (< 100 Å). Thus, there is a non-zero probability that electrons will exist on the other side of the potential barrier. Electron tunneling can vary based on the shape of the potential barrier they encounter. Direct tunneling, as illustrated in (7) and Figure 12 a, occurs when electrons tunnel through a rectangular barrier. Conversely, Fowler-Nordheim tunneling, depicted in (8) and Figure 12 b, arises when electrons tunnel through a triangular barrier. When electrons receive thermal excitation to cross a metal-insulator or insulator-semiconductor barrier, it results in thermionic emission, as described by (9) and depicted in Figure 12 c. Schottky emission, as detailed in (6) and also depicted in Figure 12 c, occurs when this thermal excitation is complemented by a barrier reduction due to an external electric field. It's important to note that for insulators, the semiconductor parameters in (6) are substituted with the corresponding oxide parameters. Frenkel-Poole emission, outlined in (10) and Figure 12 d, refers to the release of trapped electrons due to thermal excitation. In contrast, the hopping conduction mechanism, as described by (11) and depicted in Figure 12 e, involves trapped electrons "hopping" from one trap site to another. While both mechanisms involve the release of trapped charge carriers, Frenkel-Poole emission is driven by thermal excitation, whereas hopping conduction results from the tunneling effect. Insulators can also exhibit ohmic conduction, which arises from the movement of mobile electrons in the conduction band and holes in the valence band. Despite the inherently large energy band gap of dielectrics, a minimal number of carriers can still be generated through thermal excitation. For instance, electrons might be excited to the conduction band from either the valence band or an impurity level. While the number of these carriers is limited, it is not negligible. Ohmic conduction is represented by (12) and depicted in Figure 12 f [33, 115, 116].

Direct tunneling

$$\mathrm{I} = \mathrm{I}_{\mathrm{FNT}} \cdot \exp\left(1 - \frac{\mathrm{q} \cdot \mathrm{V}_{\mathrm{ox}}}{\phi_B}\right)^{3/2} \tag{7}$$

Fowler-Nordheim tunneling

$$\mathrm{I} = \mathrm{A}_{\mathrm{eff}} \cdot \frac{\mathrm{q}^3}{16 \cdot \pi^2 \cdot \hbar} \cdot \frac{m_e}{m_{ox}} \cdot \frac{E_{ox}^2}{\phi_B} \exp\left(-\frac{4}{3} \cdot \frac{\sqrt{2 \cdot m_{ox}}}{q \cdot \hbar} \cdot \frac{\phi_B^{3/2}}{E_{ox}}\right) \tag{8}$$

Thermionic emission

$$\mathrm{I} = \mathrm{A}_{\mathrm{eff}} \cdot A^{**} \cdot T^2 \cdot \exp\left(-\frac{q}{k \cdot T} \cdot \left(\phi_B - \sqrt{\frac{q \cdot E_{ox}}{4 \cdot \pi \cdot \epsilon_{ox}}}\right)\right) \tag{9}$$

Frenkel-Poole emission

$$\mathrm{I} = \mathrm{A}_{\mathrm{eff}} \cdot q \cdot \mu \cdot N_{CV} \cdot E_{ox} \cdot \exp\left(-\frac{q}{k \cdot T} \cdot \left(\phi_B - \sqrt{\frac{q \cdot E_{ox}}{\pi \cdot \epsilon_{ox}}}\right)\right) \tag{10}$$

Hopping conduction

$$\mathrm{I} = \mathrm{A_{eff}} \cdot q \cdot \alpha \cdot n \cdot v \cdot \exp\left(\frac{q \cdot \alpha \cdot E_{ox} - \Delta E_{a,t}}{k \cdot T}\right) \tag{11}$$

Ohmic conduction

$$\mathrm{I} = \mathrm{A_{eff}} \cdot q \cdot \mu \cdot N_{CV} \cdot \exp\left(-\frac{\Delta E_a}{k \cdot T}\right) \cdot E_{ox} \tag{12}$$

With I being the electrical current, I_{FNT} the Fowler-Nordheim current, q the electron charge, V_{ox} the voltage across the oxide, ϕ_B the barrier height, A_{eff} the electrically effective area, ħ the reduced Planck's constant, m_e the free electron mass, m_{ox} effective charge carrier mass in the oxide, E_{ox} the electrical field across the oxide, A^{**} the effective Richardson constant, T the absolute temperature, ϵ_{ox} the permittivity of the oxide, μ the charge carrier mobility, N_{CV} the density of states, α the mean spacing between trap sites, n the electron concentration in the conduction band of electrons at trap sites, v the frequency of the thermal vibration of electrons at trap sites, $\Delta E_{a,t}$ the carrier activation energy from trap states to the bottom of the conduction band, and ΔE_a the carrier activation energy.

The current flow in tip insulator junctions is next to the conduction mechanism strongly dependent on the electrically effective area. Ideally, the contact area between the tip and sample A_c should match the electrically effective area A_{eff}. However, in actual measurement scenarios A_{eff} can deviate significantly from A_c. One reason for this discrepancy is the presence of humidity, which can lead to the formation of a water meniscus around the tip when the measurements are performed under ambient conditions (see Figure 13) [117].

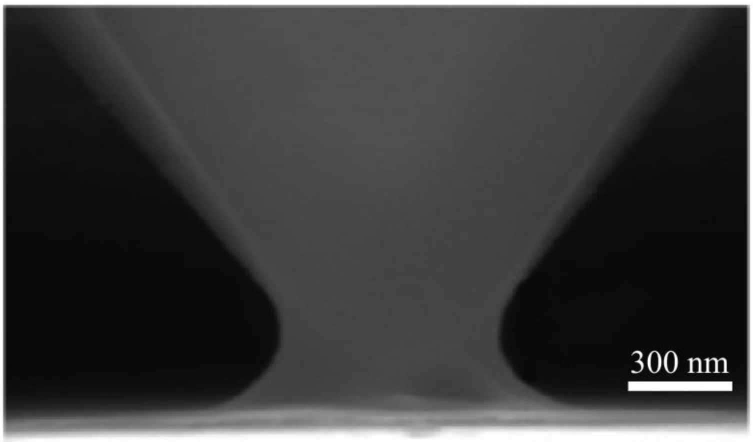

Figure 13: Environmental SEM image of a water meniscus surrounding an AFM tip. The image was recorded at 5° C with 60 % RH. Adapted from [117], copyright American Chemical Society, 2005.

Depending on deployed tip model, applied contact force and sample under investigation typical effective emission areas of the order 30-300 nm^2 were reported [49, 51, 118]. Considering a 3 nm thick water film on a 5 nm thick oxide layer and a tip with a radius of 50 nm, the maximum of the electric field creates an almost flat region with a diameter of about 30 nm at the center of the field distribution. Assuming that electron emission is solely confined to this area, A_{eff} was calculated to be approximately 700 nm^2 [119]. However, a 3 nm thick water film might be an overestimation, Heim measured water film thicknesses in the range of 0.2 nm to 0.4 nm for relative humidities from 25 to 44 %. Even at 80 % relative humidity the water film thickness was typically found to be below 0.5 nm [120]. Hence the effect on the electrically effective area may be less severe. In addition, the water film might not evenly coat the entire samples surface [31]. However the water film may interact as catalyst for dynamic electrochemical reactions that might alter the surface and tunneling behavior of tip and sample [119]. It is therefore essential to conduct multiple measurements before a conclusion is drawn.

To avoid the water layer and therewith enhance electrical resolution, one can measure in ultra-high vacuum (UHV) [121]. However, in UHV, the absence of the water layer means there is no lubrication, causing the tips to wear out faster [33]. This results in enlarged tip radii and, eventually, a partial or complete loss of the tip's conductive coating. Additionally, C-AFM systems designed for UHV operation are less productive (due to prolonged pumping times), more complex, and come at a higher cost.

Other dynamic factors that affect the tip sample junction are air borne debris [92], particles from tip and sample that were scratched off during the scanning process and subsequently picked up by the tip [93], asperities of the tip and the sample [122], wear of tip and conductive coating (which also occurs in air with lubrication due to humidity) [123], local oxidation due to electrical stress [124], and local penetration of thin oxides [125] and phase transitions as a consequence of large contact forces [126]. In summary, despite its versatility and high spatial resolution, the reliability of AFM based measurements (C-AFM included) is strongly dependent on the condition of the tip sample junction throughout the entire measurement. Thus, developing strategies to reduce tip wear is crucial and urgent.

2.6 Degradation and Dielectric Breakdown

As device dimensions continue to shrink, the impacts of tunneling, inhomogeneities, and local defects on device performance and reliability become increasingly significant. Originally designed to analyze and understand these effects in thin oxides, the C-AFM, with its high lateral resolution, remains a favored instrument for studying them until today, not only in thin oxides but also in emerging 2D dielectrics, such as hexagonal boron nitride (h-BN) [127].

2.6.1 Dielectric Breakdown and Resistive switching

Among these effects is the dielectric breakdown. Dielectric breakdown arises as a consequence of the high electric field that results when voltage is applied to a MOS sample. It may occur gradually or instantaneously, leading to the degradation of the oxides' dielectric properties and ultimately to a dramatic increase in system conduction (breakdown) [31]. Traditionally dielectric breakdown was considered to be irreversible and therewith a purely negative phenomenon [30]. However, it was discovered that SiO_2 was occasionally capable of regenerating a dielectric breakdown if the current through the oxide was limited [128, 129]. The materials' property of cyclically changing its electrical resistivity between at least two stable states is called resistive switching [130]. Known since the 1960s [131], resistive switching is of particular interest for its potential in data storage applications, as it enables the encoding of logical states, such as binary ones and zeros, into corresponding resistive states. Since these early observations of resistive switching however were not robust enough for this type of application not much attention was given to this phenomenon until the late 1990s when the hysteresis of I-V characteristics in perovskite oxides was discovered [132, 133]. In 2004 Samsung demonstrated nickel oxide (NiO) RRAM arrays integrated with 180 nm silicon CMOS (Complementary Metal-Oxide Semiconductor) technology [133] and therewith triggered massive research interest in resistive switching of binary oxides like NiO [134], titanium oxide (TiO_x) [135], copper oxide (CuO_x) [136], zirconium oxide (ZrO_x) [137], zinc oxide (ZnO_x) [138], hafnium oxide (HfO_x) [139], tantalum oxide (TaO_x) [140], aluminum oxide (AlO_x) [141], and many more. The simplicity of these materials, coupled with their compatibility with existing CMOS processes, has been a driving factor in the continued exploration of their potential [133]. With ongoing research efforts resistive switching has meanwhile also been demonstrated in polymers [142] and 2D materials [143]. Resistive random-access memory (RRAM), based on resistive switching, is a prominent contender in the next generation of non-volatile memory technologies [30]. It offers several advantages, including a straightforward architecture, rapid switching speeds, excellent scalability, and low power consumption [144]. Moreover, its compatibility with standard CMOS processes [133] makes it an attractive option for the development of devices that transcend the limitations of Moore's Law [145].

2.6.2 Defect Generation and Accumulation

It is widely accepted that the process of the dielectric breakdown can be described with the percolation model [146]. One commonly distinguishes between three stages. Initially, defects are generated within the oxide bulk and at the silicon interface due to the electrical stress applied. Subsequently, these defects accumulate, forming a localized conductive path through the insulator. Finally, this path facilitates a high current flow, which releases energy into the adjacent material, dictating the extent of the dielectric breakdown's severity [147]. A schematic is provided in Figure 14.

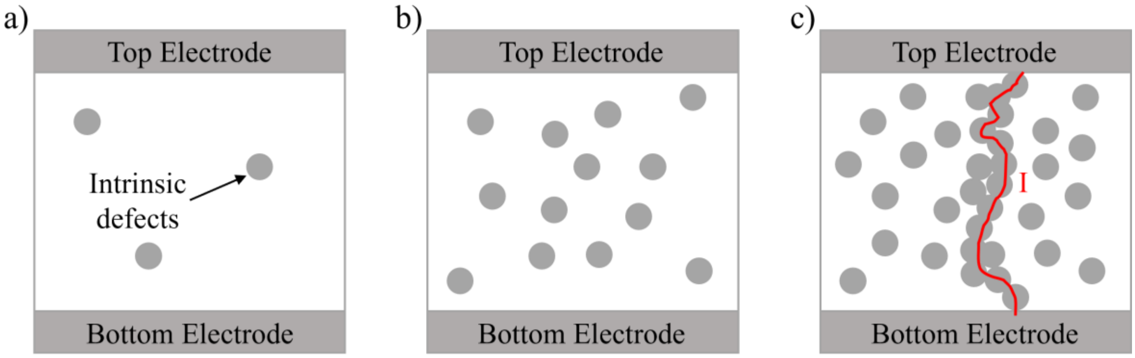

Figure 14: Dielectric breakdown formation according to the percolation model. a) Initial state of a metal-oxide-metal test structure. b) Electrical stress leads to a random formation of defects within the oxide. c) Accumulation of defects results in a conductive path (percolation path) that bridges top and bottom electrode and therewith causes dielectric breakdown.

With respect to the defect generation model there is less unity [31]. Dielectric breakdown can result from several mechanisms, including field-enhanced bond breaking (E-model) [148], impact ionization (1/E-model) [149], anode hole injection (AHI) [150], and anode hydrogen release (AHR) [151]. Neutral electron traps, interface states, hole trapping and hole-related defect generation are well-known consequences of electrical stress and are also linked to dielectric breakdown [152, 153]. The E-model and the inverse E-model (1/E-model) are two approaches that describe breakdown behavior in relation to the applied electric field and the time to breakdown. These models are consistent with experimental data for oxide films thicker than 6 nm under high electric fields around 8–10 MV/cm [154]. However, their applicability under practical operating conditions and for oxides thinner than 5 nm is debated [153]. For those, evidence suggests that degradation is more dependent on voltage than on the electric field [155]. In this voltage-driven degradation model, the energy of electrons—determined by the applied voltage—is the primary factor causing oxide wear [156]. The rate at which defects are generated is directly related to the current passing through the oxide [157]. Consequently, the mechanisms of AHI and AHR offer a more accurate explanation for the degradation and eventual breakdown of oxide layers in these contexts [158].

Dielectric breakdown in MOS structures can be categorized into extrinsic and intrinsic types [159]. Extrinsic breakdown is caused by defects introduced during manufacturing, such as point defects, which compromise the integrity of the dielectric film. Intrinsic breakdown, on the other hand, is related to the inherent properties of the oxide layer.

Figure 15 illustrates various defects that can compromise the integrity of the dielectric film in MOS structures. These defects can accelerate degradation and lead to breakdown at the electrically weakest point. It has been proposed that these weak spots effectively thin the oxide layer, reducing the nominal thickness to what is termed the electrically effective oxide thickness, which is the true measure of the oxide's ability to withstand electrical stress [160].

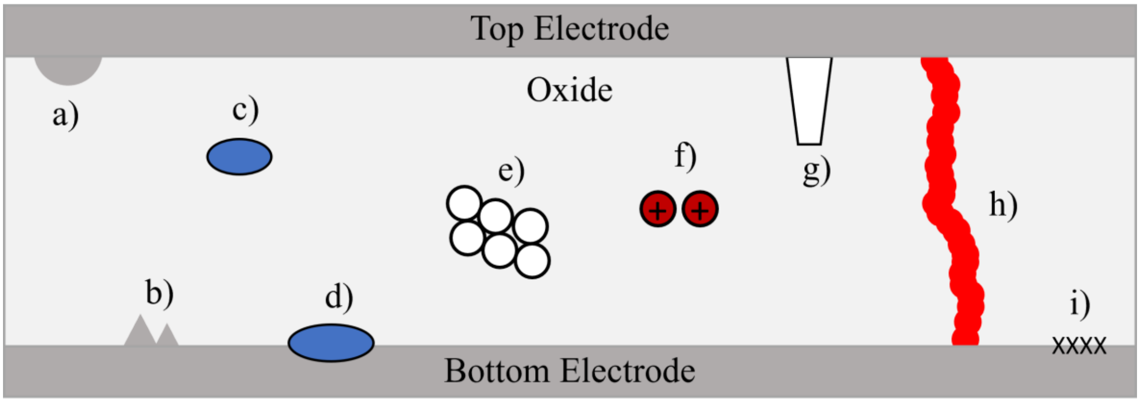

Figure 15: Exemplary defects compromising the integrity of oxide films. a) Thinned oxide. b) Asperities. c) Impurities. d) Particles. e) Areas with increased trap generation rate. f) Mobile ions. g) Voids. h) Interconnections. i) Areas with reduced barrier height [31, 32, 159]. Adapted from [31], copyright University of the West of England, 2006.

2.6.3 Dielectric Breakdown Modes

In practical scenarios, despite the existence of multiple modes of breakdown [147], events are typically classified based on the extent of post-breakdown conduction into two categories: soft breakdown (SBD) and hard breakdown (HBD) [161]. Hard breakdown is marked by an abrupt and substantial surge in leakage current, leading to fatal circuit failure. Conversely, soft breakdown is characterized by a moderate yet variable increase in leakage current, which is significantly lower than that observed in HBD scenarios. In contrast to HBD, SBD does not necessarily imply that circuit operation is affected [31]. In oxide layers with thicknesses ranging from 3 to 7 nm, a precursor to dielectric breakdown (BD) is the progressive defect generation under high electrical stress, observable as an increase in leakage current at low voltages, known as stress-induced leakage current (SILC) [34]. SILC primarily results from trap-assisted tunneling via individual traps [30]. However, when conditions allow for a favorable trap configuration, electrons may tunnel through two or more traps, leading to a phenomenon known as anomalous SILC [162]. For oxides thicker than 7 nm, defect-related charge trapping predominates. However, in thinner oxides, SILC is often obscured by direct tunneling. Notably, even within the 3 to 7 nm thickness range, SILC is typically measurable only at low electric fields, as high-field conditions result in Fowler-Nordheim Tunneling overshadowing the SILC phenomenon [163]. Schematic I-Vs to distinguish between the above-described scenarios are provided in Figure 16.

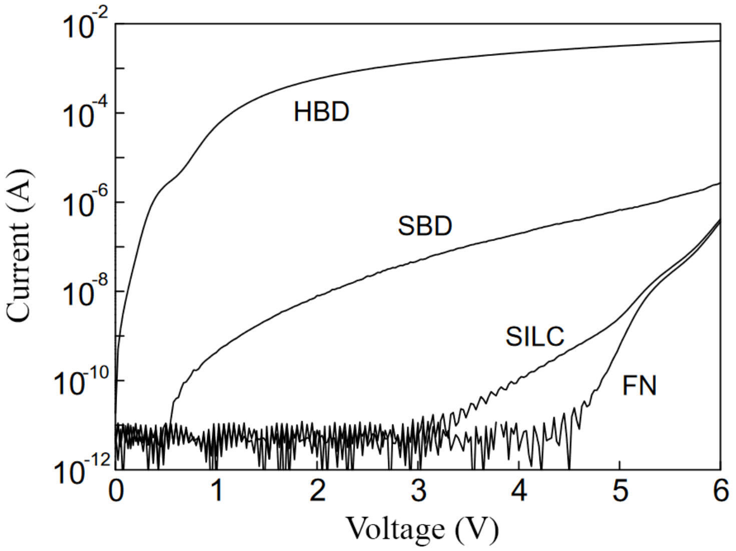

Figure 16: Exemplary I-Vs to demonstrate various stages of oxide degradation. Representative Fowler–Nordheim (FN), stress-induced-leakage-current (SILC), soft breakdown (SBD), and hard breakdown (HBD) curves are provided. The oxide thickness is 4.3 nm, the device area is $6.4 \cdot 10^{-5}$ cm^2, and the substrate is p-type. Adapted from [147], copyright Elsevier Ltd., 2003.

2.6.4 Breakdown Statistics

The random nature of oxide breakdown requires a statistical approach for its description. Given its 'weakest-link' characteristic, the Weibull distribution model is commonly employed to statistically represent the experimental data [164]. The model is defined in (13).

$$F(t_B) = 1 - exp\left[-\left(\frac{t_B}{\alpha_B}\right)^{\beta}\right] \tag{13}$$

With $F(t_B)$ being the cumulative failure probability, t_B the time to breakdown, α_B the time-to-breakdown at approximately 63 % breakdown occurrence, β the shape parameter (also referred to as Weibull slope). In order to simplify data analysis (13) is commonly reformulated into (14).

$$ln[-ln(1 - F(t_B))] = \beta \cdot ln(t_B) - \beta \cdot ln\,(\alpha_B) \tag{14}$$

When plotting $ln[-ln(1 - F(t_B))]$ as function of $ln(t_B)$, the plot follows a linear behavior from which β and α_B can be easily extracted. An example is depicted in Figure 17.

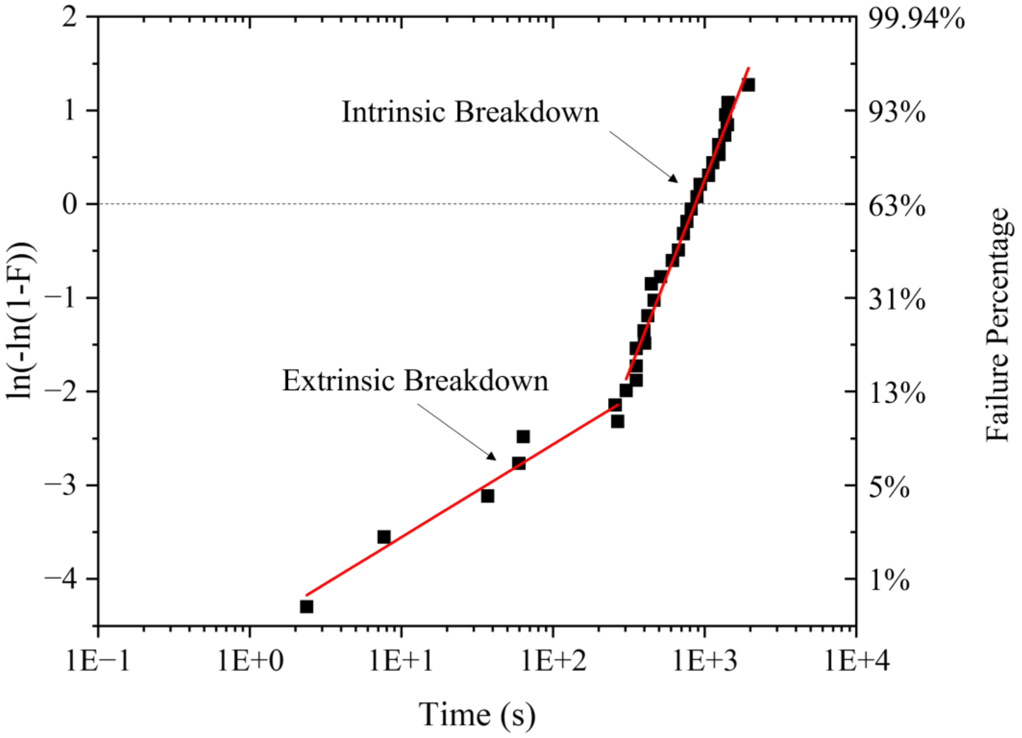

Figure 17: Exemplary Weibull-Plot with an extrinsic ($\beta < 1$) and an intrinsic ($\beta > 1$) branch. Adapted from [165], copyright Universität der Bundeswehr München, 2000.

Note that the shape factor β determines the type of distribution. If $\beta < 1$ the distribution models items that fail early (decreasing failure rate), when $\beta = 1$, it simplifies to an exponential distribution with a constant failure rate, and when $\beta > 1$, it models items that are more likely to fail as they age (increasing failure rate) [165, 166].

Selecting the right test structures is crucial for accurately evaluating oxide reliability [152]. Small area capacitors, ranging from 10^{-6} to 10^{-4} cm^2 [167], are preferred for investigating the intrinsic properties of oxides. In contrast, larger area capacitors, between 10^{-2} and $1\ \mathrm{cm}^2$ [167], are typically used to assess defect density related to extrinsic defects. Traditional macroscopic MOS structures, due to their size being substantially larger than the actual area where breakdown occurs, offer only a generalized insight into the properties of dielectric films. Unlike direct investigations using C-AFM on thin dielectrics, these structures are not capable of pinpointing specific sites of breakdown or detecting microscopic weaknesses at the nanometer scale [168].

2.6.5 Electrical Stress Tests

When characterizing dielectric films, it is standard practice to employ both time-zero and time-dependent measurement techniques. Time-zero breakdown, determined through RVS tests, involves incrementally increasing the voltage on each sample until breakdown is observed, providing a quick and effective measure of the breakdown field strength [32, 167]. On the other hand, time-dependent breakdown is analyzed using constant voltage stress (CVS) or constant current stress (CCS) tests [169, 170]. CVS assesses the duration until breakdown at specified voltage levels and electric fields [167], while CCS is used to determine the total charge that a sample can withstand before breakdown at a set current density [167].

Accelerated stress testing is essential for evaluating dielectric wear-out, as it shortens the time required to simulate the product's lifecycle compared to its anticipated service lifetime [31]. Various models for predicting device lifetime under these conditions have been detailed in the literature [152, 154, 169, 171, 172].

3 Thesis contributions

This chapter is dedicated to outlining the primary objectives of the thesis. It summarizes the key findings and provides a list of publications, in which the results of this thesis have been published.

3.1 Objectives

Although C-AFM is a widely used and effective method for analyzing the topography and electrical resistivity of various samples at the nanoscale, a significant challenge in this field is achieving reproducible data. A concern that is not solely affecting C-AFM science but nanoscience in general [173, 174].

The difficulty in reproducing data in C-AFM arises from the multitude of factors that influence establishing and maintaining tip-sample contact. These factors comprise roughness of the sample, micro-roughness of the tip, scanning speed, applied contact force, contamination of the tip and sample, dynamic modifications of the tip and sample surfaces during scanning, and external disturbances such as vibrations or electrical noise. Due to their fine tip radii, typically ranging from approximately 5 to 200 nm, tips are prone to degradation. This degradation can be attributed mainly to two causes. The first cause, since most C-AFM measurements are conducted in contact mode, are lateral frictions. Depending on the deployed contact force, the tip and sample material roughness and hardness, the ambient humidity, and the scan speed, mechanical abrasion leads to a gradually increased tip radius over time. If a tip with a conductive coating is used, there is a risk that this coating may be scratched off after prolonged use, resulting in a loss of the tip's conductivity. Additionally, it should be considered that non-conductive scratched-off debris from the sample can adhere to the tip, which would lead to significantly increased tip resistance. Lateral frictions pose a dual problem. They do not only diminish the achievable topographical resolution due to the increase in tip radius, but they also contribute to the partial or complete loss of the tip's conductivity [14]. To address this issue, the scientific community has recently adopted the use of intermittent contact mode, in which the tip is retracted during lateral movements, to measure local currents [19].

The second major issue is the high current densities experienced when a bias voltage is applied. Since C-AFMs typically measure currents above a few picoamperes (corresponding to the usual noise level), the current densities encountered by C-AFM tips are never lower than 1 $\mathrm{A/cm^2}$. In certain experiments, these densities can increase dramatically, reaching up to 10^8 $\mathrm{A/cm^2}$ [20]. These high current densities may lead to conductive varnish melting and tip oxidation, which would lead to a profoundly increased tip resistance. Occasionally this degradation occurs abruptly, and one can distinguish well which data sets are still valid. Often however degradation occurs incrementally, which complicates the process of ascertaining the validity of the data. This gradual deterioration can be challenging to detect and may potentially result in incorrect conclusions [14].

With Peakforce Tapping mode already providing an effective means to mitigate tip degradation due to mechanical abrasion, the focus of this thesis is on developing strategies to minimize tip degradation resulting from high current densities. This research aims to assess the extent of degradation in metal coated probes, which are currently the most widely used in the field, under various C-AFM measurement scenarios. Furthermore, readily available alternatives, such as solid Pt probes and software-based current limitation, shall be thoroughly evaluated. The primary goal is to present a robust solution that effectively shields C-AFM probes from damage induced by high current densities. Overall, this thesis shall contribute to the evolution of the C-AFM technique by enhancing its reliability and therewith ensuring more consistent and dependable results in nanoscale material analysis.

3.2 Key Findings

This chapter briefly summarizes the key findings of each experimental chapter of this thesis:

Chapter 4.1.1	This chapter analyzes the dynamic degradation behavior of Pt/Ir-coated C-AFM probes, which are presently the most widely used. The performed experiments suggest a two-phase degradation process of these probes. Initially, the conductive coating undergoes a reduction in thickness before it ultimately melts. During this thinning phase, a stable intermediate state characterized by increased contact resistance was identified. Without a reference,

this intermediate state can be challenging to discern, potentially misleading users to wrong statements in material assessment. It is therefore recommended to always test the performance of the deployed probe initially on a sample with known electrical parameters, or to double check the result by repeating the experiment with a second probe.

The second key finding of this chapter involves the unexpectedly low currents recorded with a PFTUNA probe [15] ($R_{TIP,nom}$ = 25 nm, $k_{C,nom}$ = 0.4 N/m) during tunneling current measurements on a 2 nm $TiO_2/SiO_x/n^{++}$ Si sample. Computational analysis revealed that this reduction in current is attributed to the formation of H_2O nanogap between the tip and the sample. Interestingly, this nanogap persisted despite applying the maximum deflection setpoint (10 V) allowed by the system. To prevent inaccurate conclusions about d_{ox} or V_{on}, it is advisable to use stiffer C-AFM probes for Ramped Voltage Spectroscopy (RVS) on this type of samples, or to conduct the measurements in a controlled environment, such as under vacuum or in a dry nitrogen atmosphere.

Chapter 4.1.2

In this chapter, a comprehensive statistical analysis of the performance of solid Pt probes (model RMN-25Pt300b) in various C-AFM applications was performed. These applications encompassed topography measurements, step height estimations, current map recordings, and RVS. Furthermore, the probe-to-probe variability was assessed. The analysis revealed that the topography obtained using solid Pt probes, compared to Pt/Ir-coated probes (model ContV-Pt), appeared slightly less defined, and the estimated step heights were marginally lower than the reference values obtained with a NCHV-A probe in tapping mode. However, these differences were minor, and the solid Pt probes were found to be fully capable of delivering reliable results in both disciplines. In terms of current mapping, both the solid Pt and Pt/Ir-coated probes produced comparable results. The notable distinction between them was observed in their topographical endurance.

Initially, the ContV-Pt probe offered higher resolution in topography, but this quality rapidly diminished with successive scans. In contrast, the solid Pt probe maintained a consistent quality of topographical detail over numerous scans. This sustained performance underscores the robustness of solid Pt probes particularly for applications that require repeated or prolonged scanning. When recording RVS, the solid Pt probe exhibits superior performance in comparison to the Pt/Ir-coated probe. Notably, the solid Pt probe was able to conduct RVS at 100 locations without displaying any tendency towards higher voltages in the resulting I-V curves. In contrast, the Pt/Ir-coated probe showed a clear downward trend in performance after just the initial curves, failing to register currents above the noise level by approximately the 50th I-V curve. An additional analysis was conducted on the onset potential variations across three different new solid Pt probes. The findings revealed only minor deviations, confirming that probe-to-probe variability is not concern. Overall, for cost-effectiveness and enhanced reliability in C-AFM investigations, solid Pt probes stand out as an excellent choice. While they may offer a marginally lower topographical resolution compared to Pt/Ir-coated probes, this is greatly offset by their significantly better endurance over numerous scans and their substantially increased electrical durability, making them a valuable tool for consistent, long-term C-AFM investigations.

Chapter 4.2.1 This chapter provides an in-depth exploration of the working principle of software-based current limitation featuring the Bruker Dimension Icon. This tool is straightforward to use and does not require prior knowledge of the sample’s resistance. In contrast to solely relying on more durable probes, software-based current limitation actively restricts the resulting currents, thus enabling the extended use (by approximately a factor of 50 for the scenario described in Chapter 4.2.1) of metal-coated probes (which offer a wider variety in probe types), while also safeguarding the sample from current-induced damage. It is important to note, however, that software-based current limitation does not offer absolute current limitation. For instance, when applying a voltage ramp from 0 V to 6 V with a current threshold of 100 pA, the trigger will halt the forward sweep at the voltage level (V_{STOP}) where the current first exceeds the threshold. Enhancing the sampling rate and ramp frequency can minimize current overshoot beyond this threshold and refine precision. Yet, from V_{STOP}, the system unavoidably conducts a backward sweep back to its initial value (0 V in this case). Since electrical stress is a function of both, voltage and time, dielectric breakdown may still occur during this backward sweep, potentially resulting in much higher currents than the set current threshold. Software based current limitation may also be employed while recording current maps. On h-BN on copper (Cu), the generation of new defects could not be fully prevented, but their occurrence notably diminished. In summary, software-based current limitation substantially enhances the reliability of C-AFM investigations across various fields and contributes to cost reduction by ensuring longer probe lifetimes. It however does not provide true current limitation.

Chapter 4.2.2 The concluding chapter presents an innovating development in the form of a new sample holder, integrated with a MOSFET. This design enables true current limitation in both the forward and backward sweep directions, a capability that distinguishes it from software-based current limitation. While similar results could theoretically be achieved by connecting resistors in series with the tip, the novel sample holder eliminates the need for prior knowledge about the sample’s resistance. Additionally, the traditional approach of using resistors often necessitates hardware alterations when switching between different samples. In contrast, the current-limiting sample holder simply requires an adjustment of the gate voltage to accommodate a variety of sample types, streamlining the process significantly. The holder’s design, compatible with standard SOT-23 housed transistors, allows for high customizability across a wide spectrum of experiments.

Furthermore, its versatility ensures compatibility with nearly all C-AFM systems. Overall, the sample holder contributes to enhanced accuracy, reliability, and versatility in C-AFM applications establishing it as an indispensable asset for researchers and practitioners in the field alike.

3.3 List of Publications

The results of this thesis have been published in:

Article 1: Jiang, L., **Weber, J.**, Puglisi, F. M., Pavan, P., Larcher, L., Frammelsberger, W., Benstetter, G. & Lanza, M. (2019). Understanding current instabilities in conductive atomic force microscopy. *Materials*, *12*(3), 459.

Autor Contribution: Validation, formal analysis, investigation, data curation, visualization, manuscript composing, reviewing, and editing.

Article 2: **Weber, J.**, Yuan, Y., Kühnel, F., Metzke, C., Schätz, J., Frammelsberger, W., Benstetter, G. & Lanza, M. (2023). Solid Platinum Nanoprobes for Highly Reliable Conductive Atomic Force Microscopy. *ACS Applied Materials & Interfaces*, *15*(17), 21602-21608.

Autor Contribution: Conceptualization, methodology, validation, formal analysis, investigation, data curation, visualization, manuscript composing, reviewing, editing.

Article 3: **Weber, J.**, Yuan, Y., Pazos, S., Kühnel, F., Metzke, C., Schätz, J., Frammelsberger, W., Benstetter, G. & Lanza, M. (2023). Current-Limited Conductive Atomic Force Microscopy. *ACS Applied Materials & Interfaces 15* (48), 56365-56374.

Autor Contribution: Conceptualization, methodology, validation, formal analysis, investigation, data curation, visualization, manuscript composing, reviewing, editing.

For the evaluation of this PhD dissertation thesis the following articles shall be considered:

Article 2: **Weber, J.**, Yuan, Y., Kühnel, F., Metzke, C., Schätz, J., Frammelsberger, W., Benstetter, G. & Lanza, M. (2023). Solid Platinum Nanoprobes for Highly Reliable Conductive Atomic Force Microscopy. *ACS Applied Materials & Interfaces*, *15*(17), 21602-21608.

Article 3: **Weber, J.**, Yuan, Y., Pazos, S., Kühnel, F., Metzke, C., Schätz, J., Frammelsberger, W., Benstetter, G. & Lanza, M. (2023). Current-Limited Conductive Atomic Force Microscopy. *ACS Applied Materials & Interfaces 15* (48), 56365-56374.

A full list of the Authors publications (as of the 29th November 2023) can be found in the Scientific Vita in Chapter G.

4 Experimental

The experimental section is structured into two principal areas. The initial chapter focuses on a crucial aspect of Conductive Atomic Force Microscopy research: the reliability of different probe types. This chapter is further segmented into two subsections. The first subsection examines the impact of metal-coated C-AFM probes, which are presently the most widely used in the field. The second subsection delves into the potential of solid Pt probes. Owing to their enhanced robustness and comparable topographical resolution, these probes emerge as a potentially promising alternative for C-AFM applications. The second chapter, divided into two subsections, examines the advantages and drawbacks of different current limitation systems. The first subsection addresses software-based current limitation, a readily available and user-friendly solution. This method efficiently restricts the current through the tip/sample junction by halting the forward sweep upon reaching a predefined current threshold. However, it is important to note that during the ensuing, inevitable backward sweep, there is no current limitation. Despite this, compared to scenarios with no current limitation, the lifespan of the probes is still notably prolonged, and damage to the sample due to current induction is minimized. In the second subsection, to address the shortcomings of software-based current limitation, a novel and universally applicable C-AFM sample holder is introduced as a solution for hardware-based current limitation. This innovative holder is designed to effectively limit currents through the tip-sample junction in both sweep directions using an integrated CMOS transistor. This advancement not only offers a significantly extended probe lifetime compared to software-based current limitation systems but also further reduces current-induced damage to the sample.

4.1 Tip Influence on C-AFM Measurements

Conductive Atomic Force Microscopy (C-AFM) is a powerful tool for analyzing materials, offering exceptional lateral resolution and the unique capability to directly correlate surface topography with electrical current [175]. Despite these advantages, the technique faces a critical challenge: Substantial current fluctuations in both, individual experiments and across different studies. These fluctuations can be primarily attributed to two factors [176]: i) Tip degradation, and ii) moisture.

i) The metallic coating on C-AFM tips is susceptible to degradation due to mechanical wear and high current densities, which can generate enough heat to compromise the coating integrity, potentially leading to skewed experimental results [72]. The use of costlier, but more stable, solid metallic tips has been suggested as a solution. A thorough analysis of the capabilities of solid Pt probes is provided in Chapter 4.1.2. Despite their susceptibility to rapid degradation, metal-coated silicon tips remain the standard for C-AFM investigations due to their cost-effectiveness and the relative ease of their production process [18]. Further approaches include the use of doped diamond-coated probes [177] or solid doped-diamond probes [89] (typical dopants are B [86] and N [87]). However, doped-diamond probes are more expensive than solid metal probes and, more importantly, often damage the surface of the samples due to their high stiffness [176]. Advances such as graphene-coated silicon tips [90, 123, 178] show promise for enhancing tip longevity without significantly increasing the tip radius, but these are still under development and not yet commercially available.

ii) Water molecules trapped between the tip and the sample can significantly affect C-AFM measurements [124, 179]. Some C-AFM setups [180, 181] allow for vacuum conditions to mitigate this issue, but most research is still conducted in air, where moisture is ubiquitous. The vacuum levels achievable by standard commercial C-AFM systems ($10^{-4} – 10^{-5}$ torr) may not suffice to eliminate all moisture, which could necessitate heating the sample to temperatures above 100°C - a requirement not always practical or possible.

For C-AFM to reach its full potential in accuracy and reliability, a deeper understanding of tip coating degradation and the dynamics of moisture at the tip-sample interface is essential. These issues will be addressed in Chapter 4.1.1 using metal-coated silicon probes.

4.1.1 Metal-Coated C-AFM Probes

To investigate the degradation of C-AFM tip coatings and assess the impact of a moisture layer between the tip and sample, 2 nm-thick TiO_2 layers on highly doped n-type silicon (n^{++} Si) wafers were fabricated using a plasma-enhanced atomic layer deposition system (PEALD, Savannah, Cambridge Nanotech, Cambridge, UK). The chosen wafers, with a resistivity ranging from 0.008 to 0.02 $\frac{\Omega}{cm}$, are consistent with those employed in prior C-AFM research [54, 182]. The precursors for the deposition were tetrakis(dimethylamido)titanium [$Ti(NMe_2)_4$] for titanium and oxygen for the oxide component. The deposition was conducted at a temperature of 200 C, achieving a growth rate of 0.51 Å per cycle, which translates to 40 cycles for a 2 nm film. The ALD process involved a 0.1-second pulse of $Ti(NMe_2)_4$, followed by a 10-second hold. The plasma phase utilized an oxygen flow rate of 30 sccm for 20 seconds at 300 W power, with an additional 5-second hold time. Prior to titanium dioxide (TiO_2) layer deposition, the Si wafers were etched in a 4 % hydrofluoric acid (HF) solution to remove the native silicon oxide (SiO_x) layer. Cross-sectional transmission electron microscopy (TEM) imaging verified the precise TiO_2 thickness and revealed a roughly 1 nm interfacial SiO_x layer, a byproduct of the oxygen interaction with the Si substrate [183, 184]. C-AFM topographic analysis showed the TiO_2 surface roughness to be under 200 pm, comparable to the initial Si wafer surface [185], confirming the coating's conformality and quality (see Figure 18). The transmission electron microscope (TEM) analyses were performed using a JEM-2100 (JEOL, Akishima, Tokyo, Japan), and C-AFM assessments were conducted with a Digital Instruments Dimension 3100 (Veeco, Plainview, NY, USA) in Contact Mode using a new PFTUNA probe under standard air atmosphere.

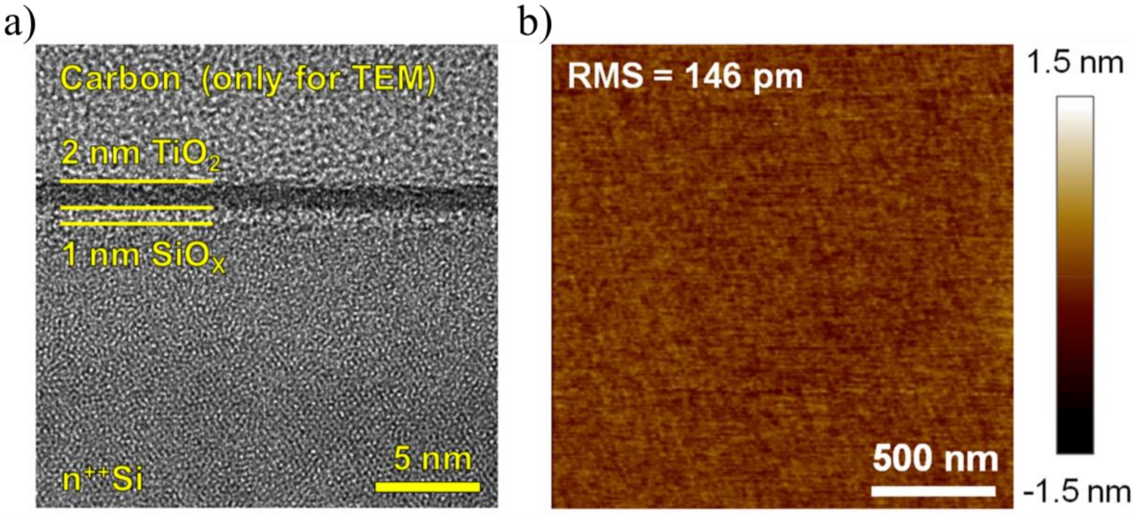

Figure 18: Sample analysis using TEM and C-AFM. a) Cross-sectional TEM image of $TiO_2/SiO_x/n^{++}Si$ sample. Note the top carbon layer is a prerequisite for the TEM investigation only. b) C-AFM topographic map of a $TiO_2/SiO_x/n^{++}Si$ sample. Adapted from [176], copyright MDPI, 2019.

In this study, two types of C-AFM tips, SCM-PIT [186] and PFTUNA [15], were utilized. Both are made from Si and silicon nitride (SiN) respectively and coated with a 20 nm layer of Pt/Ir, a 95 % platinum and 5 % iridium alloy. The SCM-PIT tips feature a nominal tip radius (R_{TIP}) of 20 nm, with a maximum of 25 nm, while the PFTUNA tips have a typical R_{TIP} of 25 nm, extending up to 35 nm. The primary distinction between these tips lies in their spring constants: the SCM-PIT has a spring constant of 2.8 N/m, whereas the PFTUNA's is 0.4 N/m (nominal values). I-V curve sequences were recorded at multiple $TiO_2/SiO_x/n^{++}Si$ sample locations using both SCM-PIT and PFTUNA tips, with a distance of 1 µm in between each I-V to prevent interference. The ramped voltage stress was applied at 0.1 Hz with current limits set from −100 pA to 100 pA, ensuring accurate readings by applying a positive bias to the C-AFM tip and grounding the sample holder [187]. A deflection setpoint of 4 V was selected for both tip types, resulting in contact forces of approximately 151 nN for PFTUNA and 526 nN for SCM-PIT, higher than typical to promote reliable contact [55]. It should be emphasized that this study focuses solely on spectroscopic measurements, where lateral friction is minimal, thus allowing for the use of increased contact force without the risk of early C-AFM tip wear. Although current/resistance mapping is a valuable technique for analyzing various nanomaterials [188-190], it was excluded to avoid the excessive lateral stress that could compromise the integrity of the C-AFM tips.

87 I-V curves with an RVS ranging from 0 V to a maximum of 5 V were recorded using the SCM-PIT tip (see Figure 19 a). The onset potential (V_{on}), where the current first exceeded 10 pA, varied from 0.49 V to 1.35 V. After recording these curves, the SCM-PIT tip maintained its original conductivity without any observable degradation. In contrast, with the PFTUNA tip, we recorded 107 I-V curves under the same RVS conditions. The initial 85 curves, detailed in Figure 19 b, had V_{on} values between 1.48 V and 2.10 V. A distinct shift was observed in the subsequent 22 curves, with V_{on} values ranging from 2.81 V to 3.80 V, as depicted in Figure 19 c. After this set of measurements, the PFTUNA tip lost conductivity, failing to register any current above the noise threshold at the C-AFM's maximum bias of 10 V.

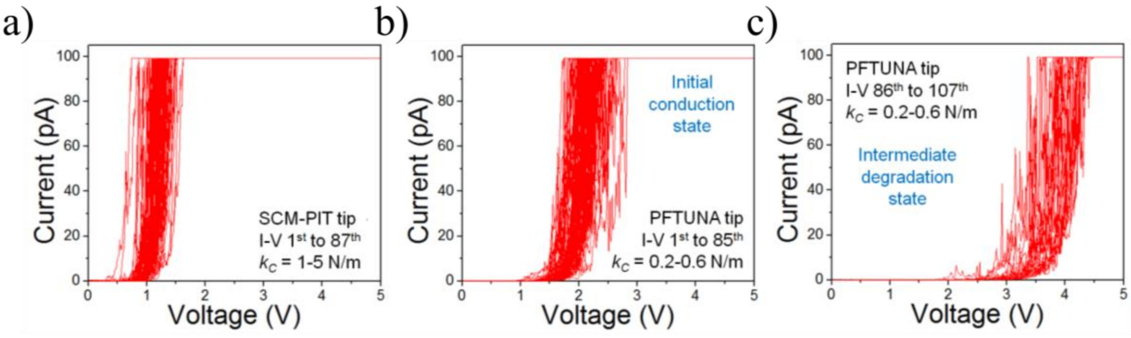

Figure 19: Sequences of I-Vs using SCM-PIT and PFTUNA probes. (a) 87 I-V curves were obtained using a SCM-PIT probe at various points on the $TiO_2/SiO_x/n^{++}Si$ sample. (b) The first set of 85 I-V curves and (c) a subsequent set of 22 I-V curves were similarly gathered using a PFTUNA probe on the same sample. All measurements were conducted in a standard atmospheric environment. The graphs display the applied voltage to the C-AFM tip on the x-axis, while the sample holder was grounded. Adapted from [176], copyright MDPI, 2019.

Comparing Figure 19 b and Figure 19 c reveals degradation of the PFTUNA tip, corroborating the findings from [18], in which a detailed analysis of tip degradation due to metallic varnish melting, tip apex erosion, and particle adhesion is provided. However, the dynamics of this degradation - specifically, the progression of current signal decay - remain uncharted. While [18] addresses degradation during lateral scans, which are prone to accelerated wear and contamination due to friction, this study focuses on spectroscopic I-V curves, where such effects are presumed to be less pronounced. Nonetheless, prolonged high-current conditions in I-V spectroscopy may expedite the melting of the metallic coating [90].

From the comparison of Figure 19 b and Figure 19 c, it is evident that tip conductivity diminishes progressively, transitioning through an intermediate state with stable yet altered measurements due to increased contact resistance, likely from metallic coating wear. This intermediate state, characterized by higher onset voltages (V_{on}), could mislead researchers by presenting altered sample characteristics, such as an overestimated oxide thickness. Therefore, caution is advised when interpreting measurements from tips in this compromised condition.

To further quantify the degradation of C-AFM tips, an additional experiment was conducted. It involved placing a metal-coated silicon tip on a metallic substrate - a silicon wafer with a 300 nm layer of SiO_2, coated with a 100 nm layer of platinum via atomic layer deposition (ALD). The platinum film was connected to the C-AFM plate using silver paint. Sequences of I-V curves were then collected by using an external source meter (Keithley 6430, Keithley Instruments, Cleveland, USA) [191-193]. This setup, utilizing a pure metallic junction between the tip and the sample, allows for the direct monitoring of the C-AFM tip's metallic coating performance without the interference of tunneling currents across the $TiO_2/SiO_x/n^{++}Si$ sample. Employing a source meter also enables the measurement of larger currents, thus facilitating the determination of the maximum current threshold (I_{MAX}) at which tip degradation occurs.

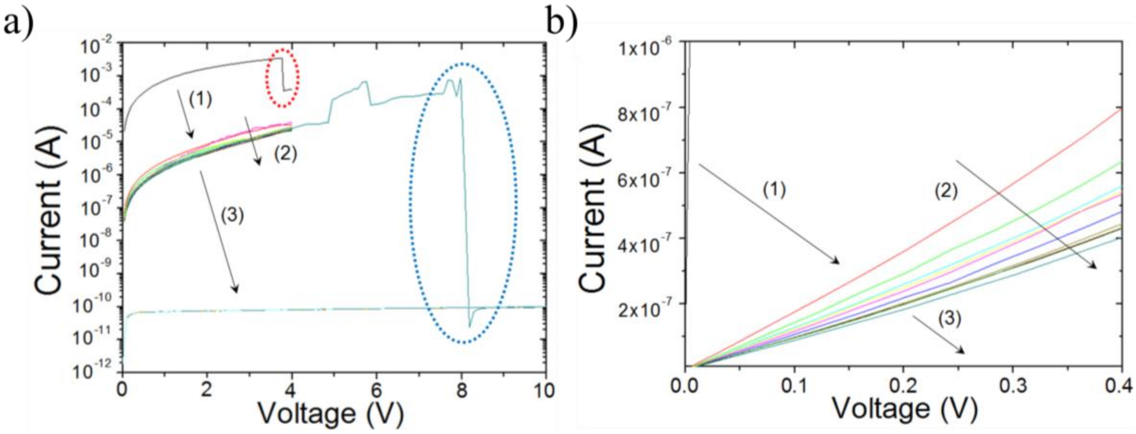

Figure 20: Sequence of I-V curves obtained from a single location on a 100 nm Pt/300 nm SiO_2/Si sample using a C-AFM that is linked to a Keithley 6430 source meter. a) The data are presented on an expanded scale to clearly show the degradation phases of the C-AFM tip. The red dashed circle highlights the C-AFM tip's initial degradation phase, leading to an intermediate state, while the blue dashed circle marks the point of complete tip degradation. (b) Identical data depicted on a more detailed scale. Adapted from [176], copyright MDPI, 2019.

The results, depicted in Figure 20, are presented in two scales for clarity. The initial I-V curve demonstrates a perfect linear response, terminating in a sudden current drop at $I_{MAX} = 3.5$ mA, as highlighted by the red circle in Figure 20 a. Calculations from the linear portion of the I-V curve yield an initial contact resistance of 4.54 kΩ, aligning with the manufacturer's specifications. Post-decline, the tip maintains a near-linear response with an increased contact resistance of 5.88 MΩ, correlating with the stable resistive state observed in Figure 19 c. This suggests a two-phase degradation process: initial narrowing followed by complete melting of the tip coating. The intermediate state, marked by increased contact resistance, could mislead users in material assessments. Continued stress leads to total tip failure at approximately 8 V and $I_{MAX} = 510$ µA, as indicated by the blue circle in Figure 20 a.

To discern the variations in electrical signals obtained with different C-AFM tips, the I-V curves were analyzed using advanced computational models. Historically, equations from various tunneling models such as Direct Tunneling [194], Fowler-Nordheim Tunneling [195], and Poole-Frenkel [196], as well as their combinations [197], have been instrumental in investigating currents across thin dielectrics like SiO_2 [198] and HfO_2 [198]. For the complex TiO_2/SiO_x bilayer system in our study, we employed Ginestra® (Version 3.1, Applied Materials Inc., Santa Clara, USA), a sophisticated multilevel computational platform tailored for precise simulations of charge transport and degradation in dielectric stacks [199, 200]. Ginestra®'s capabilities include a comprehensive treatment of transport mechanisms—Direct Tunneling, Fowler-Nordheim Tunneling, and multiphonon trap-assisted tunneling—and full 3D simulations that incorporate material-specific parameters, defect impacts, localized power dissipation at defects, and the resultant electric field distortions due to trapped charges.

Figure 21 a depicts the fit of 87 I-V curves acquired using SCM-PIT tips. For the fitting, a $Pt/TiO_2/SiO_x/n^{++}Si$ structure with a 2 nm TiO_2 layer and a 1 nm SiO_x layer was considered, and an A_{eff} of 100 nm² assumed. The TiO_2 and SiO_x were characterized by their respective electron affinity (φ), bandgap (E_g), and dielectric permittivity (ε), using the following values: $\varphi_{TiO_2} = 3.55\ eV$ [201], $E_{g,TiO_2} = 3\ eV$ [202], $\varepsilon_{TiO_2} = 60$ [203], $\varphi_{SiO_x} = 0.95\ eV$ [204], $E_{g,SiO_x} = 8.9\ eV$ [205], and $\varepsilon_{SiO_x} = 6.6$ [206]. Oxygen vacancy defects with a density of $5 \cdot 10^{19}\ cm^{-3}$ were included into both layers. Figure 21 c illustrates the structure's schematic as generated by Ginestra®. To mirror experimental variability, we simulated 300 randomized devices, accounting for random defect distribution, oxide thickness variations (±0.3 nm), and contact area deviations (ranging from 64 to 144 nm² with an average of 100 nm²). The simulation results align closely with the experimental data, demonstrating the model's robustness in capturing the effects of structural randomness on electrical behavior.

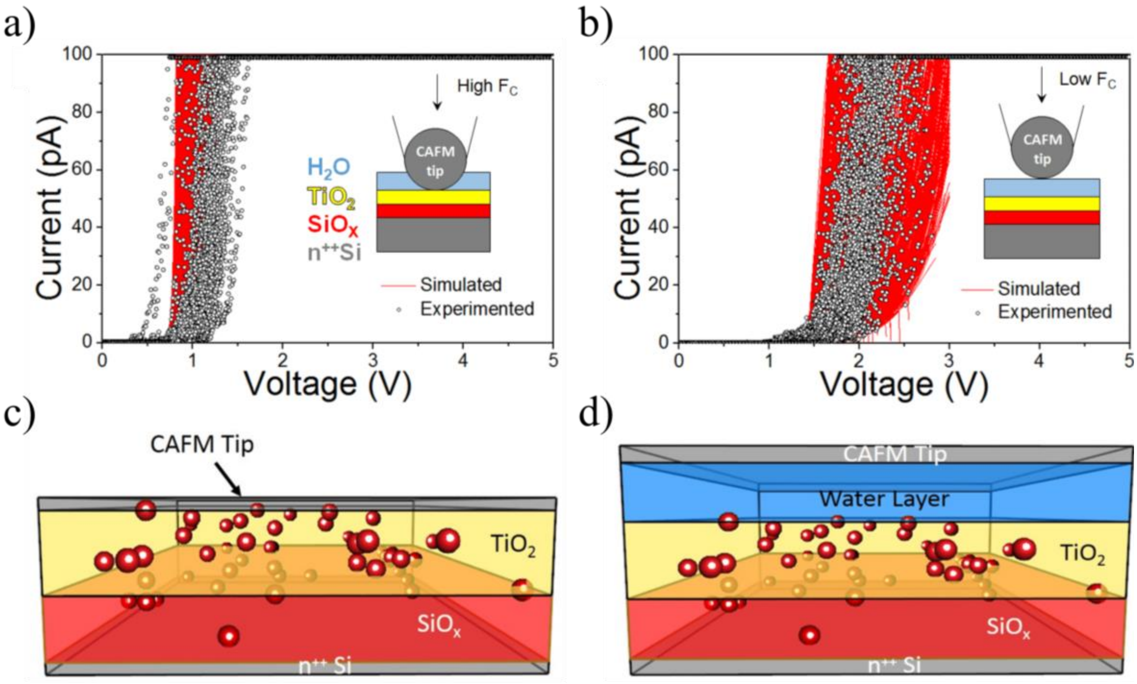

Figure 21: Experimental I-V curves recorded at various locations of the $TiO_2/SiO_x/n^{++}Si$ samples using (a) an SCM-PIT and (b) a PFTUNA tip, and their belonging fittings using Ginestra®. The experimental curves equal those in Figure 19 a and Figure 19 b. A range of simulated curves is presented to reproduce the intrinsic variability of the experiments (density of traps, thickness of each layer, and tip/sample contact area). Insets (a) and (b) illustrate the respective tip/sample configurations. Figures (c) and (d) depict the detailed structural schematics for the SCM-PIT/$TiO_2/SiO_x/n^{++}Si$ and PFTUNA/$H_2O/TiO_2/SiO_x/n^{++}Si$ systems as modeled by Ginestra®, with red spheres indicating the location of intrinsic defects within the TiO_2 and SiO_x layers. Adapted from [176], copyright MDPI, 2019.

Subsequently, an attempt to fit the I-V curves recorded using PFTUNA tips was made. Notably, the primary distinction between the SCM-PIT and PFTUNA tips lies in their spring constant (k_C); the k_C for PFTUNA tips is seven times less than that for SCM-PIT tips. It should be highlighted that variations in k_C only modify the value of A_{eff} in the tip/sample system [207]. This relationship is quantitatively defined by (15) and (16):

$$A_{eff} = A_c = \pi \cdot r_c^2 = \pi \cdot \left(\frac{F_c \cdot R_{TIP}}{K}\right)^{\frac{2}{3}} \tag{15}$$

$$\frac{1}{K} = \frac{3}{4} \cdot \left(\frac{1-\nu_1^2}{E_1} + \frac{1-\nu_2^2}{E_2}\right) \tag{16}$$

With A_c being the contact area, r_c the radius of the contact area, and K the reduced Young's modulus consisting of the Poisson's ratios of the tip and sample ν_1 and ν_2 respectively, and the respective moduli of elasticity E_1 and E_2. The contact force F_c is the product of the spring constant k_C and the cantilever deflection δ_C. It's important to note that the effective contact area A_{eff} is not always equivalent to A_c. The electric field may be confined at certain points within A_c, resulting in $A_{eff} < A_c$, or it may extend beyond, leading to $A_{eff} > A_c$ [28]. However, for the purposes of this experiment, equating A_{eff} and A_c is a reasonable approximation because the insulating nature of the sample restricts the spread of the electric field, and the applied contact force is not excessively high, which would otherwise lead to significant field confinement (field confinement due to excessive contact force typically occurs with tips that feature a spring constant greater that 20 N/m) [28].

For the Ginestra® fitting of I-V curves obtained with PFTUNA tips, we employed the same parameters as those used for SCM-PIT tips, except for A_{eff}. The relationship between A_{eff} for SCM-PIT and PFTUNA tips can be deduced from (15) and (16), resulting in $A_{eff.SCM-PIT}$ being approximately 1.90 times $A_{eff.PFTUNA}$. For this calculation the cantilever deflection was extracted for both probes by dividing the deflection setpoint with the average slope of the trace and retrace characteristic in contact using three Force-Distance curves at various locations for each probe, see Figure 22.

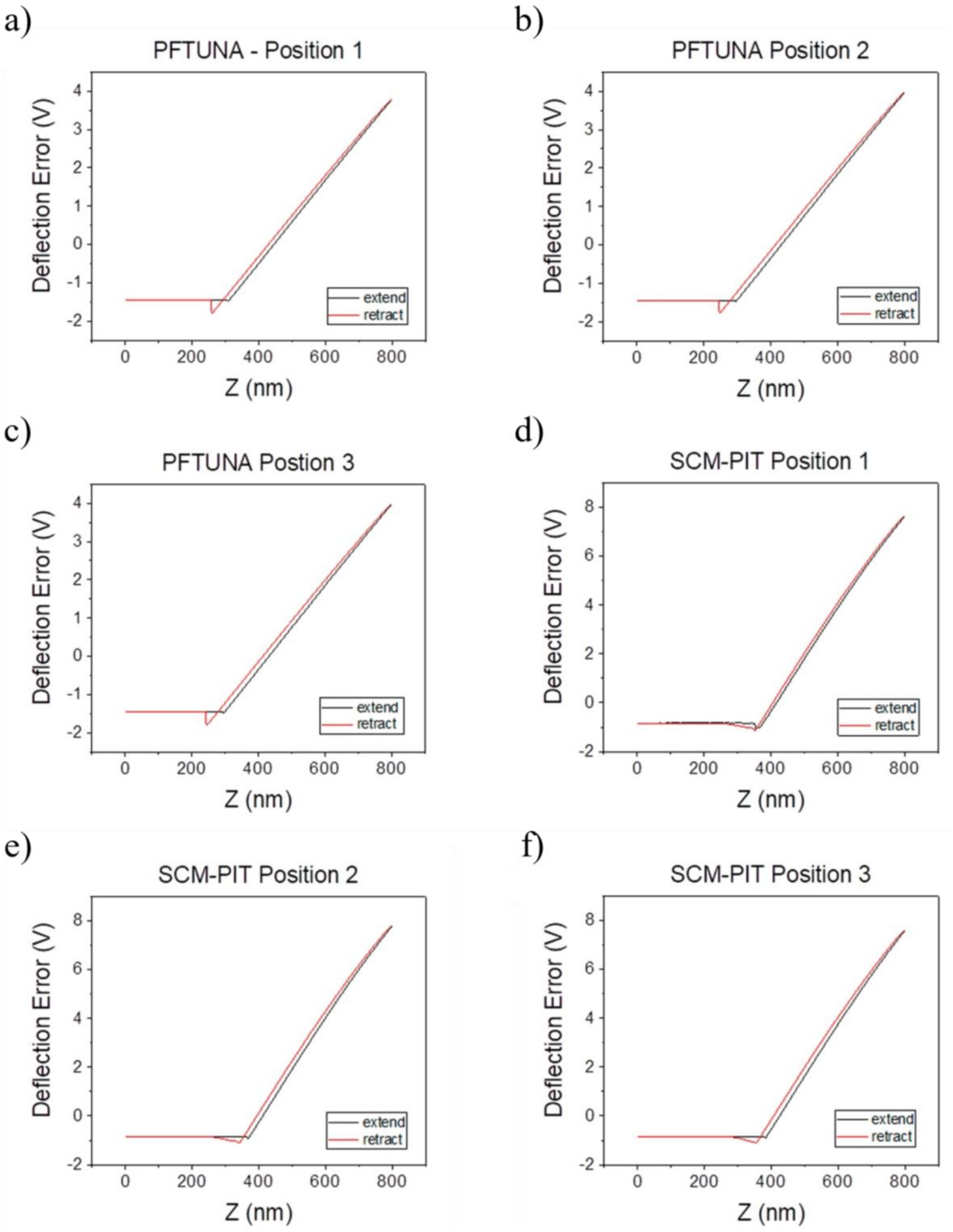

Figure 22: Force Distance curves recorded with new SCM-PIT and PFTUNA probes at various locations on TiO2/SiOx/n++ Si. a) PFTUNA at Position 1. b) PFTUNA at Position 2. c) PFTUNA at Position 3. d) SCM-PIT at Position 1. e) SCM-PIT at Position 2. f) SCM-PIT at Position 3.

The following parameters were used $\nu_{1,Pt} = 0.39$ [208], $\nu_{2,TiO_2} = 0.27 - 0.29$ [209], $E_{1,Pt} = 171\ GPa$ [208], $E_{2,TiO_2} = 230 - 288\ GPa$ [209], $k_{C,SCM-PIT} =$

$1.2;\ 2.8(nom);\ 5.5\ N/m$ [186], $k_{C,PFTUNA} = 0.2;\ 0.4(nom);\ 0.8\ N/m$ [15], $R_{TIP,SCM-PIT} = 20;\ 22.5;\ 25\ nm$ [186], and $R_{TIP,PFTUNA} = 25;\ 30;\ 35\ nm$ [15]. Given that the average $A_{eff.SCM-PIT}$ value considered in Figure 21 a is 100 nm², an A_{eff} of 52 nm^2 with a spread of ± 24 nm^2 (similar to the percentage spread assumed for the 100 nm^2) was chosen for the PFTUNA tip. However, this approach did not yield a satisfactory fit between the simulated and experimental I-V curves. Even when calculating the minimum possible A_{eff} using the smallest values of $R_{TIP,PFTUNA}$, $k_{C,PFTUNA}$, and δ_C and the largest values for ν_{2,TiO_2} and E_{2,TiO_2}, which gives a ratio of $A_{eff.SCM-PIT}$ to $A_{eff.PFTUNA}$ of 5, the fit was still not achieved. This outcome suggests that the lower currents observed with PFTUNA tips, compared to SCM-PIT tips, cannot be attributed solely to a reduced A_{eff} due to a lower spring constant. It implies that additional factors are contributing to the observed differences in current.

Given that the properties of the tips are highly similar, and both the sample and C-AFM setup remain constant, the significant reduction in current observed with PFTUNA tips likely stems from the presence of an ultra-thin nanogap between the C-AFM tip and the sample. This gap is likely filled with water (H_2O) molecules, since the measurements were performed under an ambient atmosphere [124, 210]. This phenomenon could be attributed to the lower k_C of PFTUNA tips compared to SCM-PIT tips, leading to a reduced F_c. However, this finding is quite unexpected, especially since we deliberately applied a high F_c of approximately 151 nN by setting the deflection setpoint (DS) to 4 V. To determine the presence of a water film at the tip/sample interface, the I-V curves recorded with PFTUNA tips were re-simulated using the same parameters above, with the sole addition of an ultra-thin H_2O nanogap (1.2 ± 0.1 nm) between the PFTUNA tip and the sample. This configuration, depicted as $Pt/H_2O/TiO_2/SiO_x/n^{++}Si$ in Figure 21 d, models the water nanogap with an electron affinity of $\varphi_{H_2O} = 1\ eV$ [211], a bandgap of $E_{g,H_2O} = 6.9\ eV$ [212], and a dielectric permittivity of $\varepsilon_{H_2O} = 80$ [213]. Remarkably, incorporating the H_2O nanogap into the simulation resulted in an excellent fit with the experimental I-V curves, as shown in Figure 21 b. The simulation also considered variability in the water layer thickness, with 300 randomized devices simulated in total. The calculated thickness of the water nanogap, necessary to fit the measurements, aligns with previous research on comparable samples [124, 210]. This outcome, supported by Ginestra® simulations, suggests that despite applying a high deflection setpoint (DS) of 4 V, resulting in a contact force F_c of approximately 151 nN, the PFTUNA tip was unable to penetrate the water layer and make direct contact with the sample. This is visually represented in the inset image of Figure 21 b, in contrast to the inset image of Figure 21 a.

In an attempt to disrupt the water layer, we repeated the experiments using the maximum deflection setpoint (DS) permitted by our system, which was 10 V. Theoretically, applying a DS of 10 V with a PFTUNA tip featuring a spring constant k_c of 0.4 N/m should generate a contact force F_c of approximately 378 nN. Contrary to expectations, even at this high DS, only minor changes in current (within the variability range of those recorded in Figure 19 b) were observed, and no notable variations were detected at intermediate DS values of 6 V and 8 V. This finding is in line with other studies that also reported negligible differences in I-V characteristics beyond a certain DS threshold [55]. However, the inability of a theoretical force of ~378 nN to penetrate the water layer suggests that the actual force exerted by the C-AFM at a DS of 10 V might be lower than anticipated. Notably, at such high force levels, some materials were even observed to be scratched by the C-AFM tip [93, 214]. It is likely that capillary forces arising from the water meniscus at the tip-sample interface exert a repulsive force, counteracting the force applied by the system [207]. These results suggest that PFTUNA tips are unsuitable for obtaining sequences of I-Vs under environmental conditions on this type of sample. However, this does not imply that all prior C-AFM studies using this setup are flawed. It is clear that quantitative I-V curves cannot be reliably obtained with these types of tips under ambient atmosphere, even when applying the maximum contact force (i.e., DS) permitted by the C-AFM. Nevertheless, when analyzing different samples, relative variations in the data may still provide valuable insights. Additionally, the nanogap observed during spectroscopic I-V curve acquisition might not be a factor during lateral scans, as the sideward movement of the tip could help displace the H_2O molecules.

In summary, over 80 I-Vs were collected on a $TiO_2/SiO_x/n^{++}$ Si sample using C-AFM with two nearly identical types of tips, differing only in their spring constants k_C of 0.4 N/m and 2.8 N/m. Notably, the currents measured with the 0.4 N/m tip were significantly lower than expected and could not be explained by a reduction of A_{eff}. Computational calculations revealed that this substantial reduction in current is attributable to a water nanogap formed between the C-AFM tip and the sample, caused by the lower contact force. This nanogap persisted even when applying the maximum contact force the equipment could provide (using a DS of 10 V). Furthermore, the degradation process of C-AFM tips was alluded, noting an intermediate stable state with increased contact resistance before complete degradation. These findings emphasize the importance of considering factors like the presence of a water layer or tip degradation when interpreting C-AFM data, as these can lead to erroneous conclusions, such as incorrect assumptions about oxide thickness or onset voltage. The results of this study have been published in [176].

4.1.2 Solid Pt Probes

In recent years, the use of solid Pt probes in C-AFM has been gaining popularity [215, 216] due to their durability, minimal sample damage, and cost-effectiveness compared to doped-diamond probes, both coated and solid [123]. Despite this growing interest, a comprehensive statistical assessment of the performance of solid Pt probes relative to traditional platinum/iridium (Pt/Ir)-coated silicon probes is still lacking. Subsequently, a detailed statistical analysis of the conductivity, resolution, and durability of solid Pt probes under various C-AFM working conditions is presented. The results indicate that the resolution of both topographic and current maps obtained with solid Pt probes is very similar to those produced using Pt/Ir-coated Si probes. However, solid Pt probes demonstrate significantly enhanced durability across all experimental conditions tested. This study offers valuable insights for C-AFM practitioners, potentially contributing to improved reliability and efficiency in their research.

This experiment utilized a Dimension Icon AFM from Bruker, which was operated in an air atmosphere with a relative humidity of 53.5% and equipped with four distinct types of probes. The first type, Bruker's NCHV-A [217] (nominal $R_{TIP} = 8\ nm$, $k_C = 40\ N/m$), consists of silicon probes typically used for topographic measurements in tapping mode. Tapping mode is noted for providing the highest resolution in topographic AFM measurements due to the small radius of the tip and the absence of lateral frictions [37, 218]. Thus, measurements obtained with these probes serve as a benchmark for evaluating the quality of other probes. The second type is Bruker's ContV-Pt [16] (nominal $R_{TIP} = 25\ nm$, $k_C = 0.2\ N/m$), silicon probes with a platinum/iridium (Pt/Ir) coating on the tip and cantilever front side for electrical measurements in contact mode. The specific details about the thickness and composition of the Pt/Ir coating remain undisclosed, leaving ambiguity regarding whether the term Pt/Ir denotes a layer of platinum over iridium or an alloy, as utilized by other manufacturers. The third type, Bruker's SCM-PIT-V2 [17] (nominal $R_{TIP} = 25\ nm$, $k_C = 3\ N/m$), are also Pt/Ir-coated silicon probes, similar to the ContV-Pt but with a higher spring constant. The fourth type, the RMN-25Pt300b [88] from Rocky Mountain Nanotechnology (nominal $R_{TIP} = 20\ nm$, $k_C = 18\ N/m$), features probes made entirely of solid platinum for the tip and cantilever, also used for electrical measurements in contact mode.

Multiple ContV-Pt and RMN-25Pt300b probes are analyzed using a SEM (Nova NanoSEM 630, FEI, Oregon, USA), with R_{TIP} estimated by fitting the apex of each tip with a circle, as outlined in [219]. Figure 23 illustrates the results: for five Pt/Ir-coated tips (nominal R_{TIP} = 25 nm), the actual R_{TIP} ranges from 20.7 to 28.9 nm, and for ten solid Pt tips (nominal R_{TIP} = 20 nm), the actual R_{TIP} varies between 10.9 and 28.5 nm. Since the manufacturers do not specify the variability of R_{TIP} on their websites, it is unclear if these values fall within expected specifications. Nonetheless, the R_{TIP} variability for both types of tips appears to be reasonable and within acceptable limits.

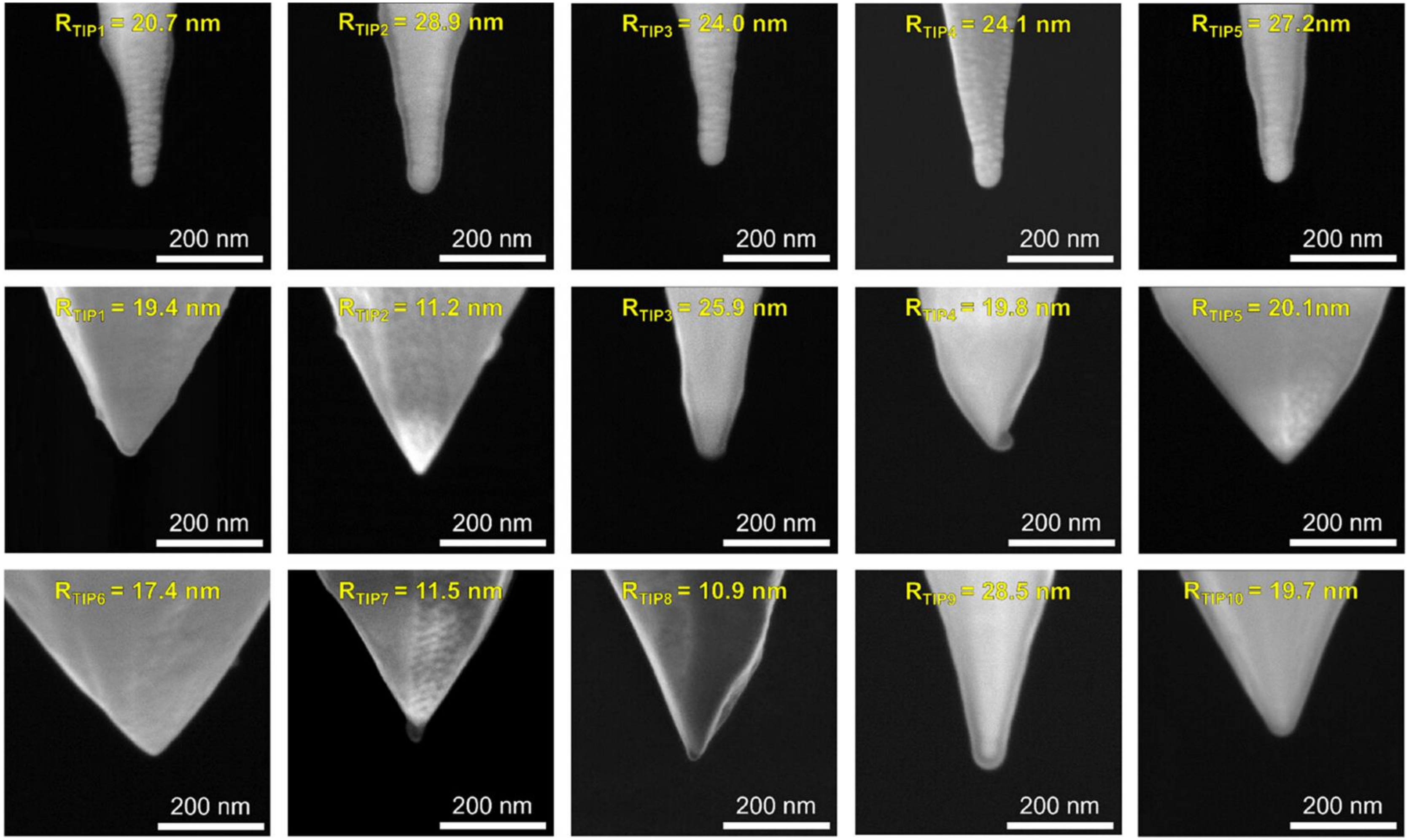

Figure 23: Comparative sharpness of Pt/Ir-coated and solid Pt C-AFM probes. SEM images of the apex of different C-AFM probes. The first row illustrates Pt/Ir-coated probes (ContV-Pt), while the second and third rows showcase solid Pt probes (RMN-25Pt300). Adapted from [72], copyright American Chemical Society, 2023.

A series of experiments were conducted to evaluate the quality of topographic maps, current maps, and spectroscopic measurements obtained using each type of probe. Five distinct samples, each with unique properties, were utilized for this assessment. Samples 1, 2, and 3 are composed of 3.4, 4.7, and 5.6 nm SiO_2 layers, respectively, grown by rapid thermal oxidation on highly conductive n-type (100) silicon, doped with arsenic and featuring a resistivity of 0.0025–0.0035 $\Omega\cdot$cm. These samples are exemplary models of state-of-the-art SiO_2 dielectrics, characterized by their homogeneity, low defect concentration, and well-understood parameters such as electron mass and barrier height. This uniformity minimizes uncertainties in the tip/sample system, aiding in the precise interpretation of differences in recorded current signals. The highly conductive substrate beneath the SiO_2 layer is advantageous, as it eliminates the potential drop typically encountered with standard silicon substrates [197]. Sample 4 is a multilayer molybdenum disulfide (MoS_2) flake, produced through mechanical exfoliation and transferred onto a 300 nm SiO_2/Si wafer [220]. This sample serves as an ideal test subject for probing the thickness measurement capabilities at the flake's edge. Lastly, Sample 5 comprises a stack of hexagonal boron nitride (h-BN) about 10 layers thick (approximately 3.3 nm), grown via chemical vapor deposition on Cu foil [221]. This sample's rougher texture compared to SiO_2 provides an opportunity to assess the solid Pt probes' effectiveness in mapping topographic-current correlations. Additionally, the presence of multiple local defects in this sample allows for the evaluation of the probes' ability to quantify defect sizes.

The cross-sectional morphological properties of the SiO_2/Si samples were characterized using a TEM (TITAN Themis 200, FEI, Oregon, USA). Prior to TEM analysis, as detailed in Figure 24, a thin lamella was extracted from the samples using a Focused Ion Beam (FIB, Helios Nanolab 450S, FEI, Oregon, USA). The obtained images, as illustrated in Figure 25 a, confirmed that the thickness of the SiO_2 film precisely matched the expected value. Additionally, the images revealed that the SiO_2 film possesses an amorphous and homogeneous structure. The surface of the SiO_2 film and its interface with the Si substrate were observed to be exceptionally flat and sharply defined. These observations confirm the high quality of the industrial SiO_2/Si samples.

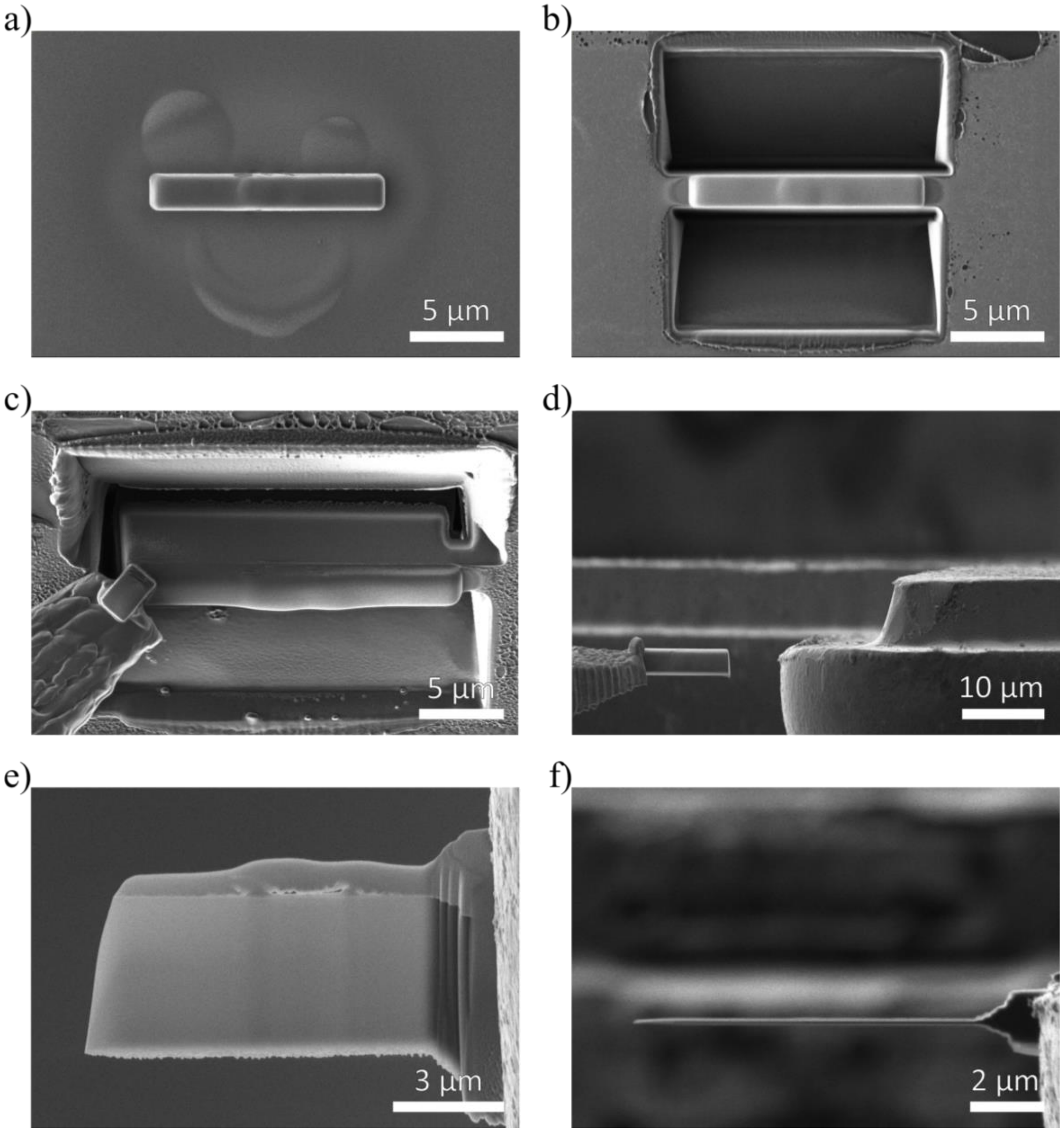

Figure 24: FIB TEM lamella preparation. a) Deposition of protective layer. b) Material removal. c) J-Cut and Pt deposition to merge micromanipulator with lamella. d) Positioning of lamella at TEM grid. e) Pt deposition to merge lamella with TEM grid and micromanipulator severing with FIB. f) lamella thinning.

Initially, the topography of the SiO_2 sample was evaluated using a silicon probe (NCHV-A) in tapping mode. The surface of the sample exhibited remarkable flatness, with a root mean square (RMS) roughness of 0.2 nm (see Figure 25 b), corroborating findings from previous studies [222]. Subsequent measurements of the same SiO_2 sample's topography were conducted in contact mode using a Pt/Ir-coated Si probe (ContV-Pt) and a solid Pt probe. The RMS roughness values detected for the surface were 0.16 nm and 0.12 nm, respectively, as shown in Figure 25 c and Figure 25 d.

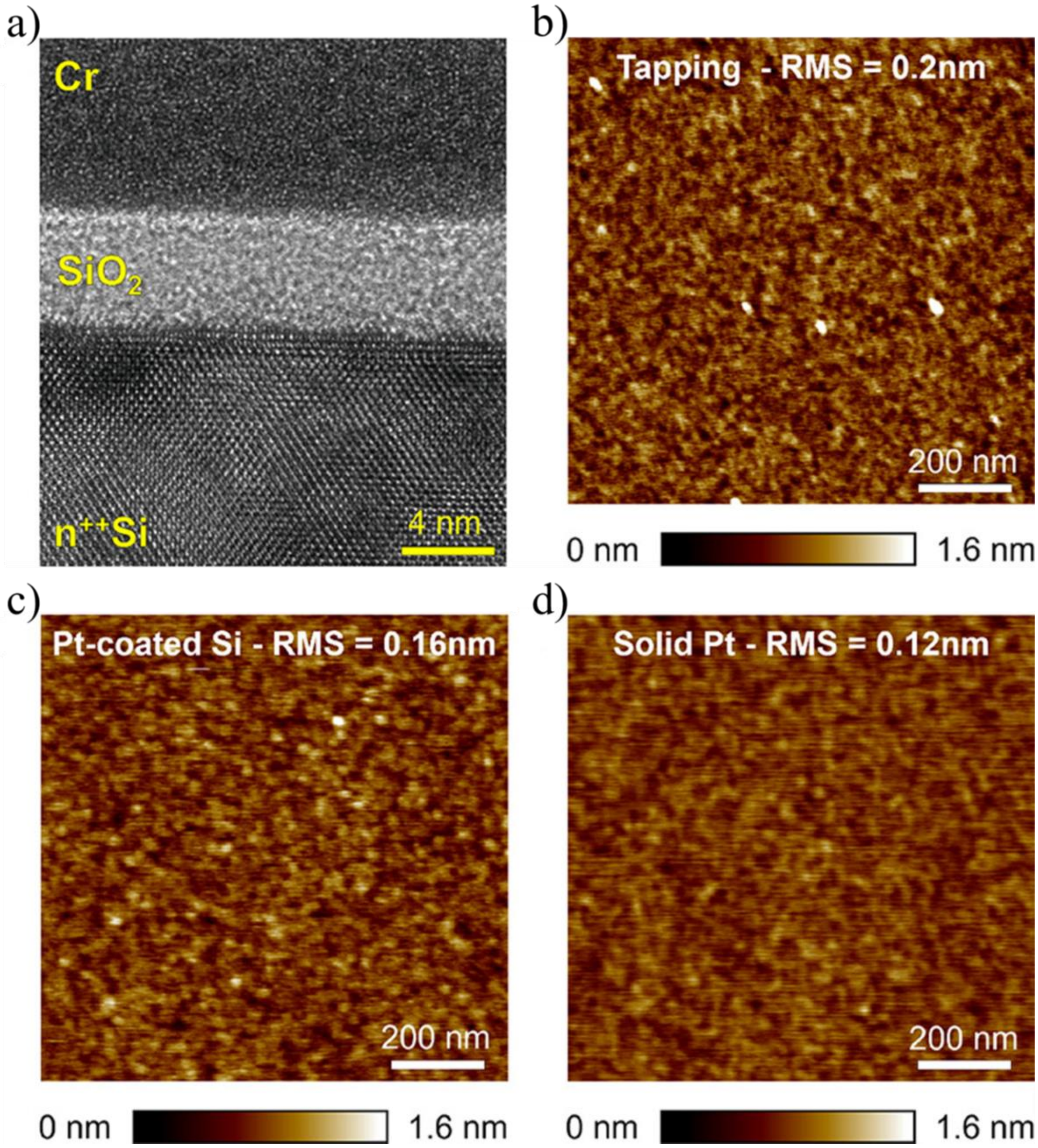

Figure 25: Assessment of surface roughness of a 4.7 nm SiO_2/n^{++} Si sample using diverse probes. a) Thickness and morphology of the SiO_2/n^{++} Si sample via TEM. Note that the top Cr layer is a prerequisite for the FIB preparation prior to TEM imaging. Topographic maps collected with b) a Si probe (NCHV-A) in tapping mode, c) a Pt/Ir-coated Si probe (ContV-Pt) in contact mode, and d) a solid Pt probe (RMN-25Pt300b) in contact mode. The surface roughness is indicated in each topographic map respectively. Adapted from [72], copyright American Chemical Society, 2023.

These roughness measurements are applicable for an area of 1 by 1 µm. It is important to note that while the topographic maps generated using both probes were of good quality, they were not as sharply defined as those obtained in tapping mode, which is a typical observation. One potential explanation for this could be a larger R_{TIP} of the solid Pt probe compared to the Si and Pt/Ir-coated Si probes. A higher R_{TIP} might result in less precise tracking of the sample's contours, particularly in areas with high aspect ratios, leading to a seemingly flatter surface profile. However, as shown in Figure 23, the R_{TIP} of solid Pt tips is generally slightly smaller than that of the Pt/Ir-coated Si tips. Another possibility is that the higher spring constant of the solid Pt tip enhances the tip/sample contact, contributing to the lower observed surface roughness. Despite these minor differences, all probe types demonstrate effective mapping capabilities for the ultra-flat surface topography of the SiO_2/Si sample.

Next the capability of solid Pt probes to measure the thickness of nanomaterials by analyzing their edges is evaluated, a common procedure in the study of various materials such as two-dimensional materials [223], polymers [224], and deoxyribonucleic acid (DNA) [225]. Topographic maps displayed in Figure 26 a,d and Figure 26 b,l were obtained using a silicon probe in tapping mode on different areas of a multilayer MoS_2 flake, which was mechanically exfoliated and transferred onto a 300 nm SiO_2/Si wafer. The flake's thickness at each probe-detected area was determined through post-processing of the images, employing a reliable method that involves analyzing the spectrum of the topographic images (see Figure 26 h-k and Figure 26 p-s), as described in [226]. The thickness measurements of the MoS_2 flake at areas 1 and 2 (shown in Figure 26 a,d and Figure 26 b,l) were found to be 16.73 nm and 16.03 nm, respectively, using the silicon probe. Upon repeating the experiments with other probes (see Figure 26 e-g and Figure 26 m-o), it was observed that the images collected were very similar, although the thickness measurements varied slightly, as detailed in the table in Figure 26 c. Generally, the conductive probes operating in contact mode (ContV-Pt, SCM-PIT-V2, and RMN25Pt-300b) yielded thickness values that were 4.1 to 15.4 % smaller compared to those obtained with the silicon probe in tapping mode. However, a detailed discussion on these minor differences is considered non-essential because: firstly, the differences are minimal and close to interatomic distances, and secondly, the effect of the flattening or plane fit in the step edge calculation is comparable. It can be confidently stated that the solid Pt probes deliver step edge values comparable to those obtained with Pt/Ir-coated probes, confirming their suitability for such experiments.

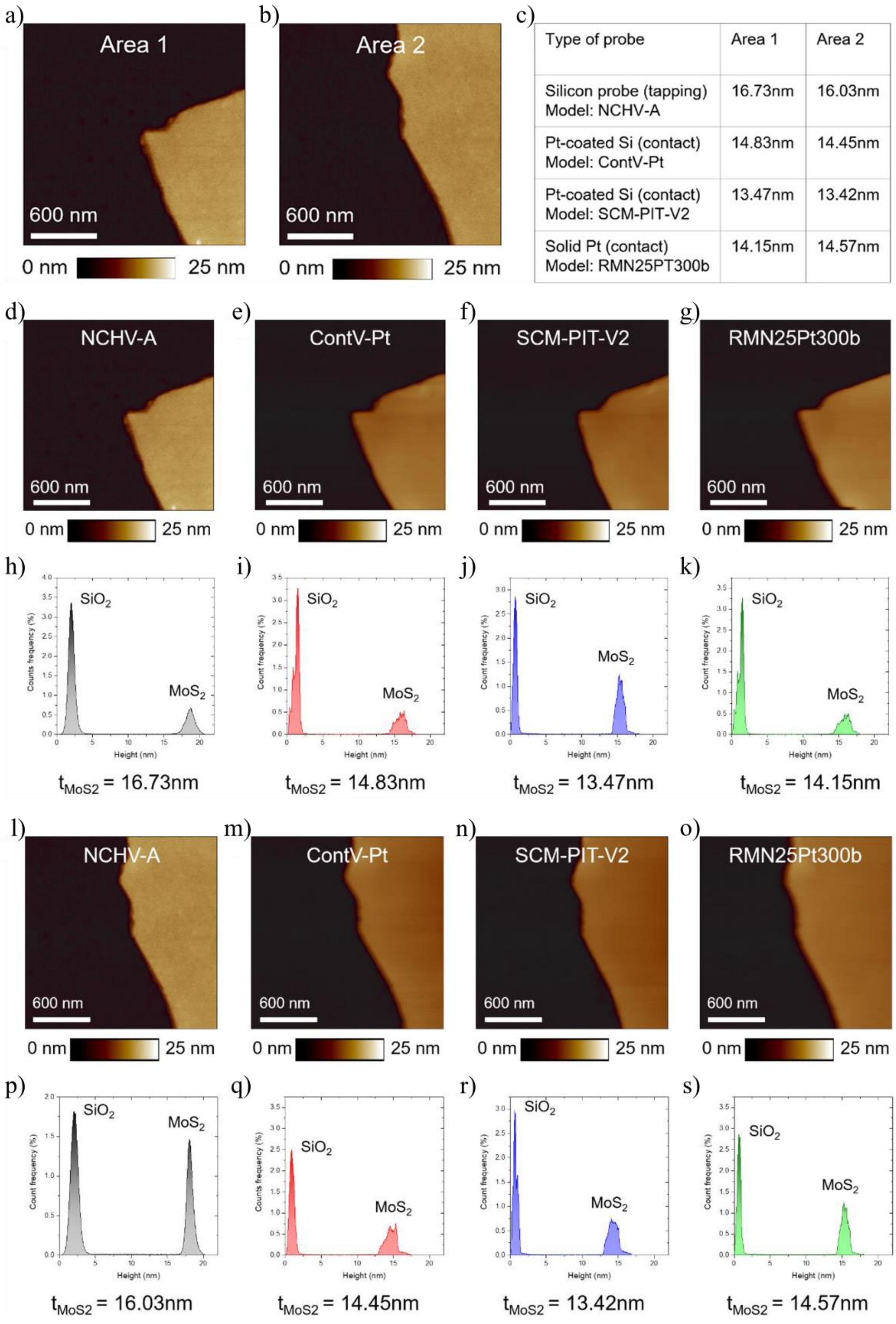

Type of probe	Area 1	Area 2
Silicon probe (tapping) Model: NCHV-A	16.73nm	16.03nm
Pt-coated Si (contact) Model: ContV-Pt	14.83nm	14.45nm
Pt-coated Si (contact) Model: SCM-PIT-V2	13.47nm	13.42nm
Solid Pt (contact) Model: RMN25PT300b	14.15nm	14.57nm

Figure 26: MoS2 flake thickness measured with different probes. a) Topographic map collected with a Si probe in tapping mode at location 1. b) Topographic map collected with a Si probe in tapping mode at location 2. c) Step height summary of both locations measured with four different types of probes. Thickness measurements at MoS_2 flake location 1 recorded with: d) A Si Probe (NCHV-A) in tapping mode. e) A Pt/Ir coated Si

probe with low spring constant (ContV-Pt) in contact mode. f) A Pt/Ir-coated Si probe with intermediate spring constant (SCM-PIT-V2) in contact mode. g) A solid Pt probe (RMN25Pt300b) in contact mode. The histograms of each topographic map h)-k) are displayed right below it. The step height t_{MoS_2} is defined as the distance between the highest points of the two peaks, corresponding to the surfaces of the substrate and the MoS_2 flake. Thickness measurements at MoS_2 flake location 2 recorded with: l) A NCHV-A in tapping mode. m) A ContV-Pt in contact mode. n) A SCM-PIT-V2 in contact mode. o) A RMN25Pt300b in contact mode. The histograms of each topographic map p)-s) are displayed right below it. Adapted from [72], copyright American Chemical Society, 2023.

The lateral resolution of current maps obtained with Pt/Ir-coated Si probes and solid Pt probes is analyzed through scans of the h-BN/Cu sample. For each probe type, the minimum voltage necessary to discern current above the noise level (V_{on}) is applied during scans. This voltage is 2 V for the solid Pt probe and 6 V for the Pt/Ir-coated Si probe. The observed voltage difference is likely attributable to the higher spring constant of the solid Pt probes, potentially facilitating a better, water-free contact. The aim of this experiment is to assess the capability of these two probe types to accurately map weak spots in the h-BN sample. Consequently, scan parameters for each probe are individually tailored. It is noteworthy that although various manufacturers provide Pt/Ir-coated Si probes, so far none offer a model with a spring constant k_C of 18 N/m, akin to the solid Pt probes used in this study, for electrical measurements in contact mode. Furthermore, even if probes with identical nominal spring constants were available, each would require optimization of scanning parameters, which could differ from one probe to another. Therefore, in this experiment, using different voltages for each probe type is considered acceptable, as long as they generate similar tunneling/leakage currents across the sample being tested. Employing identical scan parameters for probe comparison would lead to inaccurate results, as it would not represent the optimum operating conditions for each probe, and the currents driven would vary. A positive bias is deliberately applied to the C-AFM probe (relative to the substrate) to prevent local anodic oxidation, which could occur due to water splitting caused by electron injection from the tip [227]. The topographic maps generated using solid Pt probes exhibit a marginally fuzzier quality compared to those obtained with Pt/Ir-coated Si probes, a distinction that is evident upon comparing Figure 27 a with Figure 27 e. This observation aligns with previous findings in Figure 25 and Figure 26, and the level of fuzziness is generally within acceptable limits for most experimental applications. When examining the current maps, the quality of the images produced by both types of probes is notably similar. The resolution, characterized by the size and distribution of current spots, is comparable across both probe types at different current scales. However, it is observed that the currents measured with the solid Pt probe are slightly higher, as demonstrated in Figure 27 b, c, f, and g. This similarity in resolution, despite the minor difference in current intensity, underscores the effectiveness of both probe types in conducting such measurements.

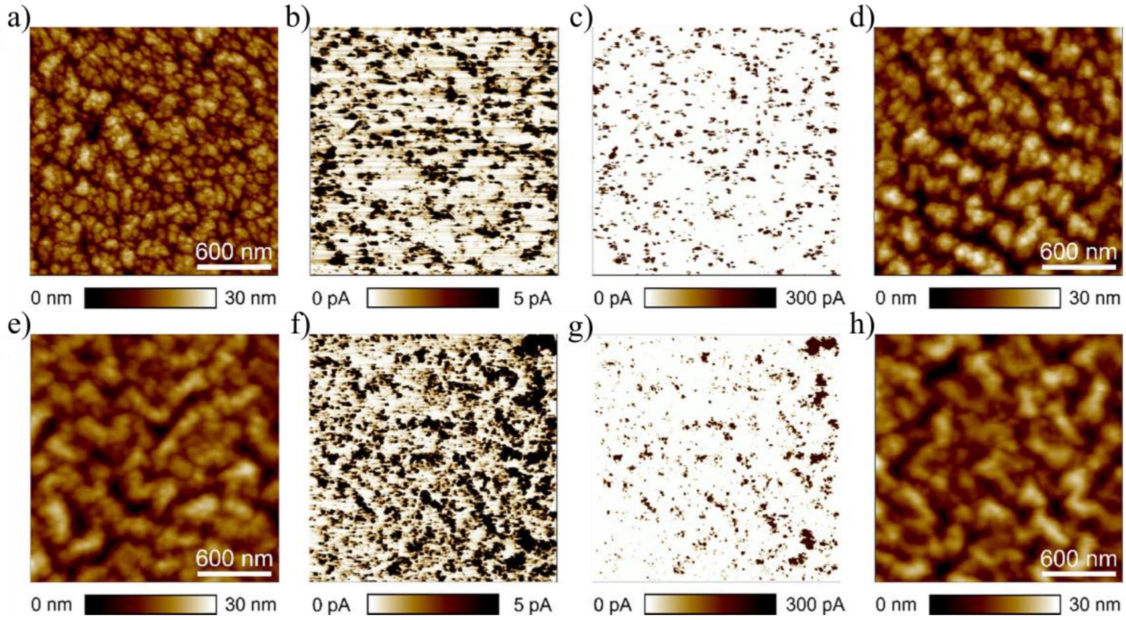

Figure 27: Assessment of electrical lateral resolution using Pt/Ir-coated and solid Pt probes: The images presented in this section are divided into two sets, with the top row showcasing data from Pt/Ir-coated Si probes (ContV-Pt) and the bottom row featuring data from solid Pt probes. a) Topographic and b) current maps collected simultaneously on an h-BN/Cu sample using a Pt/Ir-coated probe. c) Same current map than b) but with a different current scale. d) Topographic map collected on an h-BN/Cu sample using a Pt/Ir-coated probe after five subsequent current scans. The voltage applied in panels (a–d) is 6 V. e) Topographic and f) current maps collected simultaneously on an h-BN/Cu sample using a solid Pt probe. g) Same current map than f) but with a different current scale. h) Topographic map collected on an h-BN/Cu sample using a solid Pt probe after five subsequent current scans. The voltage applied in panels (e–h) is 2 V. Adapted from [72], copyright American Chemical Society, 2023.

The durability of the topographic imaging quality with the solid Pt probe is noteworthy, as it remains consistent even after multiple scans (as evident when comparing Figure 27 e and Figure 27 h). In contrast, the Pt/Ir-coated Si probe exhibits a noticeable decline in lateral resolution over time, with certain topographic features, such as cavities, becoming less discernible in later scans (this can be seen when comparing Figure 27 a and Figure 27 d). Since the currents detected during these experiments are relatively low (<1 nA), it is inferred that the observed degradation in image quality is primarily due to the wear and tear of the probe tips, likely caused by mechanical friction during the scanning process, rather than electrical factors.

Subsequently the durability of solid Pt probes in comparison to Pt/Ir-coated Si probes is analyzed by applying ramped voltage stresses (RVS) ranging from 0 to 10 V to the C-AFM tip, while keeping the substrate grounded, at 100 randomly selected locations on a 3.4 nm $SiO_2/n^{++}Si$ sample. Such stress leads to a significant increase in current at the tip/sample junction and often triggers the dielectric breakdown (DB) of the SiO_2 film, which can induce surface epitaxy [182, 228]. To prevent electrical stress from one RVS influencing the current measured in subsequent RVS, a safe distance of 1 µm is maintained between each stressed site. Initially, 100 I-V curves are collected using a Pt/Ir-coated Si probe (R_{TIP} = 27.2 nm, as shown in Figure 28 a). A notable decrease in registered currents is observed as the stress progresses. Around the 50th I-V curve, the probe ceases to trigger hard-DB events (as depicted in Figure 28 b and Figure 28 c). This indicates a significant loss of conductivity in the Pt/Ir-coated probe tip during the initial RVS, attributed to the harsh nature of the hard-DB, which subsequently affects the currents measured in later RVS. This conclusion is further supported by dramatic tip degradation, evident in SEM images taken after the stress tests (Figure 28 d). These images reveal both the melting of the metallic Pt varnish (indicated by the presence of spherical particles) and the removal of Si volume. This observation aligns with findings reported in earlier studies [90], highlighting the challenges in maintaining probe integrity under aggressive electrical stress conditions. The experiment was then repeated using a solid Pt probe, initially featuring an R_{TIP} of 29.1 nm (as indicated in Figure 28 e). Analysis of the forward I-V curves (Figure 28 f) revealed a high degree of homogeneity in the sample, with only minor random variations in V_{ON} attributable to inhomogeneities within the $SiO_2/n^{++}Si$ sample. Following the I–Vs, a topographic map was recorded (shown in Figure 28 g), indicating that a hard dielectric breakdown (hard-DB) event occurred at most locations. This outcome suggests that despite the apparent degradation of R_{TIP} (evident in Figure 28 h), the probe retained sufficient conductivity. Consequently, the data collected remain valid, affirming that the probe can continue to be utilized for I-V curve recordings. However, it's important to note that the probe, given its current condition, may not be ideal for measuring lateral scans, as the degraded R_{TIP} could impact the quality and accuracy of such measurements.

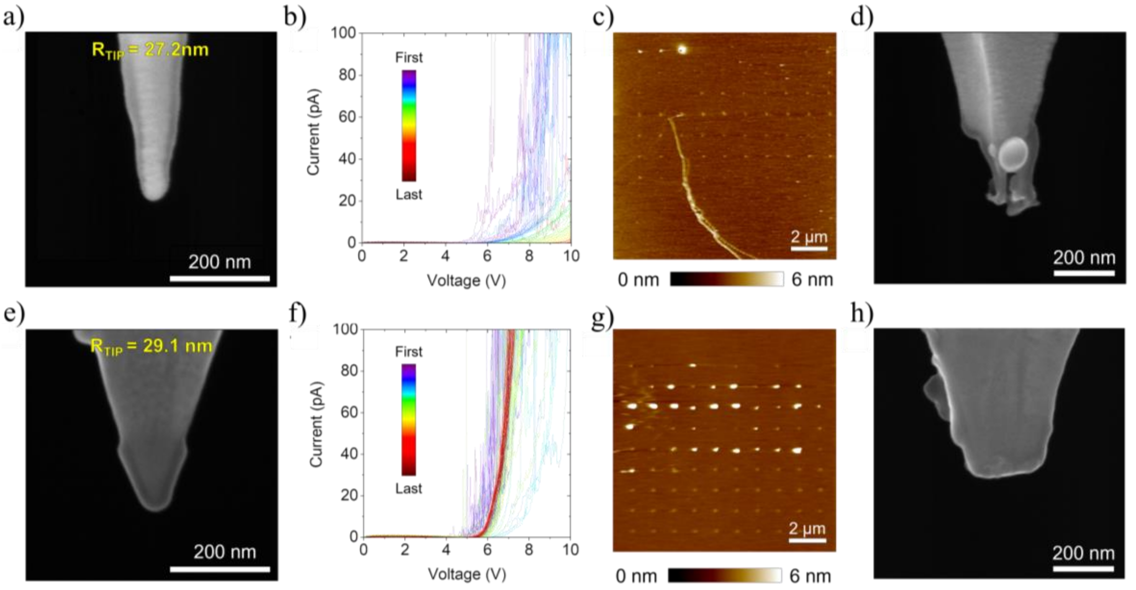

Figure 28: Comparative durability study of Pt/Ir-coated Si probes and solid Pt probes. The data in the top row corresponds to the Pt/Ir-coated Si probes (ContV-Pt); the data in the bottom row corresponds to the solid Pt probes. SEM images of a Pt/Ir-coated Si tip before a) and after d) measuring 100 I–V curves at different locations of a 3.4 nm SiO_2/n^{++} Si sample. b) A declining trend is evident in the I–V curves, and the subsequent topographic AFM map c) indicates that around the 50th I–V curve, the probe becomes incapable of triggering further hard-DB events. d) Post-stress SEM imaging reveals extensive damage to the probe, characterized by the melting of the metal coating (noted by spherical particles) and the removal of Si volume. SEM images of a solid Pt tip before e) and after h) measuring 100 I–V curves at different locations of a 3.4 nm SiO_2/n^{++} Si sample. f) The post-stress topographic AFM map suggests that hard-DB was induced at nearly all locations, evidenced by visible surface epitaxy. h) The post-stress SEM image shows that the tip has become dull but remains functional, as indicated by the lack of a progressive current reduction in the I–V curves in f). This implies that, despite some physical alterations, the solid Pt probe maintains its effectiveness and can still be used for further I–V curve measurements. Adapted from [72], copyright American Chemical Society, 2023.

Finally, the probe-to-probe deviation is analyzed. This assessment involves collecting 100 I–V curves at various locations on the 5.6 nm SiO_2/n^{++} Si sample using three distinct new solid Pt probes and a current limitation of 100 pA. The results, as depicted in Figure 29, reveal that the deviation of V_{ON} from one probe to another is relatively minor. Specifically, the V_{ON} values recorded are 8.18 V ± 0.21 V, 7.68 V ± 0.19 V, and 7.66 V ± 0.27 V. These variations are comparable to, or even smaller than, those observed with Pt/Ir-coated Si probes [176]. Such consistency underscores the high reproducibility of measurements obtained using solid Pt probes. This finding is particularly significant considering the inherent and unavoidable variations in spring constant (k_C) and R_{TIP} that are characteristic to all types of C-AFM probes. Therefore, the data variability seen across different solid Pt probes is deemed not to be a significant concern for the accuracy and reliability of the measurements.

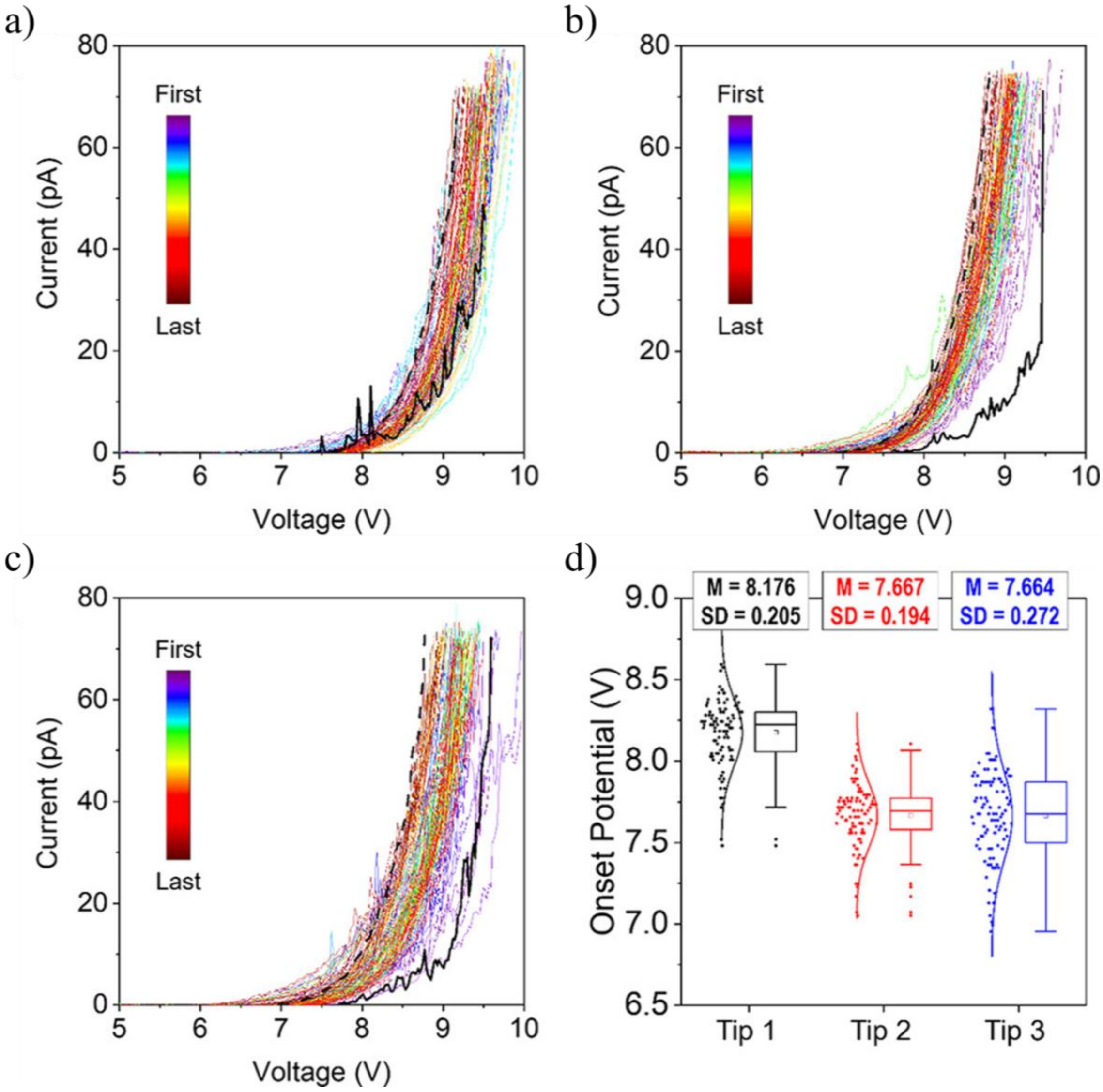

Figure 29: Solid Pt probe-to-probe variability. a)-c) Forward I–V curves recorded at 100 different locations of a 5.6 nm SiO_2/n^{++} Si sample using three different solid Pt probes (RMN-25Pt300b). In each graph, the initial I–V curves are denoted by thicker black solid lines, while the final I–V curves are indicated by black dashed lines. This depiction highlights that there is no discernible tip degradation (e.g., no downward trend in the curves) throughout the course of the measurements. (d) Statistical analysis of V_{on} (extracted at 3 pA). M and SD represent the mean value and the standard deviation of the distribution, respectively. Adapted from [72], copyright American Chemical Society, 2023.

In C-AFM, measurement reliability often faces challenges due to the limited durability of Pt/Ir-coated Si probes. While diamond-coated or solid diamond probes offer greater durability, their high cost and excessive stiffness, which can damage many samples, limit their practicality. This study has identified that solid Pt probes (R_{TIP} < 20 nm, $k_C \approx$ 18 N/m) are a highly effective alternative, offering lateral resolution comparable to Pt/Ir-coated Si probes but with the significant advantage of a markedly extended lifespan. Additionally, these probes demonstrate minimal variability in electrical data from one probe to another. Therefore, solid Pt probes emerge as a potential key solution for scientists seeking to enhance the reliability and cost-effectiveness of their C-AFM research, balancing performance with economic and material considerations. The insights of this chapter have been published in [72].

4.2 Current-Limited C-AFM

In C-AFM, to reduce the risk of tip damage due to high current densities, an effective strategy is to limit the resultant currents, rather than solely relying on more robust solid Pt probes. This approach not only protects the probe but also minimizes current-induced damage to the sample's surface [229]. Consequently, it opens up possibilities for investigating a wider array of phenomena. These include the characterization of delicate materials like polymer blends [230, 231], which are crucial in charge transport for organic solar cells. Additionally, it allows for the measurement of self-accelerated current phenomena such as dielectric breakdown and resistive switching [130, 228]. Moreover, this technique facilitates the probing of local defects in complex heterostructures, like aluminum gallium nitride / gallium nitride (AlGaN/GaN) [232] and cubic silicon carbide (3C-SiC) layers [233], as well as in two-dimensional materials such as MoS_2 [234, 235]. Such investigations are vital for understanding the properties and behaviors of these materials in various applications. Finally, the controlled limitation of currents can enhance the precision in oxide growth during nano-lithography processes [236]. Traditionally, this is achieved by integrating a resistor in series with the tip [237-239]. While this method effectively limits currents at the nanoprobe/sample junction, it demands prior knowledge of the sample's resistance to select an appropriate resistor value, which may not always be readily available. Furthermore, depending on the specific C-AFM model, setting up this configuration can be cumbersome. This complexity is compounded by the need for different resistors for various samples, and the potential introduction of additional parasitic capacitance. As an alternative, the implementation of a software-based current limitation system is proposed. The forthcoming Chapter 4.2.1 will discuss the working principle, benefits, and constraints of such a system, featuring the Bruker Dimension Icon. Subsequently, Chapter 4.2.2 will introduce an innovative sample holder, incorporating a CMOS transistor designed to limit currents in C-AFM applications, showcasing a novel approach to current management in these investigations.

4.2.1 Software-Based Current Limitation

To analyze the effectiveness and the underlying working principle of software-based current limitation tunneling current across a reference ultra-thin dielectric by applying electrical stresses at hundreds of randomly selected positions were studied. Thereto an AFM (Dimension Icon, Bruker, Massachusetts, USA), equipped with a Nanoscope VI controller and a PFTUNA module is employed. The AFM operates under ambient conditions at a temperature of 22°C. The study utilizes four distinct types of nanoprobes, encompassing one electrically insulating and three conductive variants. The first type, the electrically insulating Bruker ScanAsyst-Air [240] (nominal R_{TIP} = 2 nm, k_C = 0.4 N/m), consists of sharp silicon nitride (SiN) probes. These probes are designed for high-resolution topographic scans and exert minimal force on the sample due to their low spring constant. The second type is the Bruker ContV-Pt [16] (nominal R_{TIP} = 25 nm, k_C = 0.2 N/m), which are silicon probes coated with platinum/iridium (Pt/Ir) on the tip and the cantilever front side, suitable for electrical measurements in contact mode. The third type, the Bruker SCM-PIT-V2 [17] (nominal R_{TIP} = 25 nm, k_C = 3 N/m), also features a Pt/Ir coating on silicon but with a higher spring constant. The fourth type is the RMN-25Pt300b [88], produced by Rocky Mountain Nanotechnology (nominal R_{TIP} = 20 nm, k_C = 18 N/m), also intended for electrical measurements in contact mode. Both the tip and cantilever of this probe are made from solid platinum. It is important to note that some manufacturers do not specify tolerances for the R_{TIP}, and variations can significantly exceed 100% of the nominal value provided by the manufacturer [18]. Therefore, experimental characterization of R_{TIP} for different tips may yield values that diverge from those specified by the manufacturer, highlighting the need for e.g., SEM validation in precision measurement applications. For this experiment two distinct types of samples were chosen. The first type of sample is industrial-quality, 3.4 nm thick silicon dioxide (SiO_2), created via rapid thermal oxidation on highly conductive n-type (100) silicon. This silicon is arsenic-doped and features a resistivity of 0.0025-0.0035 Ω·cm. The fabrication process for these samples, refined over the past 30 years, allows for precise control over thickness at the atomic level. Such precision results in samples characterized by minimal impurities, minimal thickness fluctuations, and sharply defined interfaces. An example of this process's outcome is evident in a 5.6 nm thick SiO_2 sample (shown in Figure 30 a) via TEM (Titan ST, FEI, Oregon, USA), although the specific sample used in this study was 3.4 nm thick, which was verified through ellipsometry (Therma-Wave Optiprobe 3290DUV, KLA Corporation, California, USA). The use of a highly doped substrate in these samples is beneficial to eliminate the potential difference that would be present in a standard silicon substrate [197]. The second type of sample is a 10-layer-thick stack of hexagonal boron nitride (h-BN), approximately 3.3 nm in thickness, produced via chemical vapor deposition (CVD) on copper foil [221]. In contrast to the SiO_2 sample, the h-BN stack exhibits a rougher texture and possesses a significant number of local defects. These characteristics make it an excellent candidate for current mapping experiments and for assessing the closed loop system's ability to limit current at defect sites during scanning.

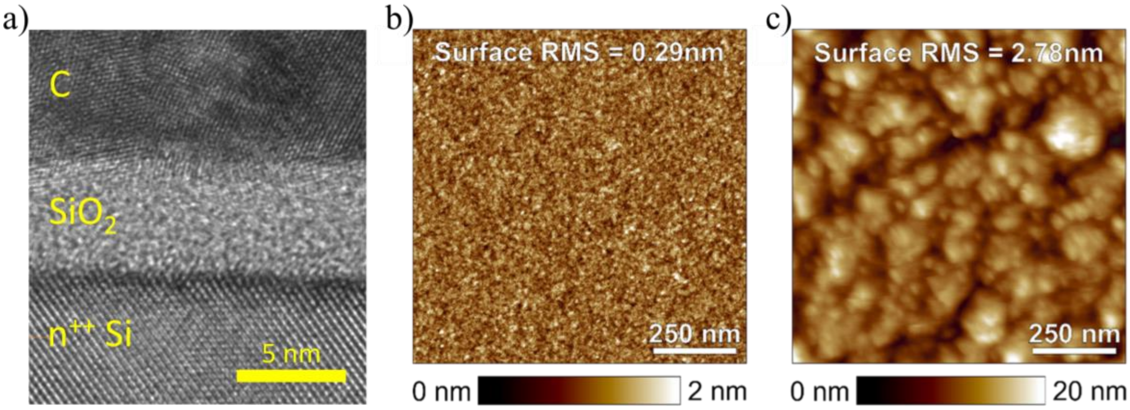

Figure 30: Sample roughness. a) TEM image unveiling the thickness and morphology of a 5.6 nm SiO_2/n^{++} Si sample. Note: the top C layer is a prerequisite for the FIB preparation prior to TEM imaging. b) Topographic map of 3.4 nm SiO_2/n^{++} Si. c) Topographic map of 10-layer-thick (~3.3 nm) CVD-grown hexagonal boron nitride (h-BN) on Cu foil. Adapted from [14], copyright American Chemical Society, 2023.

All experiments were conducted using the Bruker Dimension Icon in an air atmosphere. The procedure involved the application of ramped voltage stresses (RVS) to the sample holder while maintaining the probe tip grounded and in static contact with the sample at a single position for the duration of each RVS. Each RVS sequence included ramping the voltage from 0 V to a predetermined maximum negative voltage ($-V_{MAX}$) and then reducing it back to 0 V. Concurrently, the current was recorded to generate current versus voltage (I-V) plots. The use of negative voltage on the sample holder is a common practice designed to prevent local anodic oxidation. This phenomenon occurs when electrons, injected from the tip under a positive bias, interact with the water meniscus typically formed at the tip/sample junction in an air atmosphere. For ease of understanding and clarity in this chapter, both the applied voltages and the measured currents are presented in absolute values. Multiple sample locations were tested, following a 10x10 matrix pattern with 1 µm distance between each RVS location, chosen randomly across the sample. Current-limited RVS and current-limited current maps are implemented using the Trigger menu of the Nanoscope software (Version 10, Bruker, Massachusetts, USA), which operates the AFM. In this setting, the RVS halts at the voltage level (V_{STOP}) that induces currents exceeding a pre-set threshold. However, it is important to note that a backward voltage curve from V_{STOP} to 0 V is automatically executed, and this part of the process is not current-limited. For analyzing currents during RVS with high temporal resolution, two methods are utilized: Firstly, the High-Speed Data Capture (HSDC) feature of the Nanoscope software, capable of capturing one current data point every 2 µs, and secondly, an Oscilloscope (InfinitiVision MSOX3024G, Keysight, California, USA) is connected to the low-frequency outputs of the AFM's controller to monitor voltage and current signals. Note that the oscilloscope output is a voltage signal that needs to be converted into current by multiplying with the chosen current sensitivity. The oscilloscope is connected to the controller via coaxial cables and set to trigger mode with a data capture rate of 10 µs. A 0.5 V voltage flank from the C-AFM voltage ramp is used as the trigger signal, and the time base offset is adjusted to 0.5 s. This setup ensures that the entire voltage sweep is captured and synchronized with the C-AFM voltage ramp, given the known ramp frequency. Additionally, current-limited scans are conducted using the Closed Loop menu of the Nanoscope Software. In the absence of current limitation, the selected voltage is directly applied to the sample. Conversely, when current limitation is activated, a current-limited RVS (up to V_{STOP}) is applied at every pixel within the scan area. The impact of electrical stress on the utilized probe tips is meticulously examined using a SEM (Magellan 400, FEI, Oregon, USA). This analysis enables a detailed observation of any structural changes or damage incurred by the tips during the experiments. Additionally, to assess the cross-sectional morphology of a SiO_2/Si sample, a TEM (Titan ST, FEI, Oregon, USA) is employed. Prior to TEM analysis, a focused ion beam (FIB, Helios Nanolab 450S, FEI, Oregon, USA) is used for the precise extraction of a thin lamella from the sample.

Initially the surface roughness of the samples is examined. For this purpose, the ScanAsyst-Air probe is employed in ScanAsyst Mode, a setting that facilitates precise and dynamic force control by recording force-distance curves at each pixel of the scanned area [43]. During scans covering a 1 µm × 1 µm area, the RMS roughness of the SiO_2/Si sample is found to be exceptionally low, at 0.29 nm (as shown in Figure 30 b), aligning with findings from previous studies [222, 241]. In contrast, the RMS roughness of the h-BN/Cu sample is markedly higher, measuring at 2.78 nm. This increased roughness is primarily attributed to the corrugations of the underlying Cu substrate, as illustrated in Figure 30 c.

Subsequently RVS is applied to the 3.4 nm thick SiO_2/n^{++} Si sample using three conductive nanoprobes: ContV-Pt, SCM-PIT-V2, and RMN-25Pt300b. Figure 31 d-f display 100 forward I-V curves for each type of tip, where the voltage is ramped up from 0 V to 10 V. A color scale in these figures helps distinguish the number of currents detected as stress progresses. The experiments were conducted with a deflection setpoint of 0.2 V and a ramp frequency of 0.3 Hz. A distance of 1 µm between each tested location was kept to avoid point-to-point interference. In these studies, displacement current has been subtracted from the I-V curves, as it results from the system's capacitance and does not relate to charge carriers moving through the sample. The onset potential (V_{on}) of the I-V curves is calculated for comparison across nanoprobes. V_{on} is the voltage at which currents exceed 3 pA, a threshold chosen for being well above the system's noise level [19] yet sufficiently low to detect tunneling events as soon as they occur. Experiments are conducted first without current limitation and then repeated with a current limitation system set to 100 pA, using new probes for both sets of experiments. SEM is utilized to examine the shape of the nanoprobes both before and after the experiments. Additionally, the sample's post-stress surface is analyzed by collecting topographic maps with the C-AFM. The data from before and after the stress are showcased in Figure 31 a-c and Figure 31 j-l, respectively.

Without current limitation, the ContV-Pt probe was capable of measuring 14 I-V curves, where V_{on} was determined to be 6.1 ± 0.2 V. Subsequently, the probe lost its conductivity abruptly, as illustrated in Figure 31 d. This observation aligns with the post-stress topography scans, where no additional hillocks, indicative of dielectric breakdown induced epitaxy spots in the SiO_2 film [182, 228], were identifiable beyond position 14 (refer to Figure 31 g). The appearance of hillocks, triggered by high currents flowing through the film, confirms that the probe remained conductive during those measurements.

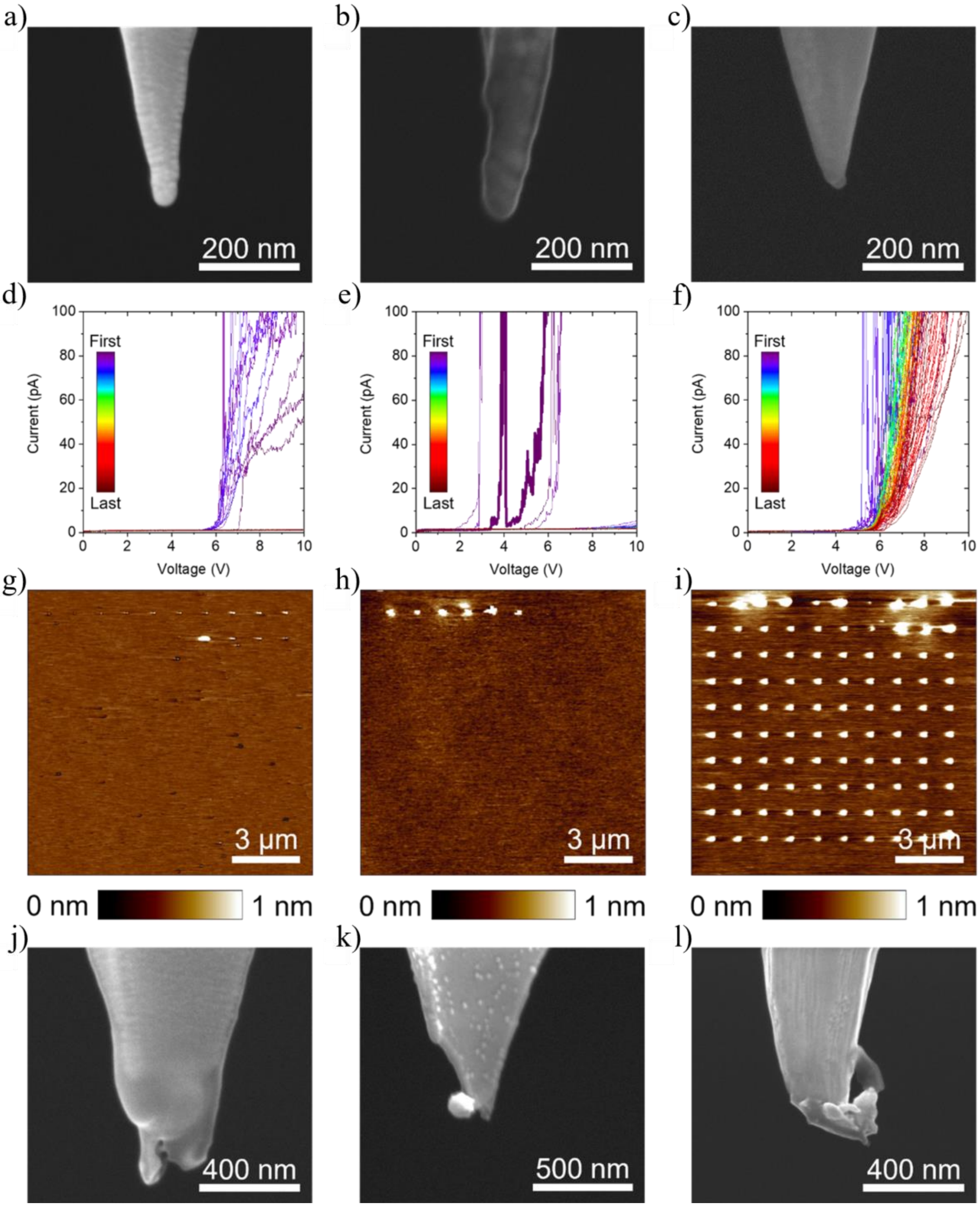

Figure 31: RVS experiments on SiO_2 without current limitation. Pre-stress SEM investigations for a) ContV-Pt, b) SCM-PIT-V2, and c) RMN-25Pt300b. 100 attempted I-V curves at various sample locations using d) ContV-Pt, e) SCM-PIT-V2, and f) RMN-25Pt300b. Post-stress topography measurements conducted with g) ContV-Pt, h) SCM-PIT-V2, and i) RMN-25Pt300b. Finally, post-stress SEM examinations of j) ContV-Pt, k) SCM-PIT-V2, and l) RMN-25Pt300b. Adapted from [14], copyright American Chemical Society, 2023.

Post-stress SEM images of the ContV-Pt probe reveal significant damage; the coating appears molten, and the silicon base material is exposed (Figure 31 a,m). In a similar scenario, the SCM-PIT-V2 probe lost its conductivity after the 6th RVS curve. This loss of conductivity is evident from the near-zero currents in the subsequent I-V curves (Figure 31 e), the presence of only six hillocks in the post-stress topographic maps (Figure 31 h), and the physical breakdown of the probe's apex with a sphere of molten Pt/Ir film visible in the SEM images (Figure 31 k). These findings might indicate that the Pt-Ir coating on the SCM-PIT-V2 probe may be less stable [18]. In contrast, the RMN-25Pt300b demonstrated high currents in all 100 I-V curves, causing saturation in the electronics of the C-AFM (refer to Figure 31 f). The V_{on} value was measured at 5.7 ± 0.23 V, lower than that achieved with ContV-Pt tips. This reduction may be attributed to either a higher spring constant or the enhanced conductivity of the solid Pt bulk material, as opposed to the Pt-Ir thin coating used in the other tip types. Notably, the RMN-25Pt300b was the only probe to exhibit currents during all 100 RVS tests, showing a gradual shift of V_{on} towards higher potentials and a decrease in slope as the stress continued. Subsequent topography scans post-stress indicated significant surface epitaxy at all 100 I-V locations (see Figure 31 i), further confirming the probe's conductive state post-testing. However, post-stress SEM analysis (Figure 31 c,l) revealed considerable damage in the form of a dulled apex and droplets of molten Pt to the RMN-25Pt300b consisting. Despite this, the RMN-25Pt300b's composition of solid Pt maintains its conductivity, potentially allowing further RVS tests or current map recordings, when lateral resolution is not a primary concern.

The experiments outlined in Figure 31 d-i were replicated, and a notable consistency emerged: all tested solid Pt tips (RMN-25Pt300b) withstood the RVS and maintained good conductivity after 100 I-V curves. In contrast, the ContV-Pt and SCM-PIT-V2 tips exhibited much faster degradation. Variability was observed in the number of I-V curves recordable by each ContV-Pt tip and SCM-PIT-V2 tip, respectively. Degradation among the ContV-Pt and SCM-PIT-V2 tips ranged from abrupt to gradual. Additionally, some ContV-Pt tips proved to be more durable than certain SCM-PIT-V2 tips, and vice versa. However, no clear trend emerged indicating a superior performance of ContV-Pt tips over SCM-PIT-V2 tips in terms of recording more I-V curves, or the reverse. These data are omitted to avoid confusion. The overarching and consistent conclusion from these experiments is the superior durability and conductivity retention of the RMN-25Pt300b under stress. To elucidate the cause of tip degradation during RVS, tests were repeated using a reduced current sensitivity of 100 nA/V. This adjustment allowed for current measurements up to approximately 536 nA. Additionally, backward I-V sweeps were analyzed using the standard AFM capture, the HSDC menu, and an oscilloscope. This approach provided two additional high-precision current monitoring sources, facilitating a comparison with the standard Nanoscope capture results. Under this configuration, it was observed that the current during the backward sweep frequently reached the saturation level of approximately 536 nA (refer to Figure 32). This suggests that the actual currents passing through the tip/sample junction might well exceed tens or hundreds of microamperes. Such high current levels likely contribute to the significant degradation observed in the apices of the tips (as shown in Figure 31 j-l).

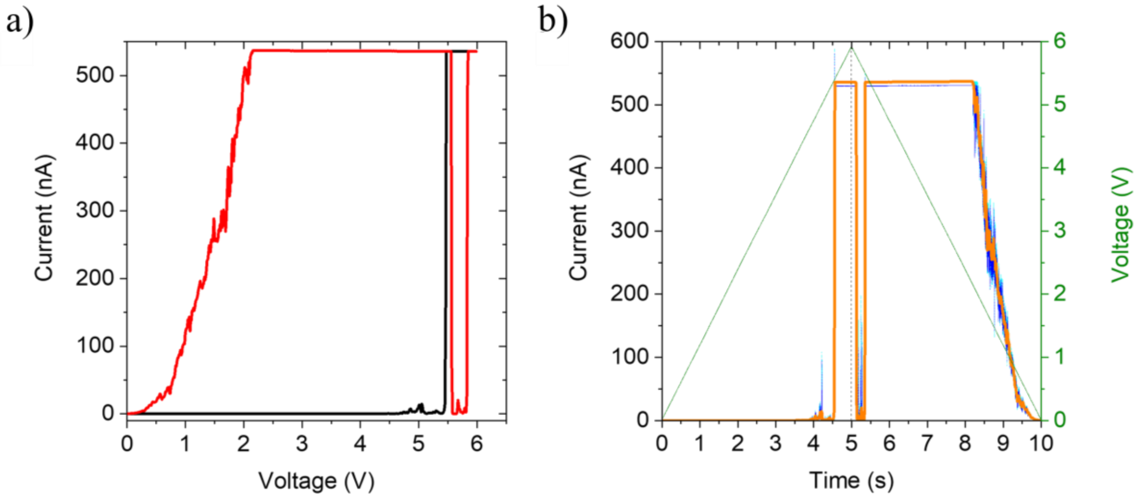

Figure 32: a) An exemplary I-V curve comprising 512 data points, with a current sensitivity of 100 nA/V and no current limitation on SiO_2. The forward sweep is shown in black, while the backward sweep is depicted in red. (b) The corresponding I-T representation, illustrated by an orange solid line, is overlaid with results from the HSDC (cyan dashed line) and the Oscilloscope (blue dotted line). Additionally, the applied voltage ramp is marked by a green line, and the end of the forward sweep is indicated by a black vertical dashed line. Adapted from [14], copyright American Chemical Society, 2023.

When the current limitation was activated, all I-V curves effectively halted upon surpassing 100 pA, though each curve may have reached a slightly different peak value. Uniform current rise characteristics were observed at all locations for all tips (see Figure 33 d-f). Importantly, there was no evidence of dielectric breakdown in the SiO_2, as indicated by the absence of hillocks in subsequent topographic maps (Figure 33 g-i). The V_{on} value in this scenario remained quite stable, showing no trend towards higher values, and was comparable across all tips. However, a minor decrease in V_{on} was noted for tips with higher spring constants. The variability in V_{STOP} mirrored that of V_{on} for all tips, which aligns with the understanding that the tunneling current across SiO_2 increases exponentially [115].

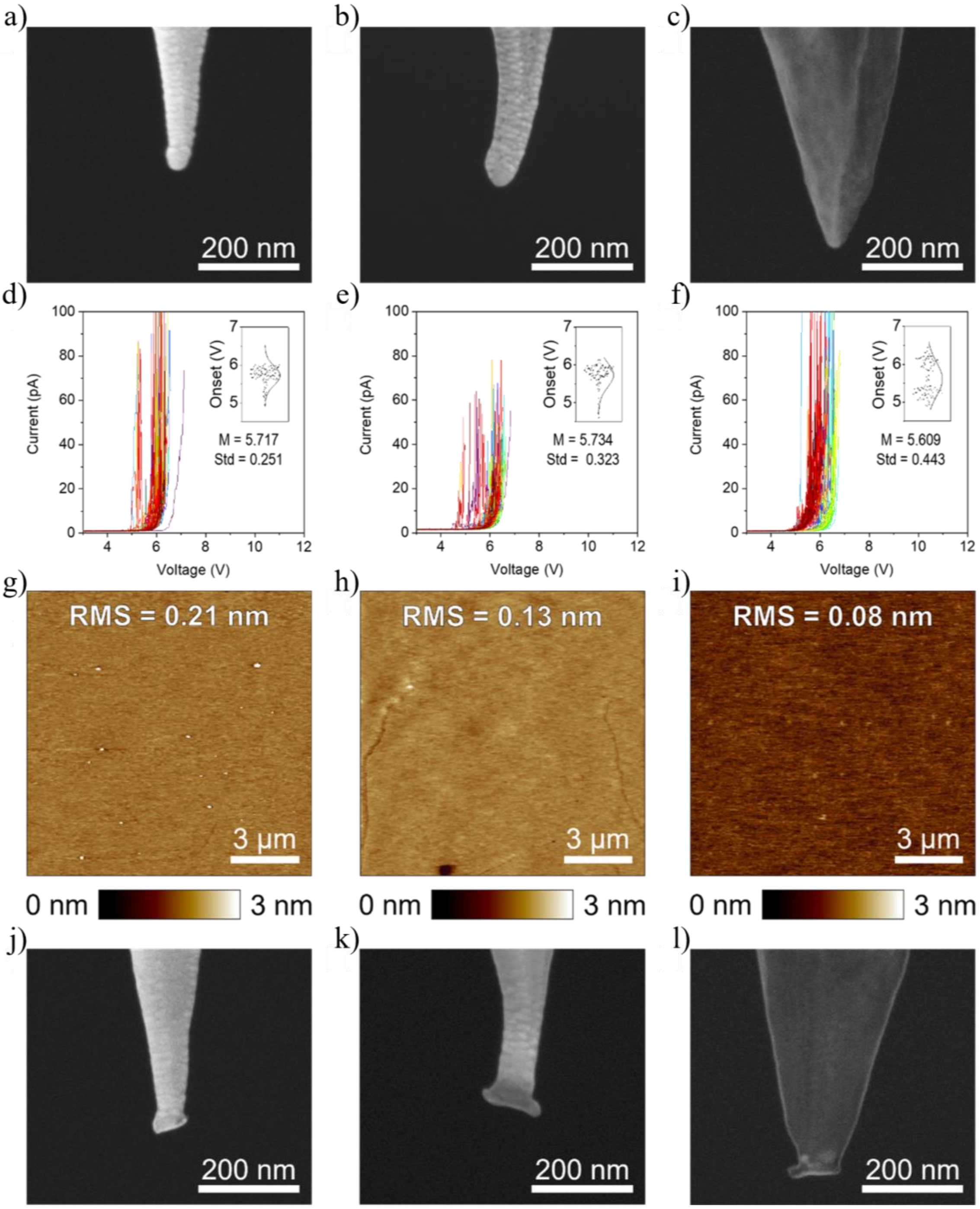

Figure 33: RVS on SiO_2 with current limitation. It includes pre-stress SEM investigations of a) ContV-Pt, b) SCM-PIT-V2, and c) RMN-25Pt300b. 100 attempted I-V curves at various sample locations using d) ContV-Pt, e) SCM-PIT-V2, and f) RMN-25Pt300b, with insets showing onset potentials at 3pA. M indicates the mean onset voltage, and Std denotes the standard deviation. Post-stress topography measurements are recorded with g) ContV-Pt, h) SCM-PIT-V2, and i) RMN-25Pt300b. Post-stress SEM investigations for j) ContV-Pt, k) SCM-PIT-V2, and l) RMN-25Pt300b. Adapted from [14], copyright American Chemical Society, 2023.

The post-stress SEM images indicate that all nanoprobes incurred minor damage, potentially diminishing their lateral resolution in current map recordings (see Figure 33 j-l). This damage is not attributed to lateral friction, as the RVS was executed in a spectroscopic mode, followed by only a single topography scan employing a comparatively low contact force. Therefore, the modifications in tip appearance, as seen when comparing Figure 33 a-c with Figure 33 j-l, are solely linked to the high current densities experienced during the I-V curves, which reached approximately 100 A/cm². No substantial damage to the tip coating was observed. The ability to extract onset potentials from all 100 I-V curves suggests that the tips remained conductive. Indeed, under the same parameters, it was possible to record an additional 490 I-V curves using the ContV-Pt and 138 I-V curves with the SCM-PIT-V2, before observing a significant increase in the V_{on} value that hindered further measurements (refer to Figure 34). A probe is considered non-conductive if, despite applying 10 V of sample bias, it fails to surpass a current threshold of 10 pA in ten consecutive I-V curves. The current-limited RVS protocol, ranging from 0 V to V_{STOP} and back to 0 V, effectively safeguards the apex of all nanoprobes. In contrast, the same RVS measurement without current limitation, moving from 0 V to V_{MAX} and then returning to 0 V, not only damages the apex of the tips but also induces surface epitaxy in the SiO_2 sample. Additionally, the electrical data, particularly the I-V curves, exhibited markedly fewer fluctuations. While the current-limitation system does not precisely limit the current across the sample to a specific value, its adept calculation and application of V_{STOP} during RVS proves highly beneficial. A skilled C-AFM user might manage to perform numerous RVS measurements without current limitation by judiciously choosing a V_{MAX} near V_{STOP}. However, such manual selection cannot match the precision achieved by the automated system. Despite the advantages of this current-limitation system, some degree of tip degradation is still noticeable, as evidenced in Figure 33 j-l.

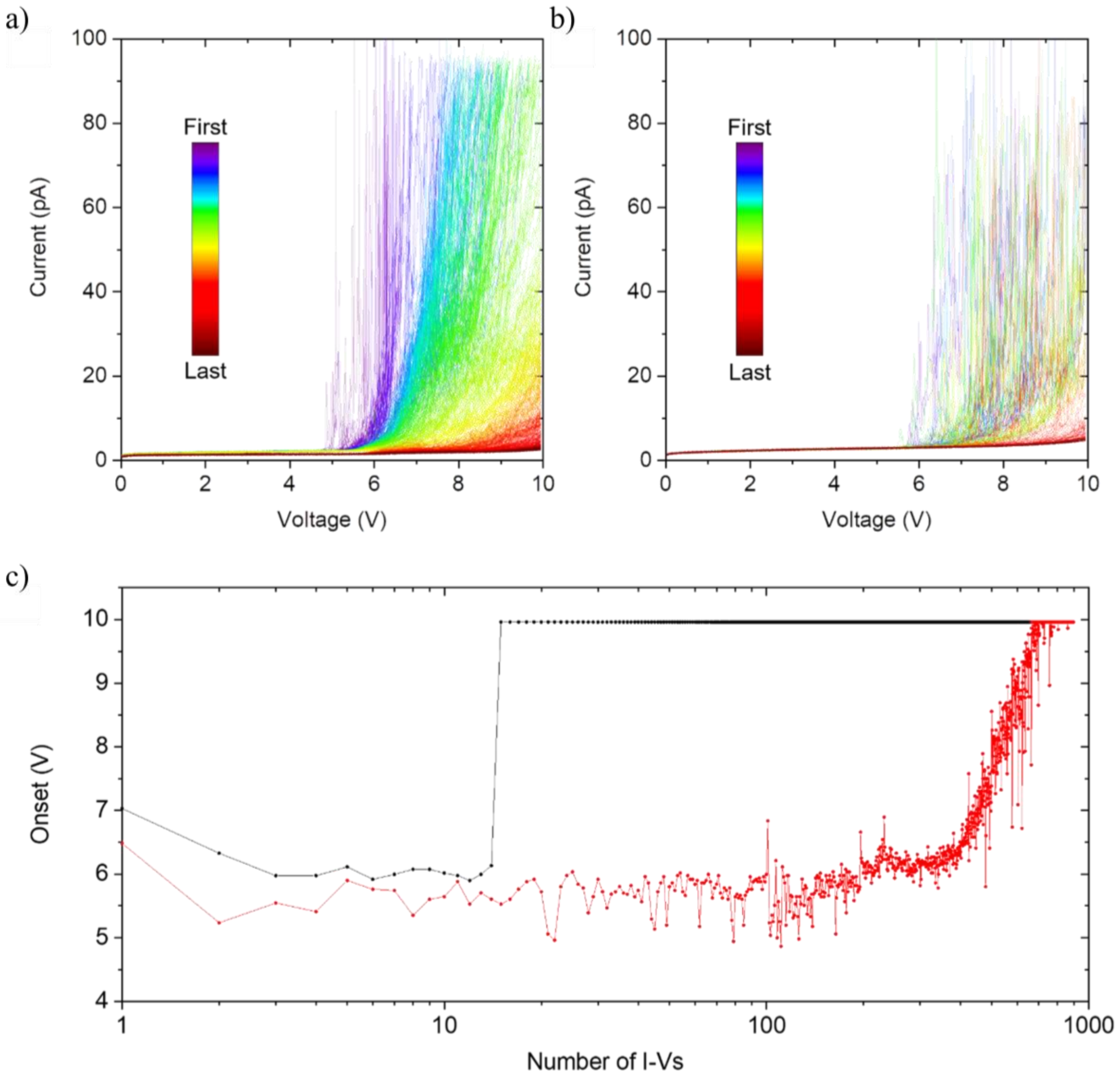

Figure 34: Consecutive current-limited RVS on SiO_2 using the ContV-Pt and the SCM-PIT-V2 probes from the measurements in Figure 33. a) With the ContV-Pt, an additional 490 I-V curves were successfully recorded. b) With the SCM-PIT-V2, 138 more I-V curves were obtained. A probe is considered non-conductive if it fails to exceed a current threshold of 10 pA in ten consecutive I-V curves, despite a 10 V sample bias. c) Onset potentials were extracted at 3 pA for the ContV-Pt, both with and without current limitation. The black dashed curve shows onset potentials from Figure 31 d (without current limitation), with a sharp transition at I-V No. 14 marking the loss of tip conductivity. The red dotted curve combines onset potentials from Figure 33 d and Figure 34 a (with current limitation). A similar analysis for the SCM-PIT-V2 was not possible, as the current dropped to the noise level after reaching 100 pA in the first I-V, followed by random shifts in V_{on} from 2 to 5.7 V in the subsequent five I-Vs. Adapted from [14], copyright American Chemical Society, 2023.

An in-depth analysis was conducted to understand the trigger's working mechanism. For this purpose, an I-V curve was recorded from 0 V to 6 V and back to 0 V (with the sample grounded), using a new RMN-25Pt300b on a 3.4 nm thick SiO_2/n^{++} Si sample. The following settings were used: A deflection setpoint of 0.2 V, a ramp frequency of 0.1 Hz, a current sensitivity of 20 pA/V (current saturation around 200 pA), and a current limitation of 100 pA. The currents flowing across the tip/sample junction were analyzed using the standard Nanoscope system, the HSDC system, and an oscilloscope (refer to Figure 32 b and Figure 35 d). In the standard configuration, a single sweep (the forward sweep from 0 V to 6 V) comprises 512 data points, corresponding to voltage steps of 9.76 mV. In this specific case, the last current value before exceeding the threshold was 7.56 pA at 5.81 V and 4.840936 s. At the subsequent voltage step, the current reached 109.33 pA, thereby surpassing the threshold and stopping the forward sweep at 498 data points (see Figure 35 a). The backward sweep, which would typically run from 6 V to 0 V, instead starts from the voltage where the forward sweep stopped. It is important to note that there is no current limitation during the backward sweep. Since stress is a function of both voltage and time, much higher currents (up to the saturation level) are observed during this phase. Nonetheless, the actual current passing through the tip/sample junction could be significantly greater.

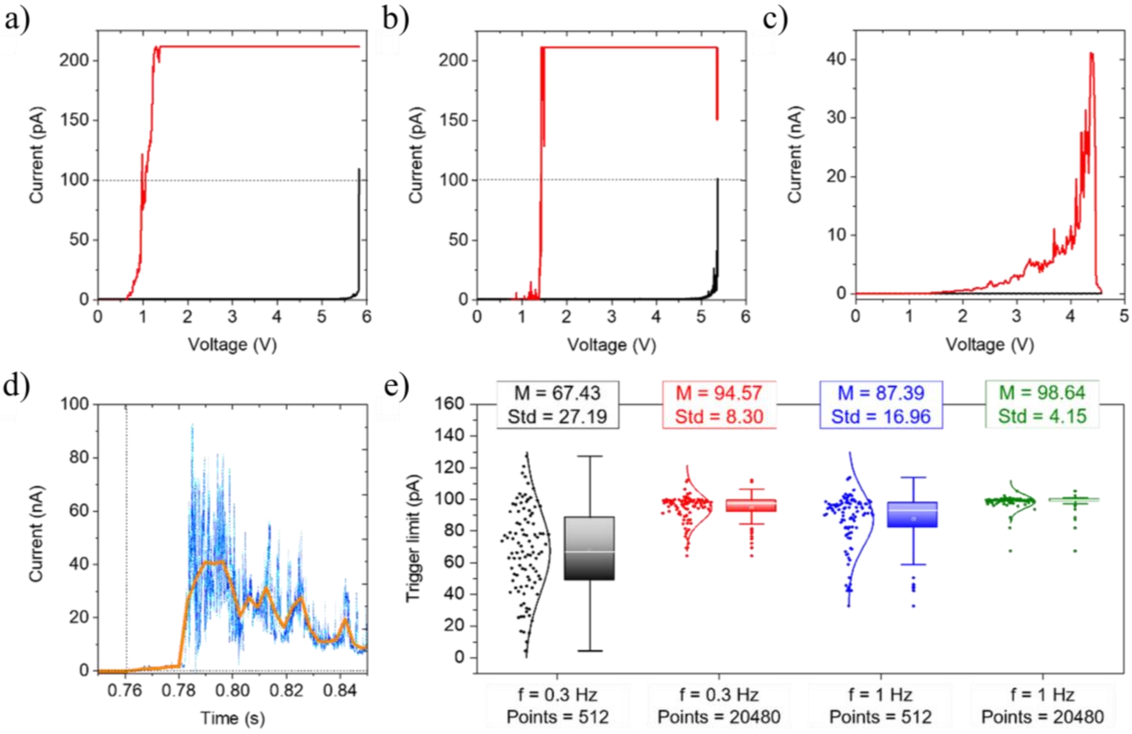

Figure 35: Trigger mechanism analysis on SiO_2: a)-c) Black solid curves represent the forward sweep, red curves the backward sweep, and black dashed horizontal lines indicate the trigger threshold. a) An exemplary I-V curve with 512 data points, a trigger threshold of 100 pA, and a current sensitivity of 20 pA/V. b) An I-V curve with 20480 data points, a trigger threshold of 100 pA, and a current sensitivity of 20 pA/V. c) An I-V curve with 512 data points, a trigger threshold of 100 pA, and a current sensitivity of 100 nA/V. d) I-T graph (solid orange line) for c), including overlayed results from the HSDC (cyan dashed line) and the Oscilloscope (blue dotted line). The black dashed horizontal line

marks the trigger threshold, while the black vertical dashed line indicates the end of the forward sweep. e) Analysis of trigger precision under various conditions. The last current value before the trigger threshold halted the voltage sweep was extracted from I-Vs in Figure 37. M denotes the mean current limit value and Std the standard deviation. Adapted from [14], copyright American Chemical Society, 2023.

To assess the impact of the sampling rate on the standard Nanoscope capture, the experiment was repeated at a different location using the system's maximum sampling rate. In this setting, each sweep comprises 20480 data points, corresponding to voltage increments of 293 µV. In this particular case, the last current value recorded before exceeding the threshold was 64.63 pA at 5.352703 V and 4.385689 s. The subsequent current measurement reached 101.43 pA, surpassing the threshold. As a result, the forward sweep halted at 18274 data points, spanning from 0 V to 5.352996 V (refer to Figure 35 b). This increased sampling rate, with an overshoot of just 1.43 pA, proved more precise compared to the standard rate, which had a 9.33 pA overshoot with 512 data points. The experiment was replicated at a different location using the standard configuration: 512 data points, a ramp frequency of 0.1 Hz, the system's lowest current sensitivity of 100 nA/V, and a trigger threshold of 100 pA (see Figure 35 c). This configuration is advantageous for detecting the actual current flowing through the tip/sample junction due to the higher saturation level. The current recorded in this setup was 41.17 nA. However, it's important to note that the lower sampling rate of the standard Nanoscope capture might not accurately capture the maximum currents, as brief current spikes could be missed. Additional measurements using the HSDC and oscilloscope revealed that the currents actually reached 92.25 nA and 89.41 nA, respectively, as depicted in Figure 35 d. Therefore, a possible enhancement for this C-AFM current-limitation system could be to enable the execution of the forward RVS without the necessity of conducting the backward sweep (from V_{STOP} to 0 V). To gain insights into the impact of current overshoot during the backward ramp, 10 current-limited I-V measurements (ranging from 0 V to V_{STOP} and back to 0 V) were conducted. These tests used a new RMN25-Pt300b tip on the SiO_2 sample, a ramp frequency of 0.3 Hz, a current sensitivity of 200 pA/V, and a deflection setpoint of 0.2 V. Various current limitation levels were applied, including 1.5, 6.5, 16, 45, 100, and 200 pA (refer to Figure 36). By comparing both, forward and backward I-V curves, it was observed that no degradation occurred in the backward curves only at the 1.5 pA current limitation. This was the sole condition under which the forward and backward curves nearly overlapped.

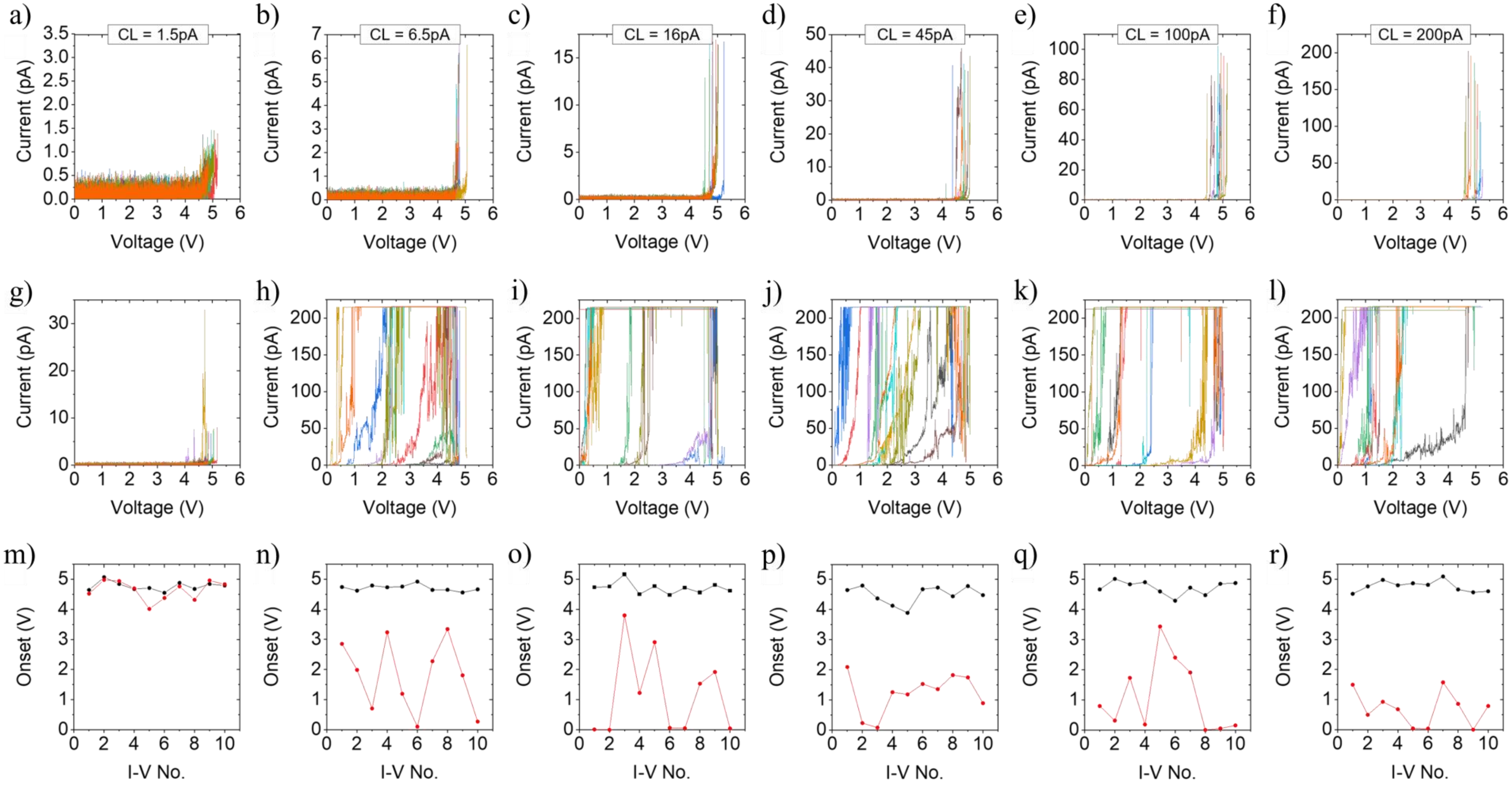

Figure 36: RVS on SiO2 with varied trigger thresholds: a)-f) Forward sweeps (from 0 V to V_{STOP}) with designated current thresholds. g)-l) Corresponding backward sweeps (from V_{STOP} to 0 V). m)-r) Onset potentials extracted at 1 pA for both forward (black dots) and backward (red dots) sweeps. Adapted from [14], copyright American Chemical Society, 2023.

To enhance the precision of the current-limitation system, experiments were conducted with varying ramp frequencies (0.3 and 1 Hz) and sampling rates (512 and 20480 data points).

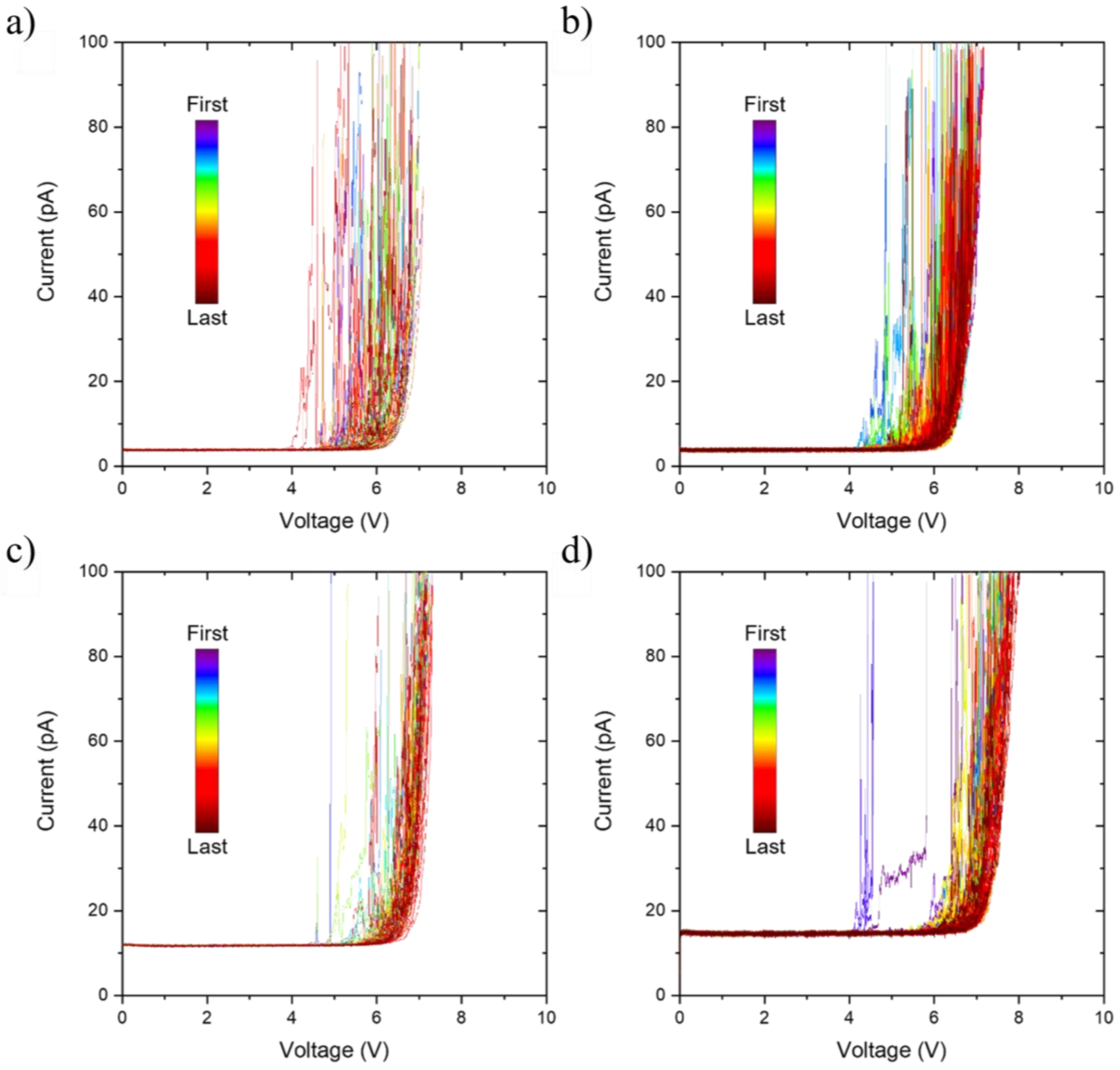

Figure 37: Current-limited RVS on SiO_2. This experiment involved recording 100 I-V curves at various locations under different settings. Displacement current compensation was omitted to prevent distorting the trigger results. Displacement currents, being linearly dependent on voltage change rate, were more pronounced in measurements with higher ramp frequencies (refer to c) and d)). Measurement specifics: a) 0.3 Hz ramp frequency with 512 data points. b) 0.3 Hz ramp frequency with 20480 data points. c) 1 Hz ramp frequency with 512 data points. d) 1 Hz ramp frequency with 20480 data points. Notably, no increasing trend in voltages was observed with the rising number of I-Vs across any of the measurement conditions. Adapted from [14], copyright American Chemical Society, 2023.

These experiments involved 100 I-V curves at different locations. The latest current value of the forward sweep from each individual I-V was extracted (as detailed in Figure 37 a-

d) and presented in Figure 35 e. The findings indicate that a higher sampling rate markedly improves the accuracy of the current-limitation system. Additionally, the data reveal that at a constant sampling rate, a higher ramp frequency also enhances the system's precision. This might seem counterintuitive, yet it could be attributed to the reduced stress imposed by higher-frequency RVS [242], which likely decreases the slope of the I-V curves. Consequently, this makes it easier to halt the curves near the desired current threshold.

Finally, 2 µm × 2 µm current maps were captured on the CVD-grown 3.3 nm multilayer h-BN/Cu sample. A new RMN-25Pt300b probe was utilized for these measurements. The current maps were generated under two distinct conditions: With a current limitation of 100 pA, using the Closed Loop feature of the Nanoscope software, and without any current limitation. Figure 38 a-b display the first and second topographic maps of the same area, recorded without current limitation. These images exhibit a good match, indicating no lateral drift. However, compared to the sharper topography in Figure 30 b-c, the images in Figure 38 a-d appear slightly blurred. This is due to the difference in R_{TIP}: whereas an ultra-sharp ScanAsyst-Air probe with a nominal R_{TIP} of 2 nm was used in Figure 30 b-c, the solid Pt probe used here had a nominal R_{TIP} of less than 20 nm. Figure 38 e-f feature the corresponding current maps. The first scan (Figure 38 e) uncovers multiple current spots, likely associated with native defects in the CVD h-BN [243]. It is important to acknowledge the possibility of introducing additional defects during the scanning process with a constant applied voltage. The second scan (Figure 38 f) reveals two key observations: i) The size of the current spots identified in the first scan increased significantly, and ii) a considerable number of new defects emerged. The experiment was replicated at a different location on the sample, this time with the current limitation activated. Figure 38 c-d present the topographic maps from the first and second scans, respectively, showing a notable match between the two. The current map from the first scan (Figure 38 g) demonstrates that the area with high current spots is smaller compared to the scan conducted without current limitation (Figure 38 e). This suggests that current limitation may reduce the incidence of newly introduced defects. It also implies that the larger defects could be inherent to the h-BN stack's synthesis, rather than being induced by the C-AFM tip.

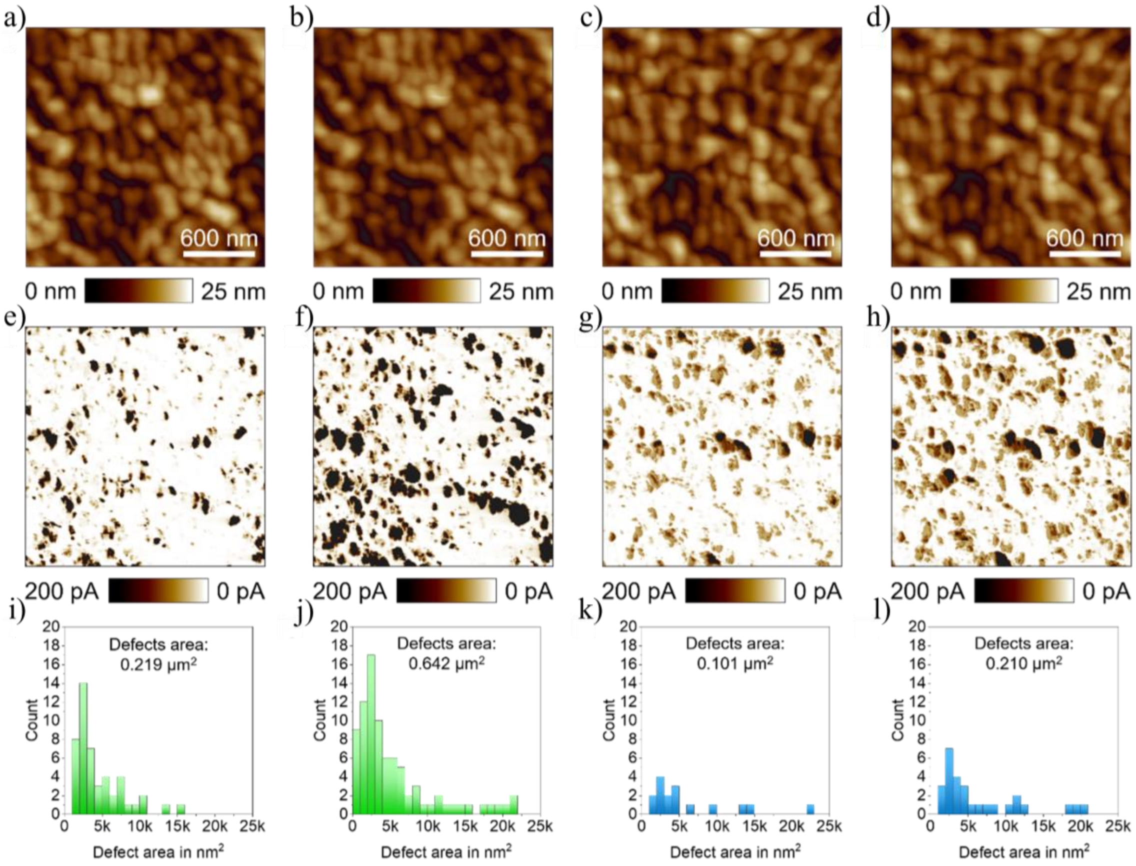

Figure 38: Current maps on CVD-grown 3.3 nm multilayer h-BN on Cu, with and without current limitation. a) First topography scan at location 1, no current limitation. e) Related current map. i) Corresponding defect histogram. b) Second topography scan at location 1, no current limitation. f) Related current map. j) Corresponding defect histogram. c) First topography scan at location 2, with current limitation. g) Related current map. k) Corresponding defect histogram. d) Second topography scan at location 2, with current limitation. h) Related current map. l) Corresponding defect histogram. Details about the size of each spot are available in Table 1. Adapted from [14], copyright American Chemical Society, 2023.

This hypothesis is further supported by the fact that at these larger defects, currents reached 100 pA at very low voltages (as shown in Figure 39). During the second scan, while there was an increase in the defect area (see Figure 38 k-l), this increase was significantly less pronounced than in the scans conducted without current limitation (compare with Figure 38 i-j).

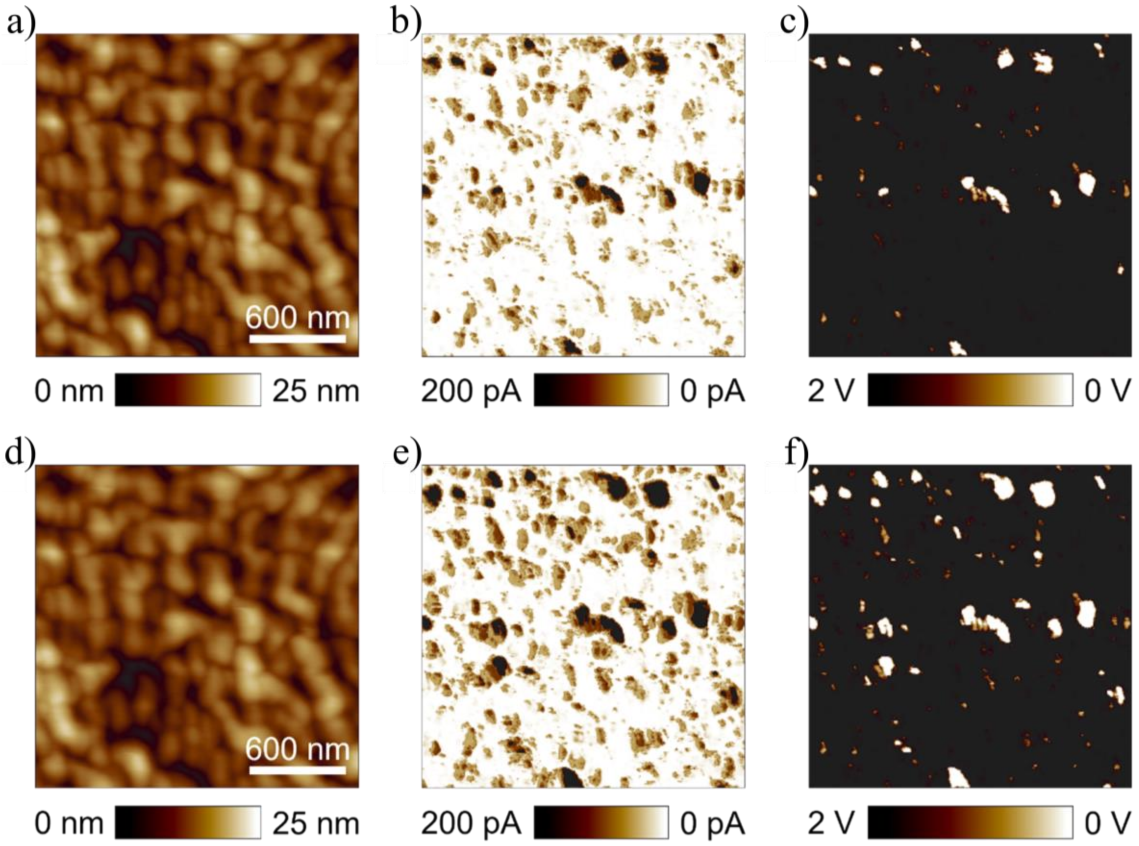

Figure 39: Current maps on CVD-grown 3.3 nm multilayer h-BN on Cu, using current limitation in closed loop configuration (100 pA limit). a) First topographic map scan at location 2 with current limitation. b) Related current map. c) Corresponding voltage map. d) Second topographic map scan at location 2 with current limitation. e) Related current map. f) Corresponding voltage map. Note: In highly conductive areas, the closed-loop configuration struggles to effectively limit currents, as the trigger threshold is often already surpassed at low voltages. Adapted from [14], copyright American Chemical Society, 2023.

The current differences were quantified by analyzing the number and size of conductive spots in the four current scans (refer to Figure 40). This analysis was performed using the Particle Analysis function of the Nanoscope Analysis software (Version 3.0, Bruker, Massachusetts, USA), with the detection threshold set at 100 pA. Each defect in the first scans, both with and without current limitation, was assigned a unique identifier. These identifiers were then mapped onto the results of the second scans to track defects present in the initial scans. In cases where distinct defects from the first scans merged in the second scans, the total combined area was attributed to the initially identified defect, and the size of the subsequent defect was recorded as zero. Remaining defects were then cataloged. A comprehensive defect-by-defect breakdown is available in Table 1.

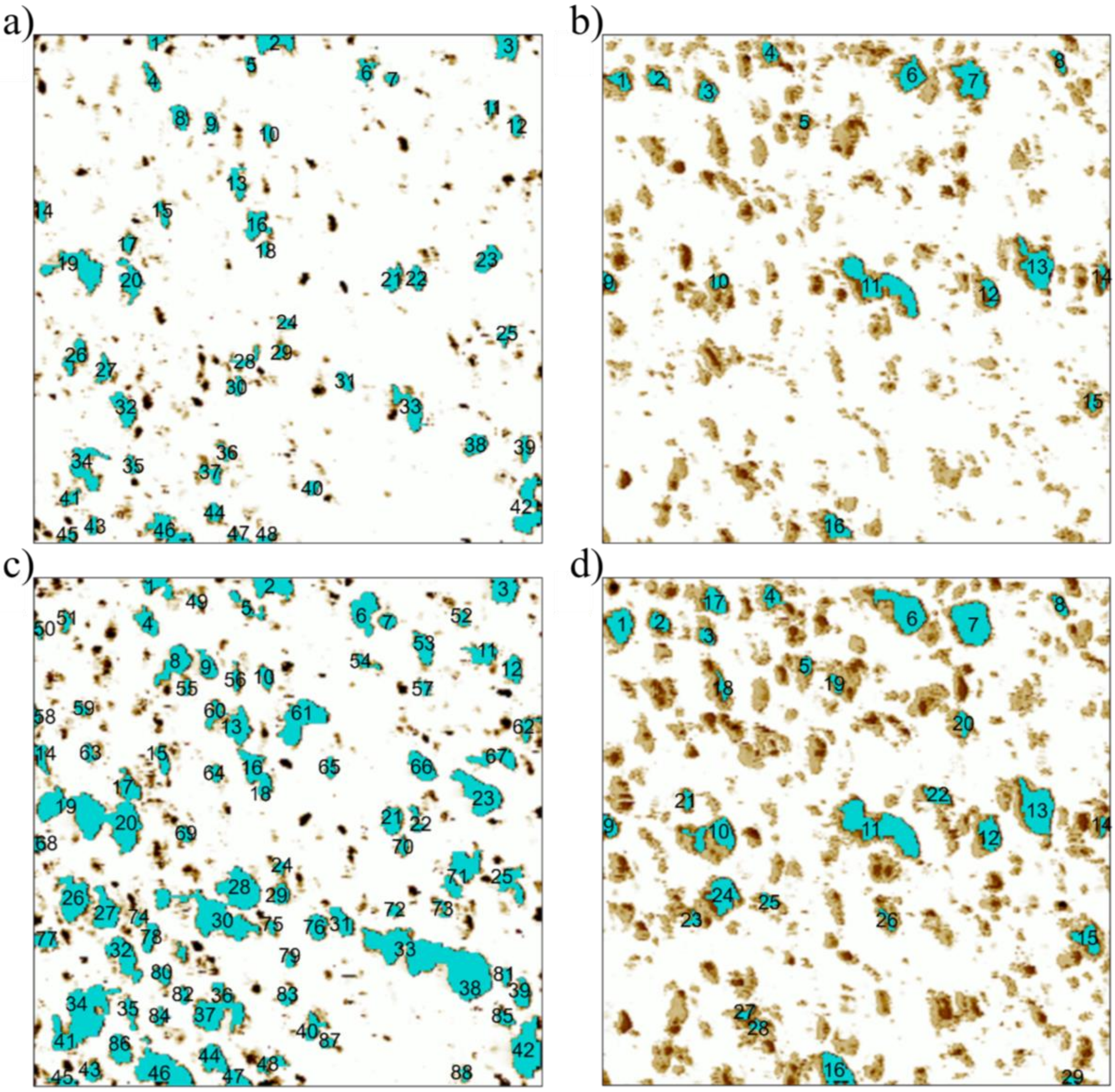

Figure 40: Nanoscope particle analysis results (100 pA detection threshold). a) Defects identified in the first scan at location 1 without current limitation. b) Defects detected in the first scan at location 2 with current limitation. c) Defects identified in the second scan at location 1 without current limitation. d) Defects detected in the second scan at location 2 with current limitation. Adapted from [14], copyright American Chemical Society, 2023.

Histogram representations in Figure 38 i-l clearly show that implementing current limitation not only reduced the emergence of new defects but also curtailed the enlargement of existing ones (see comparisons between Figure 38 i and Figure 38 j, and Figure 38 k and Figure 38 l).

Table 1: Detailed size comparison of the current spot shown in Figure 40. Adapted from [14], copyright American Chemical Society, 2023.

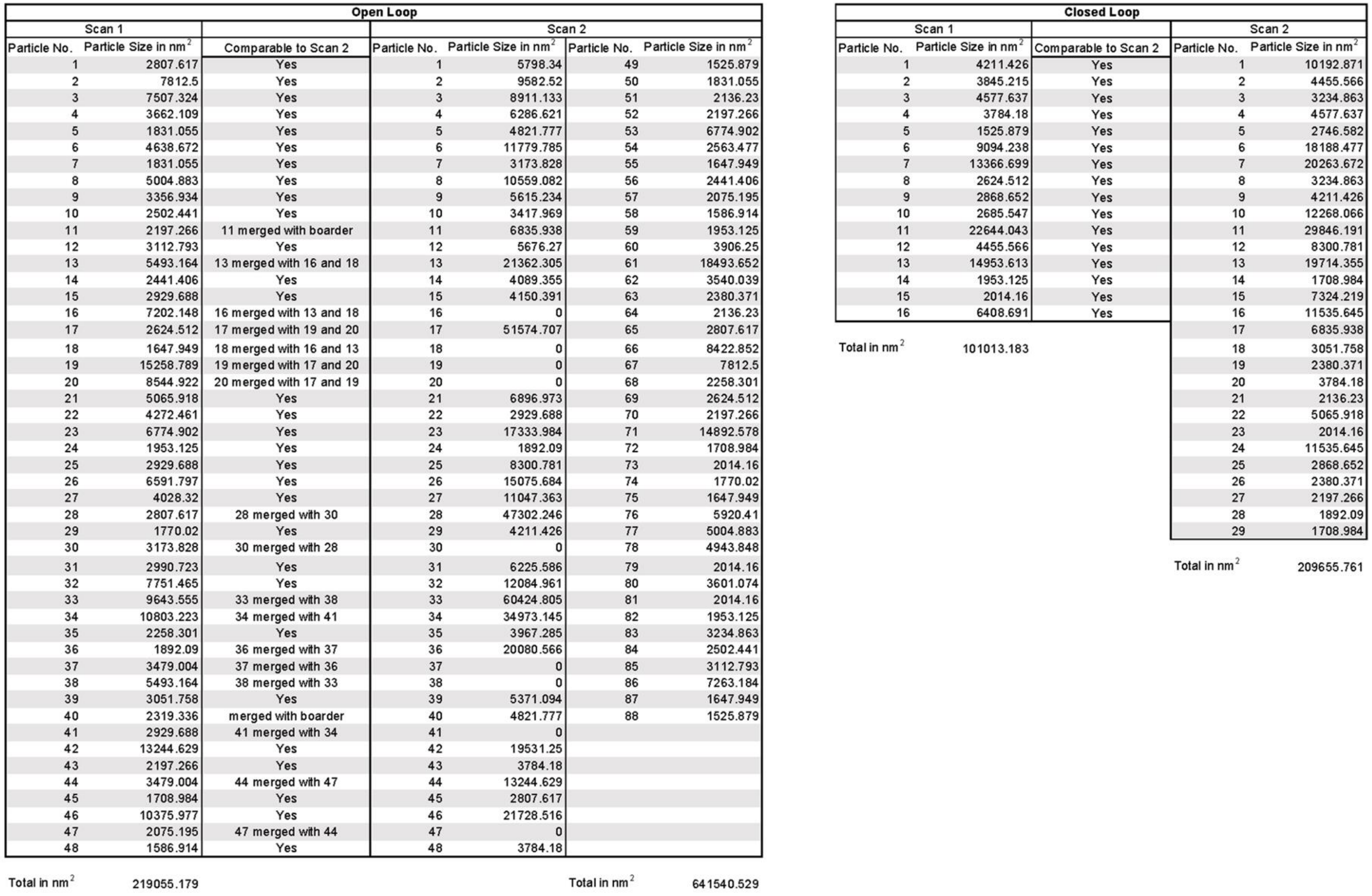

Open Loop						
Scan 1			Scan 2			
Particle No.	Particle Size in nm^2	Comparable to Scan 2	Particle No.	Particle Size in nm^2	Particle No.	Particle Size in nm^2
1	2807.617	Yes	1	5798.34	49	1525.879
2	7812.5	Yes	2	9582.52	50	1831.055
3	7507.324	Yes	3	8911.133	51	2136.23
4	3662.109	Yes	4	6286.621	52	2197.266
5	1831.055	Yes	5	4821.777	53	6774.902
6	4638.672	Yes	6	11779.785	54	2563.477
7	1831.055	Yes	7	3173.828	55	1647.949
8	5004.883	Yes	8	10559.082	56	2441.406
9	3356.934	Yes	9	5615.234	57	2075.195
10	2502.441	Yes	10	3417.969	58	1586.914
11	2197.266	11 merged with boarder	11	6835.938	59	1953.125
12	3112.793	Yes	12	5676.27	60	3906.25
13	5493.164	13 merged with 16 and 18	13	21362.305	61	18493.652
14	2441.406	Yes	14	4089.355	62	3540.039
15	2929.688	Yes	15	4150.391	63	2380.371
16	7202.148	16 merged with 13 and 18	16	0	64	2136.23
17	2624.512	17 merged with 19 and 20	17	51574.707	65	2807.617
18	1647.949	18 merged with 16 and 13	18	0	66	8422.852
19	15258.789	19 merged with 17 and 20	19	0	67	7812.5
20	8544.922	20 merged with 17 and 19	20	0	68	2258.301
21	5065.918	Yes	21	6896.973	69	2624.512
22	4272.461	Yes	22	2929.688	70	2197.266
23	6774.902	Yes	23	17333.984	71	14892.578
24	1953.125	Yes	24	1892.09	72	1708.984
25	2929.688	Yes	25	8300.781	73	2014.16
26	6591.797	Yes	26	15075.684	74	1770.02
27	4028.32	Yes	27	11047.363	75	1647.949
28	2807.617	28 merged with 30	28	47302.246	76	5920.41
29	1770.02	Yes	29	4211.426	77	5004.883
30	3173.828	30 merged with 28	30	0	78	4943.848
31	2990.723	Yes	31	6225.586	79	2014.16
32	7751.465	Yes	32	12084.961	80	3601.074
33	9643.555	33 merged with 38	33	60424.805	81	2014.16
34	10803.223	34 merged with 41	34	34973.145	82	1953.125
35	2258.301	Yes	35	3967.285	83	3234.863
36	1892.09	36 merged with 37	36	20080.566	84	2502.441
37	3479.004	37 merged with 36	37	0	85	3112.793
38	5493.164	38 merged with 33	38	0	86	7263.184
39	3051.758	Yes	39	5371.094	87	1647.949
40	2319.336	merged with boarder	40	4821.777	88	1525.879
41	2929.688	41 merged with 34	41	0		
42	13244.629	Yes	42	19531.25		
43	2197.266	Yes	43	3784.18		
44	3479.004	44 merged with 47	44	13244.629		
45	1708.984	Yes	45	2807.617		
46	10375.977	Yes	46	21728.516		
47	2075.195	47 merged with 44	47	0		
48	1586.914	Yes	48	3784.18		
Total in nm^2	219055.179				Total in nm^2	641540.529

Closed Loop				
Scan 1			Scan 2	
Particle No.	Particle Size in nm^2	Comparable to Scan 2	Particle No.	Particle Size in nm^2
1	4211.426	Yes	1	10192.871
2	3845.215	Yes	2	4455.566
3	4577.637	Yes	3	3234.863
4	3784.18	Yes	4	4577.637
5	1525.879	Yes	5	2746.582
6	9094.238	Yes	6	18188.477
7	13366.699	Yes	7	20263.672
8	2624.512	Yes	8	3234.863
9	2868.652	Yes	9	4211.426
10	2685.547	Yes	10	12268.066
11	22644.043	Yes	11	29846.191
12	4455.566	Yes	12	8300.781
13	14953.613	Yes	13	19714.355
14	1953.125	Yes	14	1708.984
15	2014.16	Yes	15	7324.219
16	6408.691	Yes	16	11535.645
			17	6835.938
Total in nm^2	101013.183		18	3051.758
			19	2380.371
			20	3784.18
			21	2136.23
			22	5065.918
			23	2014.16
			24	11535.645
			25	2868.652
			26	2380.371
			27	2197.266
			28	1892.09
			29	1708.984
			Total in nm^2	209655.761

It may be concluded that the integration of a current limitation system for C-AFM application is immensely advantageous. Utilizing this system during ramped voltage stresses and current mapping significantly extends the lifespan of both the tip and the sample, thereby boosting the reliability of the obtained data. Though this study was conducted on the current limiting system used in the Dimension Icon AFM by Bruker, the advantages of this method are applicable to any current-limited C-AFM system. The findings affirm that this system effectively maintains the conductivity and integrity of C-AFM tips during leakage current and dielectric breakdown characterization in ultra-thin dielectrics (3.4 nm SiO_2 on n^{++} Si), increasing their lifetime by approximately a factor of 50. Additionally, the precision of this system during ramped voltage stresses can be improved through higher sampling rates and ramp frequencies. While conducting lateral scans on h-BN on Cu samples, the system significantly reduces the formation of new defects, as compared to standard current maps obtained in an open-loop configuration, although it does not completely eliminate them. The current limitation feature is user-friendly and does not require prior knowledge of the sample's resistance or additional external wiring. Its simplicity and effectiveness make it a valuable tool in enhancing the reliability of C-AFM studies across various fields, while also reducing costs due to prolonged probe lifetimes. The results of this chapter have been published in [14].

4.2.2 Hardware-Based Current Limitation

Chapter 4.1.1 addresses common challenges encountered with standard metal-coated C-AFM probes. A key issue are the high current densities due to the small contact area, potentially leading to the melting of the tip’s conductive varnish. This can result in partial or complete loss of tip conductivity. While a total loss is easily identifiable, partial loss presents more subtly as increased tip resistance and reduced current flow, complicating detection and potentially leading to inaccurate measurements, such as erroneous oxide thickness calculations. An alternative might be the use of more robust probes, such as boron-doped diamond-coated or solid metal probes, as discussed in Chapter 4.1.2. However, these come with limitations. They are more expensive and offer a limited range of spring constants, restricting their use to specific sample types only. Diamond-coated probes [177] typically have a larger tip radius compared to metal-coated counterparts [16], leading to decreased lateral resolution. Additionally, the persistence of high current densities means that current-induced damage to the sample remains a concern, making the analysis of delicate materials like semiconductive polymer blends used in LEDs [244], or sensitive organic samples [245], challenging. To enable the analysis of delicate samples, limiting the resultant currents is an effective strategy. A common method involves connecting a resistor in series with the tip [237-239], which effectively caps the currents. However, this approach requires prior knowledge of the sample's resistance to select an appropriate resistor value. This information is not always readily available. Additionally, the wiring process can be cumbersome, particularly as different samples may require distinct resistors. This is further complicated by the C-AFM model being used, and the potential introduction of additional parasitic capacitance due to the added components. Some C-AFM systems offer an integrated software-based current limitation algorithm, commonly known as trigger. This algorithm continuously compares the actual current value against a predetermined current threshold. When this threshold is reached, the ongoing voltage sweep is halted at a specific voltage point (V_{STOP}). However, it's important to note that the system invariably executes a backward sweep to return the voltage from V_{STOP} to its origin. Electrical stress is also a function of time, and when probing highly non-linear electrical dynamics, which is a typical scenario in C-AFM experiments, there is a risk of excessive currents flowing through the tip before the electrical stress is completely removed. For instance, in the characterization of a thin dielectric film, the sample might undergo breakdown during the backward sweep. This can lead to currents far exceeding the preset threshold, which in turn might damage the tip's coating. Most C-AFM experiments utilize current-to-voltage amplifiers that may inherently limit current due to amplifier saturation. However, this limitation is governed by the amplifier's sensitivity (or gain) range and is not adjustable.

To overcome the previously introduced challenges, a new, universally applicable sample holder has been developed, featuring an integrated MOSFET transistor to effectively limit current intensity. The objectives of this sample holder contain, but are not limited to the following:

i) Extending the life time of conductive probe tips: By capping high currents flowing through the tip to a customizable value, the longevity of the probe tips is significantly increased.

ii) Enhancing experimental reliability: The degradation of tip performance due to electrical damage is minimized and frequent tip replacements are therewith avoided. This reduction in variability is particularly crucial in sensitive experiments where consistent tip quality is essential.

iii) Reducing electrical damage to samples: The sample holder effectively limits the currents that are flowing through the sample during C-AFM investigations. This feature is especially beneficial for insulating layers with strongly non-linear electrical characteristics under voltage stress, such as dielectric breakdown, which often exhibit large current spikes.

iv) Advanced scanning techniques: The ability to perform current-limited and constant current scans on novel thin films allows for precise control over voltage and current-dependent effects, including hydrogenation, ferroelectricity, and ion migration.

The newly designed sample holder consists of a standard printed circuit board (PCB), which is specifically designed to connect the sample to the drain of a MOSFET. A schematic of the sample holder is provided in Figure 41. The key features of the PCB comprise:

i) A top circular connection region (1) for linking the sample under test (2) to the MOSFET's DRAIN terminal (3).

ii) A designated footprint (4) for the soldering of a SOT-23 packaged MOSFET (3), with the model being customizable based on experimental needs.

iii) Copper wires connecting the GATE and SOURCE terminals of the MOSFET (3) to externally accessible contacts (5-6).

iv) Through-PCB via connections enabling the SOURCE terminal of the MOSFET (3) to connect to the PCB's bottom side and to the bottom circular connection region (7).

Specifically, both the top (1) and bottom (7) circular connection regions are coated with a conductive paste (8) to ensure low-resistance contact with the top iron sample plate (9) (optional) and the bottom iron sample plate (10). The material of these plates is chosen based on its electrical conductivity, with iron being preferred for the bottom plate to facilitate magnetic attachment to the C-AFM system sample chuck (11). Alternative fixation methods, such as vacuum, can also be employed. The sample under test is placed, preferably with a conductive adhesive (carbon tape, or silver paint), on either the top circular connection region (1) or the top iron sample plate (9).

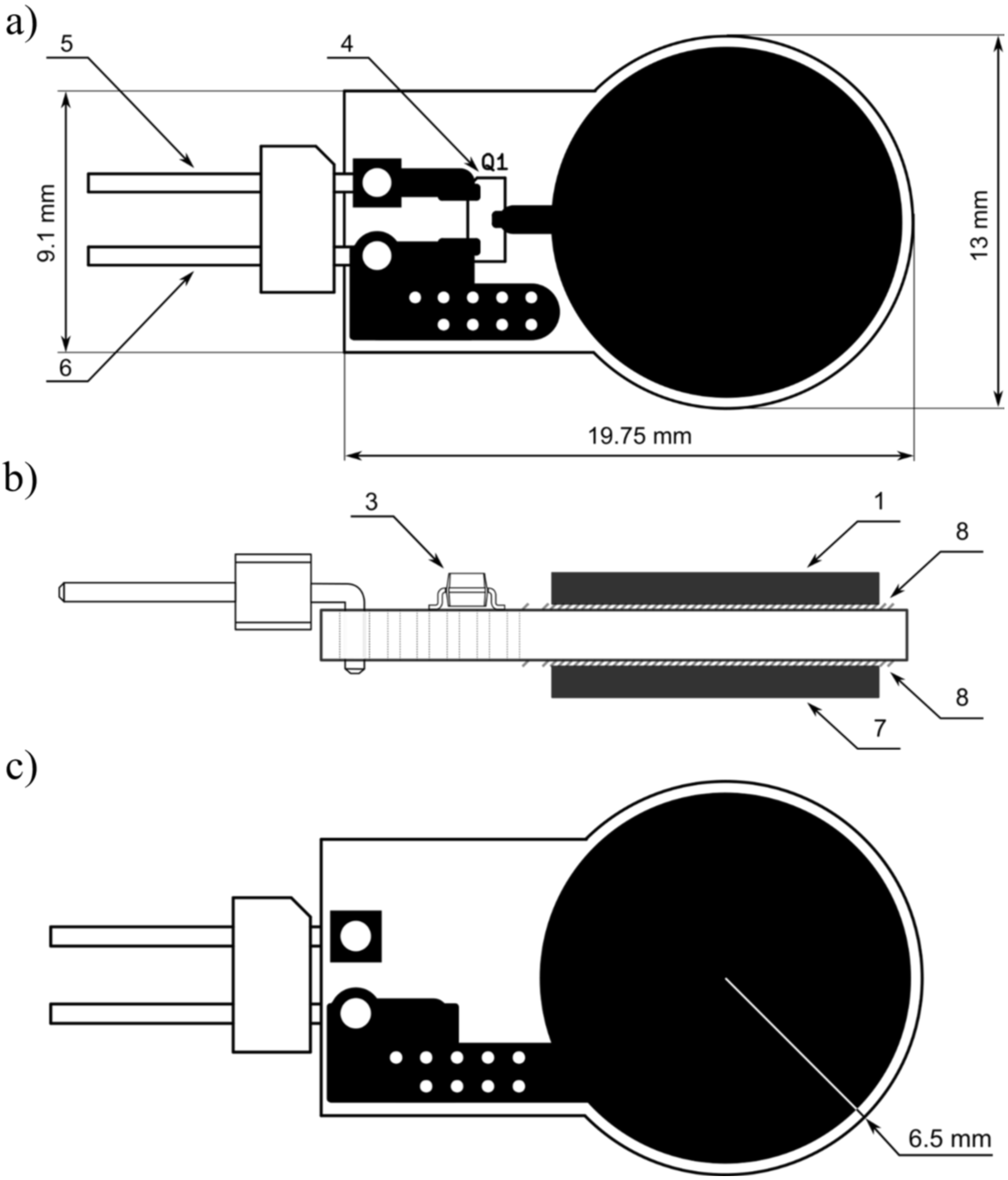

Figure 41: MOSFET sample holder schematic. a) Top view. b) Side view. c) Bottom view.

For operation, the GATE (5) and SOURCE (6) are connected to an external floating voltage source (12) that supplies the bias voltage to the MOSFET, thus enabling current limitation according to the transistor schematic in Figure 42. In this design a BSS138L n-channel logic level enhancement mode field effect transistor was chosen for its low drain source resistance in the ON state ($R_{DS(ON)}$), minimal leakage currents in the OFF state, low capacitance, and rapid switching speeds [246]. However, this transistor can be interchanged with various models to accommodate specific experimental requirements. The sample holder is designed to be compatible with all MOSFETs that utilize a SOT-23 housing, providing flexibility for diverse research applications.

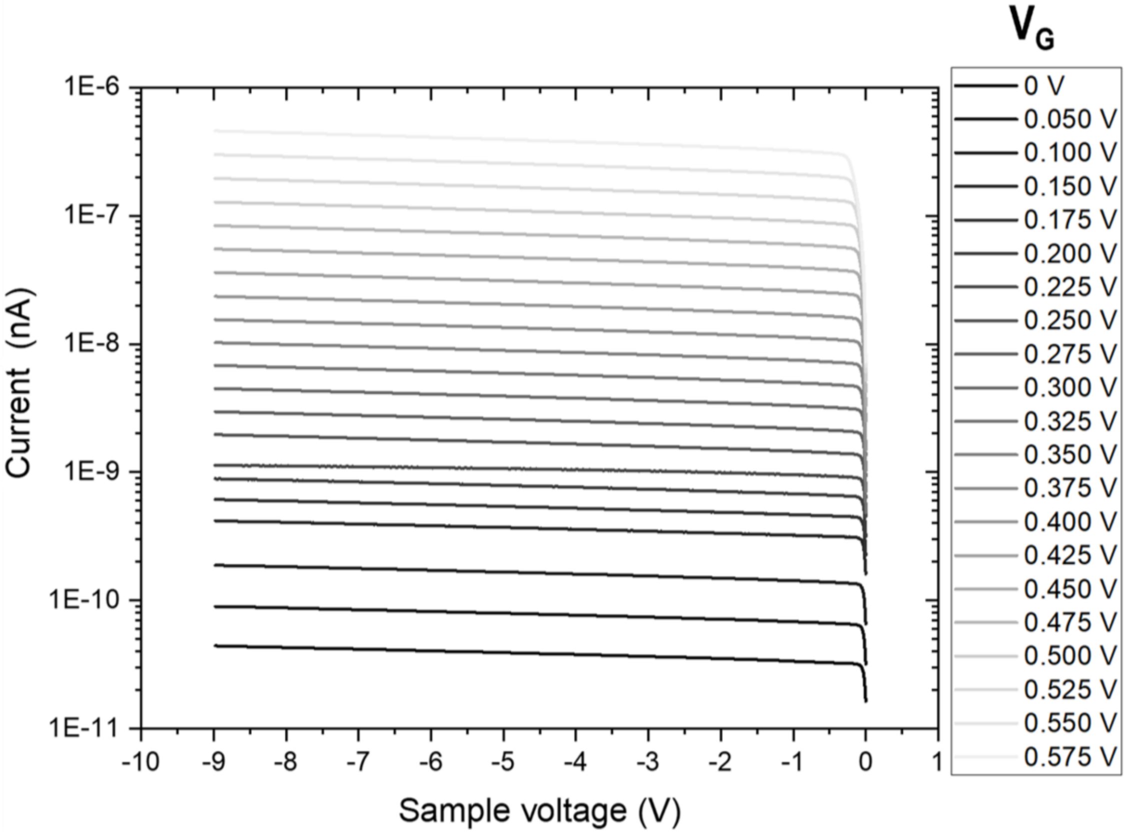

Figure 42: Exemplary RVS on a conductive sample using the current limiting sample holder, and a new RMN-25Pt300b probe on a Bruker Dimension ICON.

These connections can be established using a straight connection pole or by directly soldering a wire pair to a chosen connector type (clamps, banana jack, or coaxial connector). The limiting current value is determined by the voltage difference applied between the GATE and SOURCE of the selected MOSFET. The corresponding circuit diagram is depicted in Figure 43. This method facilitates current limitation without requiring prior knowledge of the sample's resistance. It also supports the analysis of various samples with different electrical properties simply by adjusting the gate voltage, eliminating the need for complex hardware alterations typical of series resistor-based methods. Unlike the Trigger algorithm, this design effectively restricts current in both directions of the voltage sweep and under constant voltages in area scans. This significantly diminishes the risk of damage to both the sample and the conductive coating of the tip.

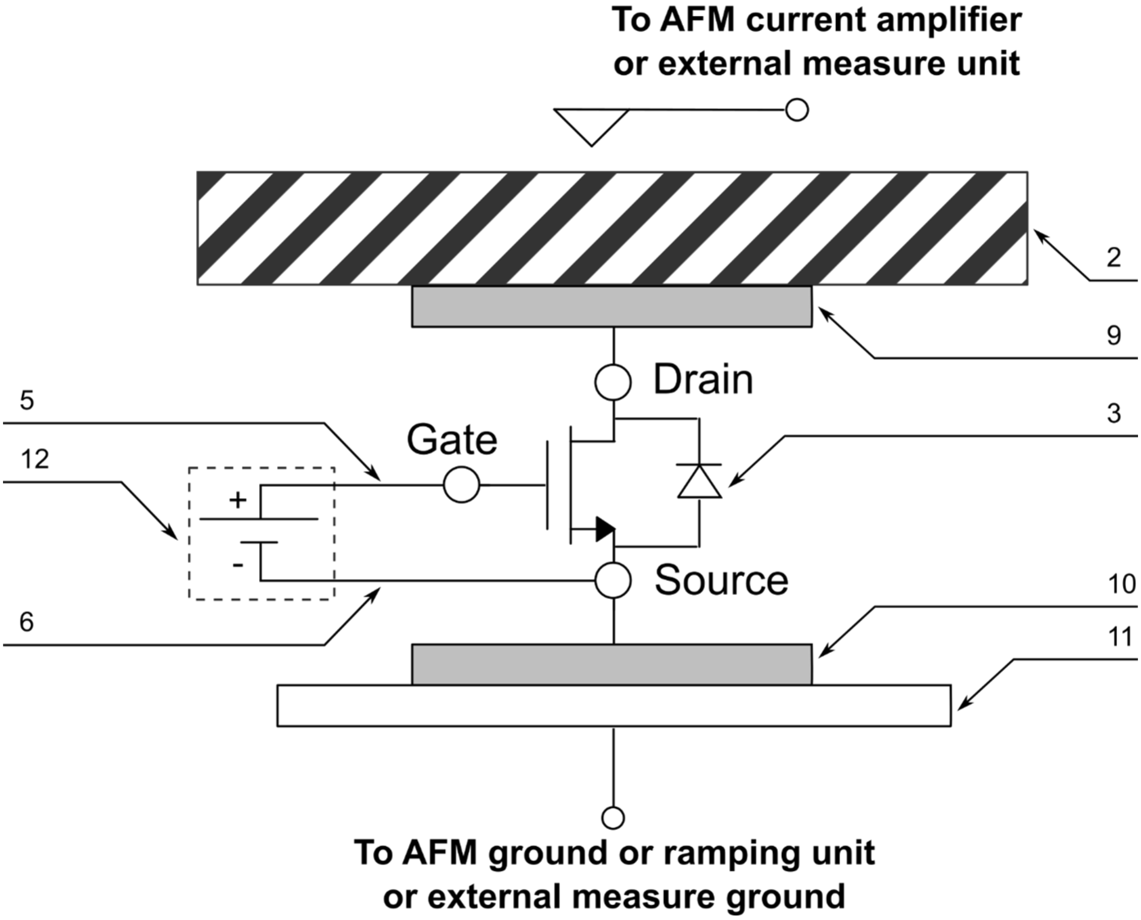

Figure 43: Schematic connection diagram of the current limiting sample holder on a standard AFM setup.

Overall, this implementation results in a sample holder that integrates a transistor (3-4) and a conductive connection region (1) for the sample under test (2), along with a separate connection to the C-AFM sample chuck (7) for conducting current-limited C-AFM experiments.

To demonstrate the effective current limitation of the newly developed sample holder, several C-AFM measurements were conducted using a Bruker Dimension ICON equipped with a TUNA module. Measurement 1, as shown in Figure 44 a, was performed on a 3.4 nm SiO_2/n^{++} Si sample without the use of a trigger or the sample holder. Measurement 2, depicted in Figure 44 b, also on 3.4 nm SiO_2/n^{++} Si, was executed with the trigger function activated but without the current limiting sample holder. The third measurement, illustrated in Figure 45, was carried out on a 1.5 nm SiO_2/n^{++} Si sample, utilizing the current limiting sample holder, but without the trigger function. In Measurement 3, a thinner oxide layer was deliberately selected to facilitate the occurrence of dielectric breakdown, and therewith higher currents, more readily. In all these experiments, voltage ramps were applied from 0 V to -9 V and back to 0 V (with tips grounded to prevent anodic oxidation) at a ramp rate of 1 Hz, employing a new solid Pt RMN-25Pt300b probe ($R_{TIP,nom}$ < 20 nm, $k_{C,nom}$ = 18 N/m) for each measurement.

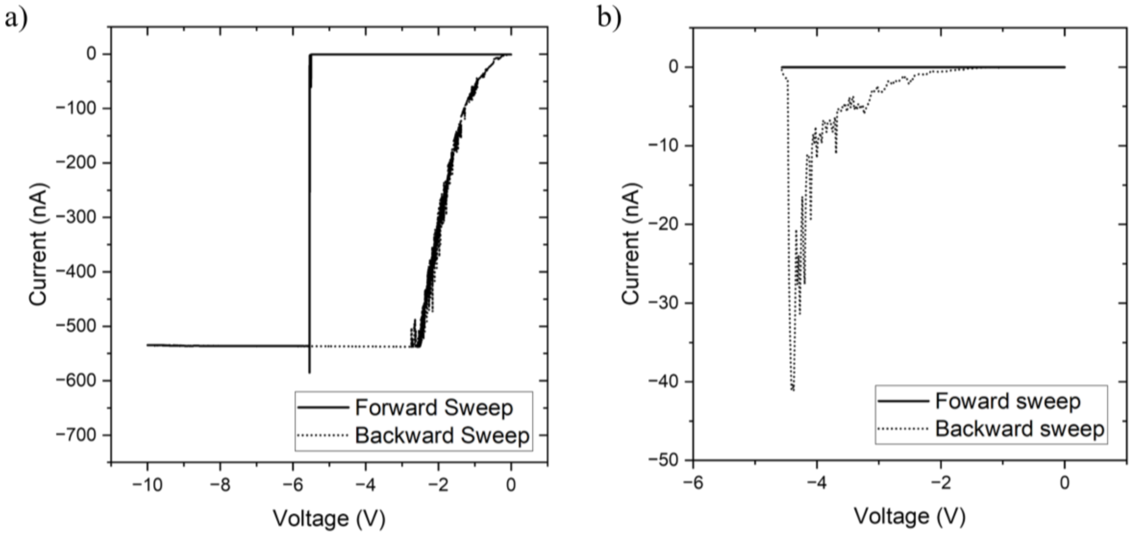

Figure 44: Exemplary RVS on 3.4 nm SiO_2/n^{++} Si. a) Without trigger and no current limiting sample holder. b) With trigger and no current limiting sample holder. The forward sweep from 0 V to -9 V is illustrated by a solid black line, the backward sweep from -9 V to 0 V by a dotted black line.

In Measurement 1 (see Figure 44 a), conducted without current limitation, a sharp increase in current was observed at around 5.5 V, reaching approximately 540 nA, which corresponds to the saturation limit of the current amplifier. It is important to note that actual currents might have been even higher. During the backward sweep, the current remained at this saturation level until around -2.5 V. For Measurement 2 (see Figure 44 b), which incorporated current limitation via the trigger function, the forward sweep was halted at around 4.5 V as the current exceeded the set trigger threshold of 100 pA. However, during the backward sweep, the current spiked to over 40 nA.

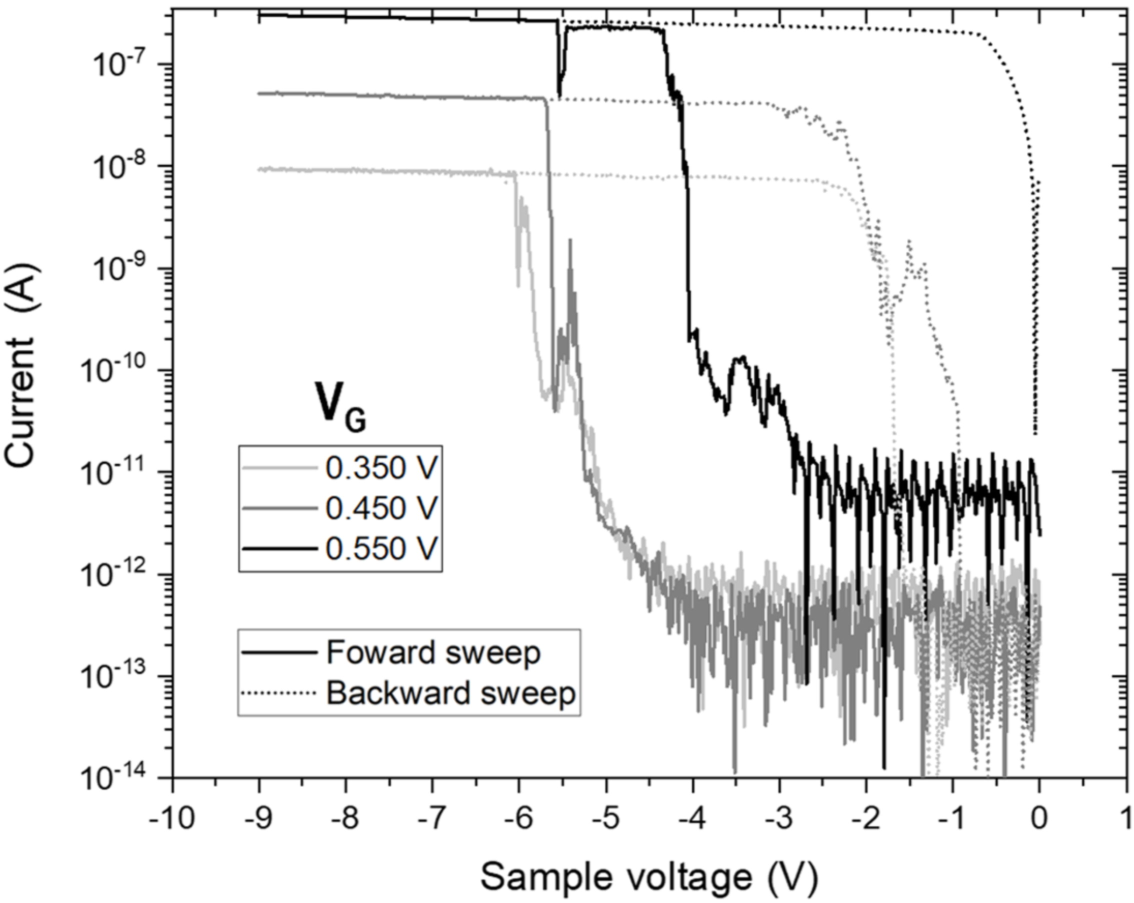

Figure 45: Exemplary RVS on 1.5 nm SiO_2/n^{++} Si using the current limiting sample holder without trigger. Three consecutive tests at different locations using varied gate voltages were conducted. The forward sweep from 0 V to -9 V is illustrated by a solid line, the backward sweep from -9 V to 0 V by a dotted line.

Measurement 3 (see Figure 45), involving current limitation through the sample holder, involved three consecutive tests at individual, random locations using varying gate voltages. In the range of -4 V to -6 V all tested locations exhibited dielectric breakdown during the forward sweep. This is obvious because of the steep rise in current across several orders of magnitude and the discrepancy with the backward sweeps, which stayed at the maximum current level until lower voltages in the range of approx. -2.5 V to -0.5 V. Without current limitation, the currents would have risen to significantly higher levels [20], potentially high enough to melt the Pt of the deployed probe. This setup however achieved effective current limitation throughout both, the full forward and backward sweeps, spanning across multiple configurable current magnitudes. The maximum currents during forward and backward sweep correlate with each other and the overall characteristics align with the transistor characteristics shown in Figure 42. This demonstrates the flawless operation of the sample holder in both sweep directions.

In summary, it may be stated that the current-limiting sample holder represents a promising advancement in C-AFM technology. Unlike the conventional trigger mechanism, this holder provides genuine current limitation in both the forward and backward sweep directions. Though, this would also be achievable by connecting resistors in series to the tip, using the sample holder does not require previous knowledge about the sample’s resistance. Additionally, using resistors often requires changing hardware for different samples, whereas with the current-limiting sample holder, a simple adjustment of the gate voltage is sufficient to adapt to various sample types. Thanks to its compatibility with standard SOT-23 housed transistors, the sample holder is highly customizable for a broad range of experiments. Moreover, it is applicable on almost all C-AFM systems.

The combination of versatility, effectiveness, and ease of use makes this current-limiting sample holder a valuable asset in the field of material analysis. It holds the potential to significantly improve the reliability of standard material analysis techniques utilized in both academic and industrial settings by effectively reducing tip and sample damage, which facilitates longer probe lifetimes. This not only enhances the quality and accuracy of C-AFM investigations but also contributes to cost reduction by minimizing the need for frequent probe replacements. Additionally, the sample holder's capability to handle current-sensitive samples broadens the scope of C-AFM applications to include a wider range of materials. This extension presents opportunities for exploring novel materials, yielding fresh perspectives and discoveries. The introduction of this sample holder represents a significant advancement, contributing to enhanced accuracy, reliability, and diversification in C-AFM applications.

5 Conclusion and Outlook

Despite C-AFM being a widely recognized and effective technique for analyzing the topography and electrical resistivity of diverse samples at the nanoscale, one of the most significant challenges in this field is ensuring the reproducibility of data. The difficulty in achieving consistent C-AFM results arises due to the large number of factors that affect the establishment and maintenance of a stable tip-sample contact. A particularly critical and difficult-to-control factor is tip degradation. This issue predominantly stems from the fine radii of the probes employed in these measurements. While these slender tip radii are vital for attaining high topographical resolution, they simultaneously increase the susceptibility of the probes to degradation. This degradation can largely be attributed to two main factors: Lateral frictions, especially since most C-AFM measurements are conducted in contact mode, and the high current densities encountered when a bias voltage is applied. With intermittent contact mode already proving effective in mitigating tip degradation due to mechanical abrasion, the focus of this thesis was to explore strategies to minimize tip degradation caused by high current densities. To address this, the extent of degradation in metal-coated probes across various C-AFM measurement scenarios should be thoroughly assessed. Furthermore, the viability of commercially available alternatives, such as solid Pt probes and software-based current limitation techniques, should be evaluated. Ultimately a robust solution capable of effectively safeguarding C-AFM probes from damage caused by high current densities should be developed. The overall objective was to enhance C-AFM reliability, thus ensuring more consistent and dependable results in nanoscale material analysis.

The dynamic degradation process of various metal-coated probe types during RVS on different ultra-thin dielectrics has been examined in Chapters 4.1.1, 4.1.2, and 4.2.1. As outlined in Chapter 4.1.1 the experimental observations indicate a two-phase degradation process for these probes. Initially the thickness of the conductive coating reduces before it melts completely. During this thinning phase, a stable intermediate state, marked by increased contact resistance, emerges occasionally. This intermediate state can be difficult to identify and may potentially lead to incorrect conclusions in material assessment. To mitigate this risk, it is recommended to initially evaluate the performance of the probe on a sample with established electrical parameters, or to verify the findings by conducting the experiment again with a second probe. In the Chapters 4.1.2 and 4.2.1, by recording sequences of RVS on ultra-thin SiO_2, a clear downward trend towards higher voltages with an increasing number of RVS was observed for Pt/It-coated ContV-Pt and SCM-PIT-V2 probes. There was noticeable variability in the number of RVS that each ContV-Pt and SCM-PIT-V2 probe could record. The degradation observed in both probe types varied, ranging from abrupt to gradual. Furthermore, it was found that some ContV-Pt probes exhibited greater durability compared to certain SCM-PIT-V2 probes, and in some cases, the reverse was true. However, no definitive trend was established that indicated a consistently superior performance of either ContV-Pt or SCM-PIT-V2 probes in terms of the number of RVS they could successfully record.

Further investigations revealed that the currents recorded during RVS using a PFTUNA probe on a $TiO_2/SiO_x/n^{++}$ Si sample were notably lower than anticipated. Computational analyses indicated that this significant decrease in current was due to the formation of a water nanogap between the C-AFM tip and the sample. This nanogap, arising due to the lower contact force associated with the low spring constant characteristic of this probe type, remained unchanged even when the maximum contact force that the equipment could exert (achieved with a Deflection Setpoint of 10 V) was applied. Likely capillary forces arising from the water meniscus at the tip-sample interface exert a repulsive force, counterbalancing the force applied by the system. To ensure accurate measurements of d_{ox} or V_{on}, it is recommended to utilize stiffer C-AFM probes for RVS on these types of samples, or to perform the measurements in a controlled environment, like under vacuum or in a dry nitrogen atmosphere.

A comprehensive statistical analysis of the performance of solid Pt probes (model RMN-25Pt300b) across various disciplines encompassing topography measurements, step height estimations, current map recordings, and RVS was performed in Chapter 4.1.2. In summary, when considering cost-effectiveness and reliability in C-AFM studies, solid Pt probes emerge as an outstanding option. Although they might provide slightly lower topographical resolution than Pt/Ir-coated probes, this minor drawback is more than compensated for by their superior endurance across multiple scans and their greatly enhanced electrical durability. These qualities establish solid Pt probes as highly valuable tools for consistent, long-term C-AFM investigations.

Chapter 4.2.1 provides a thorough exploration of both the working principle and the effectiveness of the software-based current limitation feature in the Bruker Dimension Icon. This feature is designed for easy application and does not necessitate prior knowledge of the sample's resistance. Unlike relying solely on more durable probes, this method proactively restricts the resulting currents. This enables the prolonged use of metal-coated probes (by approximately a factor of 50, as detailed in Chapter 4.2.1), while also protecting the samples from damage caused by excessive currents. However, it is crucial to understand that this approach does not provide absolute current limitation. For example, in a 0 V to 6 V voltage ramp with a 100 pA threshold, the trigger stops the forward sweep at the voltage level (V_{STOP}) where the current initially exceeds the threshold. It was discovered that increasing the sampling rate and ramp frequency reduces current overshoot and enhances precision. Nevertheless, after V_{STOP}, the system performs an inevitable backward sweep to its initial value. During this phase, dielectric breakdown, which depends on both the applied voltage and stress duration, could occur, potentially resulting in currents exceeding the predetermined threshold. This method also proves useful in recording current maps, as seen with h-BN on Cu, where it significantly reduced but did not completely prevent new defect formation. Overall, the adoption of software-based current limitation significantly enhances both the reliability and cost-effectiveness of C-AFM. This approach not only enables the investigation of delicate samples but also extends the usability of metal-coated probes, which provide a larger variety in spring constants and tip dimensions than solid Pt probes.

Finally, Chapter 4.2.2 introduced a novel sample holder integrated with a MOSFET. Unlike software-based current limitation this invention offers true current limitation in both forward and backward sweep directions. Differing from the conventional method of integrating resistors in series with the probe, this sample holder eliminates the need for prior knowledge of the sample's resistance. Additionally, it obviates the need for hardware modifications when switching between samples, a common requirement when measuring different samples using resistors. Instead, a simple adjustment of the gate voltage is sufficient to adapt to different sample types, which considerably streamlines the process. Compatible with standard SOT-23 housed transistors, the sample holder is highly customizable, making it suitable for a wide array of experiments. Its versatility also ensures compatibility with nearly all C-AFM systems. In essence, this sample holder significantly enhances the accuracy, reliability, and flexibility of C-AFM applications, which holds the potential to position it as an indispensable tool for researchers and practitioners in the field.

Conclusively, this thesis has successfully met all its initially stated objectives, contributing to a deeper understanding of probe performance in C-AFM and elucidating the various factors that influence their durability and effectiveness. In doing so, it has notably enhanced C-AFM reliability and cost-effectiveness. A key advancement made through this research is the refined ability to precisely control the currents during measurements. This precision is particularly beneficial for the analysis of sensitive samples, an aspect increasingly important given the ongoing trend of diminishing device dimensions in recent decades. The insights from this thesis could prove to be valuable in the development of future electronic devices, particularly with the industry's growing interest in incorporating functional single-atom layers. The results of this research not only address the current demands of nanoscale material analysis but also take a step towards paving the way for pioneering applications in the field of ultra-miniaturized electronic devices.

A References

[1] T.-J. King Liu and K. Kuhn, "Preface," in *CMOS and Beyond: Logic Switches for Terascale Integrated Circuits*, T.-J. King Liu and K. Kuhn Eds. Cambridge: Cambridge University Press, 2015, pp. xv-xviii.

[2] A. Spessot, R. Ritzenthaler, E. D. Litta, E. Dupuy, B. O'Sullivan, J. Bastos, E. Capogreco, K. Miyaguchi, V. Machkaoutsan, and Y. Yong, "80 nm Tall Thermally Stable Cost Effective Finfets for Advanced Dynamic Random Access Memory Periphery Devices for Artificial Intelligence/machine Learning and Automotive Applications," *Japanese Journal of Applied Physics*, vol. 60, no. SB, p. SBBB06, 2021.

[3] M. Alioto, *Enabling the Internet of Things: From Integrated Circuits to Integrated Systems*. M. Alioto, Ed, Cham, Switzerland: Springer International Publishing AG, 2017, pp. vii-ix.

[4] M. Min and S. Kadivar, "Accelerating Innovations in the New Era of HPC, 5G and Networking With Advanced 3D Packaging Technologies," in *2020 International Wafer Level Packaging Conference (IWLPC)*, 2020: IEEE, pp. 1-6.

[5] S. K. Moore and D. Schneider. "The State of the Transistor in 3 Charts." Spectrum.ieee.org. Accessed: Dec. 06, 2023 [Online]. Available: https://spectrum.ieee.org/transistor-density.

[6] W. H. Brattain, "Genesis of the Transistor," *The Physics Teacher*, vol. 6, no. 3, pp. 109-114, 1968.

[7] N. El-Atab and M. M. Hussain, "The Future of CMOS: More Moore or a New Disruptive Technology?," in *Advanced Nanoelectronics: Post-Silicon Materials and Devices*, N. El-Atab and M. M. Hussain, Eds., Weinheim, Germany: Wiley-VCH Verlag GmbH & Co. KGaA, 2019, pp. 1-31, 2018.

[8] M. Baklanov, M. Green, and K. Maex "Preface," in *Dielectric Films for Advanced Microelectronics*, M. Baklanov, M. Green, and K. Maex, Eds., Chichester, U.K.: John Wiley & Sons Ltd, 2007, pp. xv-xvii.

[9] G. E. Moore, "Cramming More Components Onto Integrated Circuits," *Proceedings of the IEEE*, vol. 86, no. 1, pp. 82-85, 1998.

[10] H. Iwai, "(Gordon E. Moore Award) Impact of Micro-/Nano-Electronics, Miniaturization Limit, and Technology Development for the Next 10 Years and After," *ECS Transactions*, vol. 102, no. 4, p. 81, 2021.

[11] H.-L. Ko, Q. H. Luc, P. Huang, J.-Y. Wu, S.M. Chen, N.-A. Tran, H.-T. Hsu, and E. Y. Chang, "Sub-10 nm Top Width Nanowire InGaAs Gate-All-Around MOSFETs With Improved Subthreshold Characteristics and Device Reliability," *IEEE Journal of the Electron Devices Society*, vol. 10, pp. 188-191, 2022.

[12] J. Kaur, "Life Beyond Moore: More Moore or More Than Moore - A Review," *Int. J. Comput. Sci. Mob. Comput*, vol. 5, pp. 233-237, 2016.

[13] X. Zheng, Y. T. Han, P. H. Seah, G. S. Lee, and K. C. Chng, "Differential C-AFM System for Semiconductor Failure Analysis," in *2016 IEEE 23rd International Symposium on the Physical and Failure Analysis of Integrated Circuits (IPFA)*, 2016: IEEE, pp. 370-373.

[14] J. Weber, Y. Yuan, S. Pazos, F. Kühnel, C. Metzke, J. Schätz, W. Frammelsberger, G. Benstetter, and M. Lanza, "Current-Limited Conductive Atomic Force Microscopy," *ACS Applied Materials & Interfaces*, vol. 15, no. 48, pp. 56365-56374, 2023.

[15] Bruker. "PFTUNA." Brukerafmprobes.com. Accessed: Nov. 10, 2023 [Online]. Available: https://www.brukerafmprobes.com/p-3762-pftuna.aspx.

[16] Bruker. "ContV-Pt." Brukerafmprobes.com. Accessed: Nov. 17, 2023 [Online]. Available: https://www.brukerafmprobes.com/p-3847-contv-pt.aspx.

[17] Bruker. "SCM-PIT-V2." Brukerafmprobes.com. Accessed: Nov. 17, 2023 [Online]. Available: https://www.brukerafmprobes.com/p-3950-scm-pit-v2.aspx.

[18] O. Krause, "Fabrication and Reliability of Conductive AFM Probes," *Conductive Atomic Force Microscopy: Applications in Nanomaterials*, M. Lanza, Ed., Weinheim, Germany: Wiley-VCH Verlag GmbH & Co. KGaA, 2017, pp. 29-44.

[19] C. Li, B. Pittenger, A. Mednick, M. Guide, and T.-Q. Nguyen, "Simultaneous Electrical and Mechanical Property Mapping at the Nanoscale with PeakForce TUNA," *Bruker Application Note #132,* 2011.

[20] M. Lanza, G. Bersuker, M. Porti, E. Miranda, M. Nafría, and X. Aymerich, "Resistive Switching in Hafnium Dioxide Layers: Local Phenomenon at Grain Boundaries," *Applied Physics Letters,* vol. 101, no. 19, 2012.

[21] R. Rottenfusser, "Education in Microscopy and Digital Imaging," zeiss-campus.magnet.fsu.edu. Accessed: Sept. 23, 2023 [Online]. Available: https://zeiss-campus.magnet.fsu.edu/articles/basics/resolution.html.

[22] E. Ruska, "The Development of the Electron Microscope and of Electron Microscopy," *Reviews of Modern Physics,* vol. 59, no. 3, p. 627, 1987.

[23] G. Binnig and H. Rohrer, "Scanning Tunneling Microscopy," *Surface Science,* vol. 126, no. 1-3, pp. 236-244, 1983.

[24] C. J. Chen, "Instrumentation," *Introduction to Scanning Tunneling Microscopy Third Edition*. C. J. Chen, Ed., New York, NY, USA: Oxford University Press, 2021, pp. 273-356.

[25] G. Binnig, C. F. Quate, and C. Gerber, "Atomic Force Microscope," *Physical Review Letters,* vol. 56, no. 9, p. 930, 1986.

[26] A. E. Moyer, "Robert Hooke's Ambiguous Presentation of" Hooke's Law"," *Isis,* vol. 68, no. 2, pp. 266-275, 1977.

[27] V. B. Baiburin, N. P. Konnov, and Y. P. Volkov, "Improved Optical Method for Measurement of AFM Cantilever Deflection," in *Three-Dimensional and Multidimensional Microscopy: Image Acquisition and Processing V,* 1998, vol. 3261: SPIE, pp. 187-192.

[28] C. Pan, Y. Shi, F. Hui, E. Grustan-Gutierrez, and M. Lanza, "History and Status of the CAFM," *Conductive Atomic Force Microscopy: Applications in Nanomaterials,* M. Lanza, Ed., Weinheim, Germany: Wiley-VCH Verlag GmbH & Co. KGaA, 2017, pp. 1-28.

[29] D. Sarid and V. Elings, "Review of Scanning Force Microscopy," *Journal of Vacuum Science & Technology B: Microelectronics and Nanometer Structures Processing, Measurement, and Phenomena,* vol. 9, no. 2, pp. 431-437, 1991.

[30] V. I. Santiso, "CAFM Nanoscale Electrical Properties and Reliability of HfO_2 Based Gate Dielectrics in Electron Devices: Impact of the Polycrystallization and Resistive Switching," Ph.D. dissertation, Department of Electronic Engineering, Universitat Autònoma de Barcelona, Barcelona, Spain, 2013.

[31] W. Frammelsberger, "Improved atomic force microscopy based techniques for electrical and structural characterisation of thin dielectric films," Ph.D. dissertation, Department of Computing, Engineering and Mathematical Sciences, University of the West of England, Bristol, U.K., 2006.

[32] D. K. Schroder, "Atomic Force Microscopy (AFM)," *Semiconductor material and device characterization*. D. K. Schroder, Ed., Hoboken, New Jersey, USA: John Wiley & Sons, Inc., 2015, pp. 545-547.

[33] G. Benstetter, A. Hofer, D. Liu, W. Frammelsberger, and M. Lanza, "Fundamentals of CAFM Operation Modes," *Conductive Atomic Force Microscopy: Applications in Nanomaterials,* M. Lanza, Ed., Weinheim, Germany: Wiley-VCH Verlag GmbH & Co. KGaA, 2017 pp. 45-77.

[34] A. Bayerl, "Variability and Reliability at the Nanoscale of Gate Dielectrics of MOS Devices and Graphene Based Structures," Ph.D. dissertation, Department of Electronic Engineering, Universitat Autònoma de Barcelona, Barcelona, Spain, 2013.

[35] N. Jalili and K. Laxminarayana, "A Review of Atomic Force Microscopy Imaging Systems: Application to Molecular Metrology and Biological Sciences," *Mechatronics*, vol. 14, no. 8, pp. 907-945, 2004.

[36] S.-I. Kitamura and M. I. M. Iwatsuki, "Observation of 7× 7 Reconstructed Structure on the Silicon (111) Surface using Ultrahigh Vacuum Noncontact Atomic Force Microscopy," *Japanese Journal of Applied Physics,* vol. 34, no. 1B, p. L145, 1995.

[37] C. Prater, P. Maivald, K. Kjoller, and M. Heaton, "Tapping Mode Imaging Applications and Technology," *Digital Instruments Nanonotes, Santa Barbara, California, USA*, 1995.

[38] C. A. Putman, K. O. Van der Werf, B. G. De Grooth, N. F. Van Hulst, and J. Greve, "Tapping Mode Atomic Force Microscopy in Liquid," *Applied Physics Letters*, vol. 64, no. 18, pp. 2454-2456, 1994.

[39] N. Ning, T. Mi, G. Chu, L.-Q. Zhang, L. Liu, M. Tian, H.-T. Yu, and Y.-L. Lu, "A Quantitative Approach to Study the Interface of Carbon Nanotubes/Elastomer Nanocomposites," *European Polymer Journal*, vol. 102, pp. 10-18, 2018.

[40] X.-R. Liu, X. Deng, R.-R. Liu, H.-J. Yan, Y.-G. *et al.*, "Single Nanowire Electrode Electrochemistry of Silicon Anode by In Situ Atomic Force Microscopy: Solid Electrolyte Interphase Growth and Mechanical Properties," *ACS Applied Materials & Interfaces,* vol. 6, no. 22, pp. 20317-20323, 2014.

[41] D. Mrđenović, D. Abbott, V. Mougel, W. Su, N. Kumar, and R. Zenobi, "Visualizing Surface Phase Separation in PS-PMMA Polymer Blends at the Nanoscale," *ACS Applied Materials & Interfaces,* vol. 14, no. 21, pp. 24938-24945, 2022.

[42] Bruker, "The Heartbeat," Bruker Nanoscope Help 2013. Accessed: Oct. 10, 2023.

[43] S. B. Kaemmer, "Introduction to Bruker's ScanAsyst and PeakForce Tapping AFM Technology," *Bruker Application Note #133*, 2011.

[44] K. Xu, W. Sun, Y. Shao, F. Wei, X. Zhang, W. Wang, and P. Li, "Recent Development of PeakForce Tapping Mode Atomic Force Microscopy and Its Applications on Nanoscience," *Nanotechnology Reviews*, vol. 7, no. 6, pp. 605-621, 2018.

[45] H.-J. Butt, B. Cappella, and M. Kappl, "Force Measurements With the Atomic Force Microscope: Technique, Interpretation and Applications," *Surface Science Reports*, vol. 59, no. 1-6, pp. 1-152, 2005.

[46] M. E. Dokukin and I. Sokolov, "Quantitative Mapping of the Elastic Modulus of Soft Materials with HarmoniX and PeakForce QNM AFM Modes," *Langmuir,* vol. 28, no. 46, pp. 16060-16071, 2012.

[47] M. P. Murrell, M. E. Welland, S. J. O’Shea, T. M. H. Wong, J. R. Barnes, A. W. McKinnon, M. Heyns, and S. Verhaverbeke, "Spatially Resolved Electrical Measurements of SiO_2 Gate Oxides Using Atomic Force Microscopy," *Applied Physics Letters,* vol. 62, no. 7, pp. 786-788, 1993.

[48] S. O’Shea, R. Atta, M. Murrell, and M. Welland, "Conducting Atomic Force Microscopy Study of Silicon Dioxide Breakdown," *Journal of Vacuum Science & Technology B: Microelectronics and Nanometer Structures Processing, Measurement, and Phenomena,* vol. 13, no. 5, pp. 1945-1952, 1995.

[49] T. G. Ruskell, R. K. Workman, D. Chen, D. Sarid, S. Dahl, and S. Gilbert, "High Resolution Fowler-Nordheim Field Emission Maps of Thin Silicon Oxide Layers," *Applied Physics Letters,* vol. 68, no. 1, pp. 93-95, 1996.

[50] A. Olbrich, B. Ebersberger, and C. Boit, "Nanoscale Electrical Characterization of Thin Oxides With Conducting Atomic Force Microscopy," in *1998 IEEE International Reliability Physics Symposium Proceedings. 36th Annual (Cat. No. 98CH36173),* 1998: IEEE, pp. 163-168.

[51] A. Olbrich, B. Ebersberger, and C. Boit, "Conducting Atomic Force Microscopy for Nanoscale Electrical Characterization of Thin SiO_2," *Applied Physics Letters,* vol. 73, no. 21, pp. 3114-3116, 1998.

[52] M. Lanza, K. Zhang, M. Porti, M. Nafría, Z. Y. Shen, L. F. Liu, J. F. Kang, D. Gilmer, and G. Bersuker, "Grain Boundaries as Preferential Sites for Resistive Switching in the HfO_2 Resistive Random Access Memory Structures," *Applied Physics Letters,* vol. 100, no. 12, 2012.

[53] M. Lanza, "A Review on Resistive Switching in High-k Dielectrics: A Nanoscale Point of View Using Conductive Atomic Force Microscope," *Materials,* vol. 7, no. 3, pp. 2155-2182, 2014.

[54] N. Xiao, M. A. Villena, B. Yuan, S. Chen, B. Wang, M. Eliáš, Y. Shi, F. Hui, X. Jing, and A. Scheuermann, "Resistive Random Access Memory Cells With a Bilayer TiO_2/SiO_x Insulating Stack for Simultaneous Filamentary and Distributed Resistive Switching," *Advanced Functional Materials,* vol. 27, no. 33, p. 1700384, 2017.

[55] G.-H. Lee, Y.-J. Yu, C. Lee, C. Dean, K. L. Shepard, P. Kim, J. Hone, "Electron Tunneling Through Atomically Flat and Ultrathin Hexagonal Boron Nitride," *Applied Physics Letters,* vol. 99, no. 24, 2011.

[56] Y. Ji, C. Pan, M. Zhang, S. Long, X. Lian, F. Miao, F. Hui, Y. Shi, L. Larcher, E. Wu, and M. Lanza, "Boron Nitride as Two Dimensional Dielectric: Reliability and Dielectric Breakdown," *Applied Physics Letters,* vol. 108, no. 1, 2016.

[57] Y. Hattori, T. Taniguchi, K. Watanabe, and K. Nagashio, "Layer-by-Layer Dielectric Breakdown of Hexagonal Boron Nitride," *ACS Nano,* vol. 9, no. 1, pp. 916-921, 2015.

[58] R. Martinez, N. Losilla, J. Martinez, Y. Huttel, and R. Garcia, "Patterning Polymeric Structures with 2 nm Resolution at 3 nm Half Pitch in Ambient Conditions," *Nano Letters,* vol. 7, no. 7, pp. 1846-1850, 2007.

[59] J. Zhao and J. J. Davis, "Force Dependent Metalloprotein Conductance by Conducting Atomic Force Microscopy," *Nanotechnology,* vol. 14, no. 9, p. 1023, 2003.

[60] S. L. Howell, S. Padalkar, K. Yoon, Q. Li, D. D. Koleske, J. J. Wierer, G. T. Wang, and L. J. Lauhon, "Spatial Mapping of Efficiency of GaN/InGaN Nanowire Array Solar Cells Using Scanning Photocurrent Microscopy," *Nano Letters,* vol. 13, no. 11, pp. 5123-5128, 2013.

[61] C. Pan, J. Hu, E. Grustan-Gutierrez, M. T. Hoang, H. Duan, J. Yvonnet, A. Mirushchenkov, G. Chambaud, and M. Lanza, "Suppression of Nanowire Clustering in Hybrid Energy Harvesters," *Journal of Materials Chemistry C,* vol. 4, no. 16, pp. 3646-3653, 2016.

[62] Bruker. "Conductive AFM (C-AFM)." Brukerafmprobes.com. Accessed: Oct. 24, 2023 [Online]. Available: https://www.brukerafmprobes.com/c-271-conductive-afm-cafm.aspx.

[63] Nanosensors, "Electrostatic Force Microscopy / Electrical Measurement AFM Probes," *Nanosensors.com,* 2023. [Online]. Available: https://www.nanosensors.com/electrostatic-force-modulation-electrical-measurement-afm-tips.

[64] Budgetsensors. "Conductive AFM Probes." Budgetsensors.com. Accessed: Oct. 24, 2023 [Online]. Available: https://www.budgetsensors.com/conductive-afm-probes.

[65] L. Aguilera, M. Lanza, M. Porti, J. Grifoll, M. Nafría, and X. Aymerich, "Improving the Electrical Performance of a Conductive Atomic Force Microscope With a Logarithmic Current-to-Voltage Converter," *Review of Scientific Instruments,* vol. 79, no. 7, 2008.

[66] Oxford Instruments Asylum Research Inc., "AFM Tools for Nanoscale Electrical Characterization," *Application Note 29,* 2018.

[67] A. Ranjan, N. Raghavan, K. Shubhakar, R. Thamankar, J. Molina, S. J. O’Shea, M. Bosman, and K. L. Pey, "CAFM Based Spectroscopy of Stress-Induced Defects in HfO_2 With Experimental Evidence of the Clustering Model and Metastable Vacancy Defect State," in *2016 IEEE International Reliability Physics Symposium (IRPS),* 2016: IEEE, pp. 7A-4-1-7A-4-7.

[68] V. Iglesias, X. Jing, and M. Lanza, "Combination of Semiconductor Parameter Analyzer and Conductive Atomic Force Microscope for Advanced Nanoelectronic Characterization," *Conductive Atomic Force Microscopy: Applications in Nanomaterials,* M. Lanza, Ed., Weinheim, Germany: Wiley-VCH Verlag GmbH & Co. KGaA, 2017 pp. 225-241.

[69] T. Albrecht, S. Akamine, T. Carver, and C. Quate, "Microfabrication of Cantilever Styli for the Atomic Force Microscope," *Journal of Vacuum Science & Technology A: Vacuum, Surfaces, and Films,* vol. 8, no. 4, pp. 3386-3396, 1990.

[70] O. Wolter, T. Bayer, and J. Greschner, "Micromachined Silicon Sensors for Scanning Force Microscopy," *Journal of Vacuum Science & Technology B: Microelectronics and Nanometer Structures Processing, Measurement, and Phenomena,* vol. 9, no. 2, pp. 1353-1357, 1991.

[71] J. H. Hafner, "Probes in Scanning Microscopies," *Nanotribology and Nanomechanics: An Introduction*, B. Bhushan, Ed., Berlin, Heidelberg, Germany: Springer, 2005, pp. 117-139.

[72] J. Weber, Y. Yuan, F. Kühnel, C. Metzke, J. Schätz, W. Frammelsberger, G. Benstetter, and M. Lanza, "Solid Platinum Nanoprobes for Highly Reliable Conductive Atomic Force Microscopy," *ACS Applied Materials & Interfaces,* vol. 15, no. 17, pp. 21602-21608, 2023.

[73] S. O’Shea, R. Atta, and M. Welland, "Characterization of Tips for Conducting Atomic Force Microscopy," *Review of Scientific Instruments,* vol. 66, no. 3, pp. 2508-2512, 1995.

[74] T. Trenkler, T. Hantschel, R. Stephenson, P. De Wolf, W. Vanderforst, L. Hellemans, A. Malavé, D. Büchel, E. Oesterschulze, W. Kulisch, P. Niedermann, T. Sulzbach, and O. Ohlsson, "Evaluating Probes for “Electrical”

Atomic Force Microscopy," *Journal of Vacuum Science & Technology B: Microelectronics and Nanometer Structures Processing, Measurement, and Phenomena,* vol. 18, no. 1, pp. 418-427, 2000.

[75] P. Niedermann, W. Hänni, D. Morel, A. Perret, N. Skinner, P.-F. Indermühle, N.F. de Rooij, and P. Buffat, "CVD Diamond Probes for Nanotechnology," *Applied Physics A: Materials Science & Processing,* vol. 66, pp. S31-S34, 1998.

[76] P. Niedermann, W. Hänni, N. Blanc, R. Christoph, and J. Burger, "Chemical Vapor Deposition Diamond for Tips in Nanoprobe Experiments," *Journal of Vacuum Science & Technology A: Vacuum, Surfaces, and Films,* vol. 14, no. 3, pp. 1233-1236, 1996.

[77] Q. Liang, A. Stanishevsky, and Y. K. Vohra, "Tribological Properties of Undoped and Boron-Doped Nanocrystalline Diamond Films," *Thin Solid Films,* vol. 517, no. 2, pp. 800-804, 2008.

[78] T. Trenkler, T. Hantschel, W. Vanderforst, L. Hellemans, W. Kulisch, E. Oesterschulze, P. Niedermann, T. Sulzbach, "Characterization of Conductive Probes for Atomic Force Microscopy," in *Design, Test, and Microfabrication of MEMS and MOEMS,* 1999, vol. 3680: SPIE, pp. 1168-1179.

[79] T. Hantschel, P. De Wolf, T. Trenkler, R. Stephenson, and W. Vandervorst, "Fabrication and Use of Metal Tip and Tip-on-Tip Probes for AFM-Based Device Analysis," in *Materials and Device Characterization in Micromachining*, 1998, vol. 3512: SPIE, pp. 92-103.

[80] T. Hantschel, R. Stephenson, T. Trenkler, P. De Wolf, and W. Vandervorst, "Characterization of Silicon Cantilevers With Integrated Pyramidal Metal Tips in Atomic Force Microscopy," in *Design, Test, and Microfabrication of MEMS and MOEMS,* 1999, vol. 3680: SPIE, pp. 994-1005.

[81] T. Hantschel, C. Derneulemeester, P. Eyben, V. Schulz, O. Richard, H. Bender, and W. Vanderforst, "Conductive Diamond Tips With Sub-Nanometer Electrical Resolution for Characterization of Nanoelectronics Device Structures," *Physica Status Solidi (a),* vol. 206, no. 9, pp. 2077-2081, 2009.

[82] S. Murarka, "Refractory Silicides for Integrated Circuits," *Journal of Vacuum Science and Technology,* vol. 17, no. 4, pp. 775-792, 1980.

[83] Rocky Mountain Nanotechnology. "Technical Data." Rmnano.com. Accessed: Oct. 25, 2023 [Online]. Available: https://rmnano.com/tech-data.

[84] Nanoworld, "ArrowTM UHF." Nanoworld.com. Accessed: Oct. 25, 2023 [Online]. Available: https://www.highspeedscanning.com/arrow-uhf.html.

[85] O. Krause, A. Sebastian, and M. Despont, "Platinum Silicide Probes: A Novel Approach to Manufacture Highly Conductive AFM Probes with Small Radii and High Wear Resistance." in *NSTI Nanotechnology Conference and Expo,* 2012.

[86] Nanoworld. "CDT-FMR." Nanoworld.com. Accessed: Nov. 10, 2023 [Online]. Available: https://www.nanoworld.com/pointprobe-conductive-diamond-coated-force-modulation-mode-afm-tip-cdt-fmr

[87] Kteknano. "DCP11." Kteknano.com. Accessed: Nov. 10, 2023 [Online]. Available: https://kteknano.com/product/dcp11/

[88] Rocky Mountain Nanotechnology. "25Pt300B." Rmnano.com. Accessed: Nov. 17, 2023 [Online]. Available: https://rmnano.com/tech-data.

[89] Bruker. "AD-40-AS." Brukerafmprobes.com. Accessed: Nov. 10, 2023 [Online]. Available: https://www.brukerafmprobes.com/p-3970-ad-40-as.aspx

[90] F. Hui, P. Vajha, Y. Shi, Y. Ji, H. Duan, A. Padovani, L. Larcher, X. R. Li, J. J. Xu, and M. Lanza, "Moving Graphene Devices From Lab to Market: Advanced Graphene-Coated Nanoprobes," *Nanoscale,* vol. 8, no. 16, pp. 8466-8473, 2016.

[91] L. Sirghi, O. Kylián, D. Gilliland, G. Ceccone, and F. Rossi, "Cleaning and Hydrophilization of Atomic Force Microscopy Silicon Probes," *The Journal of Physical Chemistry B*, vol. 110, no. 51, pp. 25975-25981, 2006.

[92] N. L. Tolman, R. Bai, and H. Liu, "Hydrocarbons in the Meniscus: Effects on Conductive Atomic Force Microscopy," *Langmuir*, vol. 39, no. 12, pp. 4274-4281, 2023.

[93] S. Chen, L. Jiang, M. Buckwell, X. Jing, Y. Ji, E. Grustan Gutierrez, F. Hui, Y. Shi, M. Rommel, A. Paskaleva, G. Benstetter, W. H. Ng, A. Mehonic, A. J. Kenyon, and M. Lanza, "On the Limits of Scalpel AFM for the 3D Electrical Characterization of Nanomaterials," *Advanced Functional Materials*, vol. 28, no. 52, p. 1802266, 2018.

[94] C. Wen, X. Jing, F. F. Hitzel, C. Pan, G. Benstetter, and M. Lanza, "In Situ Observation of Current Generation in ZnO Nanowire Based Nanogenerators Using a CAFM Integrated Into an SEM," *ACS Applied Materials & interfaces*, vol. 11, no. 17, pp. 15183-15188, 2019.

[95] G. U. Lee, D. A. Kidwell, and R. J. Colton, " Sensing Discrete Streptavidin-Biotin Interactions With Atomic Force Microscopy," *Langmuir*, vol. 10, no. 2, pp. 354-357, 1994.

[96] Y. Gan and G. V. Franks, " Cleaning Afm Colloidal Probes by Mechanically Scrubbing With Supersharp “Brushes”," *Ultramicroscopy*, vol. 109, no. 8, pp. 1061-1065, 2009.

[97] M. M. F. Elabd, "Transport Properties of Metal-Metal and Metal-Insulator Heterostructures," Ph.D. dissertation, Lehrstuhl für Theoretische Physik II, Universität Augsburg, Augsburg, Germany, 2010.

[98] G. Milano, S. Porro, I. Valov, and C. Ricciardi, "Recent Developments and Perspectives for Memristive Devices Based on Metal Oxide Nanowires," *Advanced Electronic Materials*, vol. 5, no. 9, p. 1800909, 2019.

[99] C. Kittel and P. McEuen, "Nanostructures" *Introduction to Solid State Physics*. John Wiley & Sons, 2018. C. Kittel and P. McEuen, Eds., Hoboken, New Jersey, USA: John Wiley & Sons, Inc., 2013, pp. 515-562.

[100] E. A. Miranda, C. Walczyk, C. Wenger, and T. Schroeder, "Model for the Resistive Switching Effect in HfO_2 MIM Structures Based on the Transmission Properties of Narrow Constrictions," *IEEE Electron Device Letters*, vol. 31, no. 6, pp. 609-611, 2010.

[101] Budgetsensors. "ElectriTap300-G." Budgetsensors.com. Accessed: Oct. 12, 2023 [Online]. Available: https://www.budgetsensors.com/tapping-mode-afm-probe-platinum-electritap300.

[102] L. Cao, R. Liu, W. Zhang, Y. Wang, G. Wang, Z. Song, Z. Weng, and Z. Wang, "High-Reliability Graphene-Wrapped Nanoprobes for Scanning Probe Microscopy," *Nanotechnology*, vol. 33, no. 5, p. 055704, 2021.

[103] F. Thuselt, "Ohmsche Kontakte, " *Physik der Halbleiterbauelemente Einführendes Lehrbuch für Ingenieure und Physiker*, F. Thuselt, Ed., Berlin, Heidelberg, Germany: Springer, 2011, pp. 262-263.

[104] S. M. Sze, "Metal-Semiconductor Contacts," *Semiconductor Devices: Physics and Technology*, S. M. Sze, Ed., Hoboken, New Jersey, USA: John Wiley & Sons, Inc., 2006, pp. 134-196.

[105] Electronic-notes, "Understanding Schottky Diode Characteristics & Specifications." Accessed: Oct. 26, 2023 [Online]. Available: https://www.electronics-notes.com/articles/electronic_components/diode/schottky-barrier-diode-characteristics-specifications-parameters.php.

[106] S. Cui, "Metal-Semiconductor Contacts." Eng.libretexts.org. Accessed: Oct. 26, 2023 [Online]. Available: https://eng.libretexts.org/Bookshelves/Materials_Science/Supplemental_Modules_(Materials_Science)/Semiconductors/Metal-Semiconductors_Contacts.

[107] H. Lüth, "Metal-Semiconductor Junctions and Semiconductor Heterostructures," *Solid Surfaces, Interfaces and Thin Films*. H. Lüth, Ed., Berlin, Heidelberg, Germany: Springer, 2001, pp. 381-434.

[108] S. Kremmer, C. Teichert, E. Pischler, H. Gold, F. Kuchar, and M. Schatzmayr, "Characterization of silicon gate oxides by conducting atomic force microscopy," *Surface and Interface Analysis: An International Journal devoted to the development and application of techniques for the analysis of surfaces, interfaces and thin films*, vol. 33, no. 2, pp. 168-172, 2002.

[109] W. Polspoel, W. Vandervorst, J. Petry, T. Conard, and A. Benedetti, "Comparison of Electric Properties of Ultra-Thin Thermal and Plasma Nitrided Silicon Oxides with Different Post-Deposition Treatments Using C-AFM," *Microelectronic Engineering,* vol. 80, pp. 436-439, 2005.

[110] J. Suñé, M. Nafría, E. Miranda, X. Oriols, R. Rodriguez, and X. Aymerich, "Failure Physics of Ultra-Thin SiO_2 Gate Oxides Near Their Scaling Limit," *Semiconductor Science and Technology,* vol. 15, no. 5, p. 445, 2000.

[111] X. Blasco, M. Nafría, X. Aymerich, J. Petry, and W. Vandervorst, "Breakdown Spots of Ultra-Thin (EOT< 1.5 nm) HfO_2/SiO_2 Stacks Observed With Enhanced-CAFM," *Microelectronics Reliability,* vol. 45, no. 5-6, pp. 811-814, 2005.

[112] H. J. Uppal, S. Bernardini, E. Efthymiou, S. N. Volkos, A. Dimoulas, V. Markevich, B. Hamilton, and A. R. Peaker, "Nanoscale Electrical Characterization of Ultrathin High-K Dielectric MOS Stacks: A Conducting AFM Study," *Materials Science in Semiconductor Processing,* vol. 11, no. 5-6, pp. 250-253, 2008.

[113] L. Britnell, R. V. Gorbachev, R. Jalil, B. D. Belle, F. Schedin, M. I. Katsnelson, L. Eaves, S. V. Morozov, A. S. Mayorov, N. M. R. Peres, A. H. C. Neto, J. Leist, A. K. Geim, L. A. Ponomarenko, and K. S. Novoslov, "Atomically Thin Boron Nitride: A Tunnelling Barrier for Graphene Devices," *arXiv preprint arXiv:1202.0735,* 2012.

[114] C.-Y. Zhu, J.-K. Qin, P.-Y. Huang, H.-L. Sun, N.-F. Sun, Y.-L. Shi, L. Zhen, and C.-Y. Xu, "2D Indium Phosphorus Sulfide ($In_2P_3S_9$): An Emerging van der Waals High-k Dielectrics," *Small,* vol. 18, no. 5, p. 2104401, 2022.

[115] F.-C. Chiu, "A Review on Conduction Mechanisms in Dielectric Films," *Advances in Materials Science and Engineering,* vol. 2014, 2014.

[116] K. H. Hammoud, "Parameters Optimization of a Charge Transport Model for the Electrical Characterization of Dielectric Materials," Ph.D. dissertation, Université Paul Sabatier-Toulouse III, Toulouse, France, 2022.

[117] B. L. Weeks, M. W. Vaughn, and J. J. DeYoreo, "Direct Imaging of Meniscus Formation in Atomic Force Microscopy Using Environmental Scanning Electron Microscopy," *Langmuir,* vol. 21, no. 18, pp. 8096-8098, 2005.

[118] M. Porti, M.-C. Blum, M. Nafría, and X. Aymerich, "Imaging Breakdown Spots in SiO/sub 2/films and MOS Devices With a Conductive Atomic Force Microscope," *IEEE Transactions on Device and Materials Reliability,* vol. 2, no. 4, pp. 94-101, 2002.

[119] S. Kremmer, S. Peissl, C. Teichert, and F. Kuchar, "Conducting Atomic-Force Microscopy Investigations on Thin Silicon Gate Oxides: Influence of Tip Shape and Humidity," in *ISTFA 2002,* 2002: ASM International, pp. 473-482.

[120] M. Heim, *Elektrische Leitfähigkeit oberflächenadsorbierter Wasserschichten und deren Anwendung zur Rastertunnelmikroskopie von Isolatoren und biologischen Molekülen*. Shaker, 1998.

[121] M. Lanza, M. Porti, M. Nafría, X. Aymerich, E. Whittaker, and B. Hamilton, "UHV CAFM Characterization of High-K Dielectrics: Effect of the Technique Resolution on the Pre-and Post-Breakdown Electrical Measurements," *Microelectronics Reliability,* vol. 50, no. 9-11, pp. 1312-1315, 2010.

[122] U. Celano, T. Hantschel, G. Giammaria, R. C. Chintala, T. Conrad, H. Bender, and W. Vandervorst, "Evaluation of the Electrical Contact Area in Contact-Mode Scanning Probe Microscopy," *Journal of Applied Physics,* vol. 117, no. 21, 2015.

[123] F. Hui, S. Chen, X. Liang, B. Yuan, Y. Jing, Y. Shi, and M. Lanza, "Graphene Coated Nanoprobes: A Review," *Crystals,* vol. 7, no. 9, p. 269, 2017.

[124] S. Kremmer, S. Peissl, C. Teichert, F. Kuchar, and H. Hofer, "Modification and Characterization of Thin Silicon Gate Oxides Using Conducting Atomic Force Microscopy," *Materials Science and Engineering: B,* vol. 102, no. 1-3, pp. 88-93, 2003.

[125] T. Clarysse, P. De Wolf, H. Bender, and W. Vandervorst, "Recent Insights Into the Physical Modeling of the Spreading Resistance Point Contact," *Journal of Vacuum Science & Technology B: Microelectronics and Nanometer Structures Processing, Measurement, and Phenomena,* vol. 14, no. 1, pp. 358-368, 1996.

[126] S. Doering, R. Rudolf, M. Pinkert, H. Roetz, C. Wagner, S. Eckl, M. Strasser, A. Wachowiak, and T. Mikolajick, "Scanning Spreading Resistance Microscopy for Failure Analysis of nLDMOS Devices With Decreased Breakdown Voltage," *Microelectronics Reliability,* vol. 54, no. 9-10, pp. 2128-2132, 2014.

[127] A. Ranjan, S. J. O’Shea, A. Padovani, T. Su, P. La Torraca, Y. S. Ang, M. S. Munde, C. Zhang, Y. Zhang, M. Bosman, N. Raghavan, and K. L. Pey, "Molecular Bridges Link Monolayers of Hexagonal Boron Nitride during Dielectric Breakdown," *ACS Applied Electronic Materials,* vol. 5, no. 2, pp. 1262-1276, 2023.

[128] M. Nafría, J. Suñé, and X. Aymerich, "Exploratory Observations of Post-Breakdown Conduction in Polycrystalline-Silicon and Metal-Gated Thin-Oxide Metal-Oxide-Semiconductor Capacitors," *Journal of Applied Physics,* vol. 73, no. 1, pp. 205-215, 1993.

[129] J. Suñe, M. Nafría, and X. Aymerich, "Reversible Dielectric Breakdown of Thin Gate Oxides in MOS Devices," *Microelectronics Reliability,* vol. 33, no. 7, pp. 1031-1039, 1993.

[130] M. Lanza, H. S. Philip Wong, E. Pop, D. Lelmini, D. Strukov, B. C. Regan, L. Larcher, M. A. Villena, J. J. Yang, L. Goux, A. Belmonte, Y. Yang, F. M. Puglisi, J. Kang, B. Magyari-Köpe, E. Yalon, A. Kenyon, M. Buckwell, A. Mehonic, A. Shluger, H. Li, T.-H. Hou, B. Hudec, D. Akinwande, R. Ge, S. Ambrogio, J. B. Roldan, E. Miranda, J. Suñe, K. L. Pey, X. Wu, N. Raghavan, E. Wu, W. D. Lu, G. Navarro, W. Zhang, H. Wu, R. Li, A. Holleitner, U. Wurstbauer, M. C. Lemme, M. Liu, S. Long, Q. Liu, H. Lv, A. Padovani, P. Pavan, I. Valov, Y. Jing, T. Han, K. Zhu, S. Chen, F. Hui, and Y. Shi, "Recommended methods to study resistive switching devices," *Advanced Electronic Materials,* vol. 5, no. 1, p. 1800143, 2019.

[131] J. Simmons and R. Verderber, "New Conduction and Reversible Memory Phenomena in Thin Insulating Films," *Proceedings of the Royal Society of London. Series A. Mathematical and Physical Sciences,* vol. 301, no. 1464, pp. 77-102, 1967.

[132] H.-S. P. Wong, H.-Y. Lee, S. Yu, Y.-S. Chen, Y. Wu, P.-S. Chen, B. Lee, F. T. Chen, and M.-J. Tsai, "Metal-oxide RRAM," *Proceedings of the IEEE,* vol. 100, no. 6, pp. 1951-1970, 2012.

[133] S. Yu, "Introduction to RRAM Technology," *Resistive Random Access Memory - From Devices to Array Architectures*, S. Yu, Ed., San Rafael, California (USA): Morgan & Claypool Publishers, 2016. pp. 1-7

[134] S. Seo, M. J. Lee, D. H. Seo, E. J. Jeoung, D. S. Suh, Y. S. Joung, I. K. Yoo, I. R. Hwang, S. H. Kim, I. S. Byun, J. S. Kim, J. S. Choi, and B. H. Park, "Reproducible Resistance Switching in Polycrystalline NiO Films," *Applied Physics Letters,* vol. 85, no. 23, pp. 5655-5657, 2004.

[135] B. Choi, D. S. Jeong, S. K. Kim, C. Rohde, S. Choi, J. H. Oh, H. J. Kim, C. S. Hwang, K. Szot, R. Waser, B. Reichenberg, and S. Tiedke, "Resistive Switching Mechanism of TiO_2 Thin Films Grown by Atomic-Layer Deposition," *Journal of Applied Physics,* vol. 98, no. 3, 2005.

[136] A. Chen, S. Haddad, Y.-C. Wu, T. N. Fang, Z. Lan, S. Avanzino, S. Pangrle, M. Buynoski, M. Rathor, W. Cai, N. Tripsas, C. Bill, M. Van Buskirk, and M. Taguchi, "Non-Volatile Resistive Switching for Advanced Memory Applications," in *IEEE International Electron Devices Meeting, 2005. IEDM Technical Digest.*, 2005: IEEE, pp. 746-749.

[137] C.-Y. Lin, C.-Y. Wu, C.-Y. Wu, T.-Y. Tseng, and C. Hu, "Modified Resistive Switching Behavior of ZrO_2 Memory Films Based on the Interface Layer Formed by Using Ti Top Electrode," *Journal of Applied Physics,* vol. 102, no. 9, 2007.

[138] N. Xu, L. Liu, Y. Sun, X. Liu, D. Han, Y. Wang, R. Han, J. Kang, and B. Yu, "Characteristics and Mechanism of Conduction/Set Process in TiN∕ZnO∕Pt Resistance Switching Random-Access Memories," *Applied Physics Letters,* vol. 92, no. 23, 2008.

[139] H. Y. Lee, P. S. Chen, T. Y. Wu, Y. S. Chen, C. C. Wang, P. J. Tzeng, C. H. Lin, F. Chen, C. H. Lien, and M.-J. Tsai "Low Power and High Speed Bipolar Switching With a Thin Reactive Ti Buffer Layer in Robust HfO_2 Based RRAM," in *2008 IEEE International Electron Devices Meeting,* 2008: IEEE, pp. 1-4.

[140] Z. Wei, Y. Kanzawa, K. Arita, Y. Katoh, K. Kawai, S. Muraoka, S. Mitani, S. Fuji, K. Katayama, M. Iijima, T. Mikawa, T. Ninomiya, R. Miyanaga, Y. Kawashima, K. Tsuji, A. Himeno, T. Okada, R. Azuma, K. Shimakawa, H. Sugaya, T. Takagi, R. Yasuhara, K. Horiba, H. Kumigashira, and M. Oshima, "Highly Reliable TaOx ReRAM and Direct Evidence of Redox Reaction Mechanism," in *2008 IEEE International Electron Devices Meeting,* 2008: IEEE, pp. 1-4.

[141] W. Kim, S. I. Park, Z. Zhang, Y. Yang-Liauw, D. Sekar, H.-S. Philip Wong, and S. Simon Wong, "Forming-Free Nitrogen-Doped AlO_x RRAM with sub-μA Programming Current," in *2011 Symposium on VLSI Technology-Digest of Technical Papers,* 2011: IEEE, pp. 22-23.

[142] S. Baek, D. Lee, J. Kim, S. H. Hong, O. Kim, and M. Ree, "Novel Digital Nonvolatile Memory Devices Based on Semiconducting Polymer Thin Films," *Advanced Functional Materials,* vol. 17, no. 15, pp. 2637-2644, 2007.

[143] F. Hui, E. Grustan-Gutierrez, S. Long, Q. Liu, A. K. Ott, A. C. Ferrari, and M. Lanza, "Graphene and Related Materials for Resistive Random Access Memories," *Advanced Electronic Materials,* vol. 3, no. 8, p. 1600195, 2017.

[144] R. Waser and M. Aono, "Nanoionics-Based Resistive Switching Memories," *Nature Materials,* vol. 6, no. 11, pp. 833-840, 2007.

[145] Y. Hao, H. Wu, Y. Yang, Q. Liu, X. Gong, G. Han, and M. Li, "Preface to the Special Issue on Beyond Moore: Resistive Switching Devices for Emerging Memory and Neuromorphic Computing," *Journal of Semiconductors,* vol. 42, no. 1, pp. 010101-010101-2, 2021.

[146] J. H. Stathis, "Percolation Models for Gate Oxide Breakdown," *Journal of Applied Physics,* vol. 86, no. 10, pp. 5757-5766, 1999.

[147] E. Miranda and J. Suñe, "Electron Transport Through Broken Down Ultra-Thin SiO_2 Layers in MOS Devices," *Microelectronics Reliability,* vol. 44, no. 1, pp. 1-23, 2004.

[148] J. McPherson and R. Khamankar, "Molecular Model for Intrinsic Time-Dependent Dielectric Breakdown in SiO_2 Dielectrics and the Reliability Implications for Hyper-Thin Gate Oxide," *Semiconductor Science and Technology,* vol. 15, no. 5, p. 462, 2000.

[149] D. DiMaria, E. Cartier, and D. Arnold, "Impact Ionization, Trap Creation, Degradation, and Breakdown in Silicon Dioxide Films on Silicon," *Journal of Applied Physics,* vol. 73, no. 7, pp. 3367-3384, 1993.

[150] D. DiMaria, "Defect Generation in Ultrathin Silicon Dioxide Films Produced by Anode Hole Injection," *Applied Physics Letters,* vol. 77, no. 17, pp. 2716-2718, 2000.

[151] J. Suñé and E. Wu, "Quantitative Two-Step Hydrogen Model of SiO_2 Gate Oxide Breakdown," *Solid-State Electronics,* vol. 46, no. 11, pp. 1825-1837, 2002.

[152] R. Degraeve, B. Kaczer, and G. Groeseneken, "Degradation and Breakdown in Thin Oxide Layers: Mechanisms, Models and Reliability Prediction," *Microelectronics Reliability,* vol. 39, no. 10, pp. 1445-1460, 1999.

[153] J. S. Suehle, "Ultrathin Gate Oxide Reliability: Physical Models, Statistics, and Characterization," *IEEE Transactions on Electron Devices,* vol. 49, no. 6, pp. 958-971, 2002.

[154] R.-P. Vollertsen and E. Wu, "Voltage Acceleration and t63. 2 of 1.6–10 nm Gate Oxides," *Microelectronics Reliability,* vol. 44, no. 6, pp. 909-916, 2004.

[155] P. E. Nicollian, W. R. Hunter, and J. C. Hu, "Experimental Evidence for Voltage Driven Breakdown Models in Ultrathin Gate Oxides," in *2000 IEEE International Reliability Physics Symposium Proceedings. 38th Annual (Cat. No. 00CH37059)*, 2000: IEEE, pp. 7-15.

[156] J. H. Stathis, "Reliability Limits for the Gate Insulator in CMOS Technology," *IBM Journal of Research and Development,* vol. 46, no. 2.3, pp. 265-286, 2002.

[157] E. Y. Wu, J. Suñé, W. Lai, A. Vayshenker, E. Nowak, and D. Harmon, "Critical Reliability Challenges in Scaling SiO_2-Based Dielectric to its Limit," *Microelectronics Reliability,* vol. 43, no. 8, pp. 1175-1184, 2003.

[158] E. Y. Wu, J. H. Stathis, and L.-K. Han, "Ultra-Thin Oxide Reliability for ULSI Applications," *Semiconductor Science and Technology,* vol. 15, no. 5, p. 425, 2000.

[159] T. Hori, "MIS Structure," *Gate Dielectrics and MOS ULSIs: Principles, Technologies and Applications,* T. Hori, Ed., Berlin, Heidelberg, Germany: Springer, 2012, pp. 23-74.

[160] K. F. Schuegraf and C. Hu, "Reliability of Thin SiO_2," *Semiconductor Science and Technology,* vol. 9, no. 5, p. 989, 1994.

[161] T. Pompl, C. Engel, H. Wurzer, and M. Kerber, "Soft Breakdown and Hard Breakdown in Ultra-Thin Oxides," *Microelectronics Reliability,* vol. 41, no. 4, pp. 543-551, 2001.

[162] Y. Kumagai, A. Teramoto, S. Sugawa, T. Suwa, and T. Ohmi, "Statistical Evaluation for Anomalous SILC of Tunnel Oxide Using Integrated Array TEG," in *2008 IEEE International Reliability Physics Symposium*, 2008: IEEE, pp. 219-224.

[163] D. DiMaria and E. Cartier, "Mechanism for Stress-Induced Leakage Currents in Thin Silicon Dioxide Films," *Journal of Applied physics,* vol. 78, no. 6, pp. 3883-3894, 1995.

[164] E. Y. Wu and J. Suné, "Power-Law Voltage Acceleration: A Key Element for Ultra-Thin Gate Oxide Reliability," *Microelectronics Reliability,* vol. 45, no. 12, pp. 1809-1834, 2005.

[165] T. Pompl, "Gateisolatoren für MOS-Feldeffekttransistoren," Ph.D. dissertation, Fakultät für Elektrotechnik, Institut für Physik, *Universität der Bundeswehr München*, München, Germany 2000.

[166] S. N. Luko, "A Review of the Weibull Distribution and Selected Engineering Applications," *SAE Transactions,* pp. 398-412, 1999.

[167] A. Martin, P. O'Sullivan, and A. Mathewson, "Dielectric Reliability Measurement Methods: A Review," *Microelectronics Reliability,* vol. 38, no. 1, pp. 37-72, 1998.

[168] M. Porti, M. Nafría, X. Aymerich, A. Olbrich, and B. Ebersberger, "Nanoscale Observations of the Electrical Conduction of Ultrathin SiO/sub 2/Films with Conducting Atomic Force Microscopy," in *2001 IEEE International Reliability Physics Symposium Proceedings. 39th Annual (Cat. No. 00CH37167),* 2001: IEEE, pp. 156-162.

[169] G. Ghibaudo, G. Pananakakis, R. Kies, E. Vincent, and C. Papadas, "Accelerated Dielectric Breakdown and Wear Out Standard Testing Methods and Structures for Reliability Evaluation of Thin Oxides," *Microelectronics Reliability,* vol. 39, no. 5, pp. 597-613, 1999.

[170] M. Nafría, J. Suñe, and X. Aymerich, "Breakdown of Thin Gate Silicon Dioxide Films - A Review," *Microelectronics Reliability,* vol. 36, no. 7-8, pp. 871-905, 1996.

[171] J. H. Stathis, "Physical and Predictive Models of Ultrathin Oxide Reliability in CMOS Devices and Circuits," *IEEE Transactions on device and materials reliability,* vol. 1, no. 1, pp. 43-59, 2001.

[172] E. Wu, J. Suñe, W. Lai, E. Nowak, J. McKenna, A. Vayshenker, and D. Harmon, "Interplay of Voltage and Temperature Acceleration of Oxide Breakdown for Ultra-Thin Gate Oxides," *Solid-State Electronics,* vol. 46, no. 11, pp. 1787-1798, 2002.

[173] P. Bøggild, "Research on Scalable Graphene Faces a Reproducibility Gap," *Nature Communications,* vol. 14, no. 1, p. 1126, 2023.

[174] A. P. Kauling, A. T. Seefeldt, D. R. Pisoni, R. C. Pradepp, R. Bentini, R. V. B. Oliveira, K. S. Novoselov, and A. H. C. Neto, "The Worldwide Graphene Flake Production," *Advanced Materials,* vol. 30, no. 44, p. 1803784, 2018.

[175] C. Hao, H. Xu, Y. Chen, Y. Zhang, and H. Zheng, "Investigation of the Topography-Dependent Current in Conductive AFM and the Calibration Method," *arXiv preprint arXiv:2307.09840,* 2023.

[176] L. Jiang. J. Weber, F. M. Puglisi, P. Pavan, L. Larcher, W. Frammelsberger, G. Benstetter, and M. Lanza, "Understanding Current Instabilities in Conductive Atomic Force Microscopy," *Materials,* vol. 12, no. 3, 2019.

[177] Nanoandmore. "CDT-NCHR." Nanoandmore.com. Accessed: Nov. 10, 2023 [Online]. Available: https://www.nanoandmore.com/AFM-Probe-CDT-NCHR.

[178] F. Hui, P. Vajha, Y. Ji, C. Pan, E. Grustan-Gutierrez, H. Duan, P. He, G. Ding, Y. Shi, and M. Lanza, "Variability of Graphene Devices Fabricated Using Graphene Inks: Atomic Force Microscope Tips," *Surface and Coatings Technology,* vol. 320, pp. 391-395, 2017.

[179] C. A. Peterson, R. K. Workman, D. Sarid, B. Vermeire, H. G. Parks, D. Adderton, and P. Maivald, "Effects of Moisture on Fowler–Nordheim Characterization of Thin Silicon-Oxide Films," *Journal of Vacuum Science & Technology A: Vacuum, Surfaces, and Films,* vol. 17, no. 5, pp. 2753-2758, 1999.

[180] ParkSystems. "Park NX-Hivac." Parksystems.com. Accessed: Nov. 10, 2023 [Online]. Available: https://www.parksystems.com/products/high-vacuum-afm/park-nx-hivac.

[181] Hitachi High-Tech. "Environment Control Unit AFM5300E." Hitachi-hightech.com. Accessed: Nov. 10, 2023 [Online]. Available: https://www.hitachi-hightech.com/global/en/products/microscopes/spm-afm/units/afm5300e.html.

[182] C. Wen, A. G. Banshchikov, Y. Y. Illarionov, W. Frammelsberger, T. Knobloch, F. Hui, N. S. Sokolov, T. Grassser, and M. Lanza, "Dielectric Properties of Ultrathin CaF_2 Ionic Crystals," *Advanced Materials,* vol. 32, no. 34, p. 2002525, 2020.

[183] M. Lanza, M. Porti, M. Nafría, X. Aymerich, G. Benstetter, E. Lodermeier, H. Ranzinger, G. Jaschke, S. Teichert, L. Wilde, and P. Michalowski, "Crystallization and Silicon Diffusion Nanoscale Effects on the Electrical Properties of Al_2O_3 Based Devices," *Microelectronic Engineering,* vol. 86, no. 7-9, pp. 1921-1924, 2009.

[184] M. Lanza, M. Porti, M. Nafría, X. Aymerich, G. Benstetter, E. Lodermeier, H. Ranzinger, G. Jaschke, S. Teichert, L. Wilde, and P. Michalowski "Conductivity and Charge Trapping after Electrical Stress in Amorphous and Polycrystalline Al_2O_3-Based Devices Studied with AFM-Related Techniques," *IEEE Transactions on Nanotechnology,* vol. 10, no. 2, pp. 344-351, 2010.

[185] Y. Shi, Y. Ji, H. Sun, F. Hui, J. Hu, Y. Wu, J. Fang, H. Lin, J. Wang, H. Duan, and M. Lanza, "Nanoscale Characterization of PM2. 5 Airborne Pollutants Reveals High Adhesiveness and Aggregation Capability of Soot Particles," *Scientific Reports,* vol. 5, no. 1, p. 11232, 2015.

[186] Nanoandmore. "SCM-PIT." Nanoandmore.com. Accessed: Nov. 10, 2023 [Online]. Available: https://www.nanoandmore.com/eu/AFM-Probe-SCM-PIT?gclid=CjwKCAiAxreqBhAxEiwAfGfndJveXnqntzkq69YWPJenV6XMQrbks8N-BV8onNCH33uWiJ9Dy06XJxoCM28QAvD_BwE.

[187] Y. Ji, F. Hui, Y. Shi, T. Han, Y. Song, C. Pan, and M. Lanza, "Note: Fabrication of a Fast-Response and User-Friendly Environmental Chamber for Atomic Force Microscopes," *Review of Scientific Instruments,* vol. 86, no. 10, 2015.

[188] F. Houzé, R. Meyer, O. Schneegans, and L. Boyer, "Imaging the Local Electrical Properties of Metal Surfaces by Atomic Force Microscopy With Conducting Probes," *Applied Physics Letters,* vol. 69, no. 13, pp. 1975-1977, 1996.

[189] I. Infante, F. Sánchez, V. Laukhin, A. Pérez del Pino, J. Foncuberta, K. Bouzehouane, S. Fusil, and A. Barthélémy, "Functional Characterization of $SrTiO_3$ Tunnel Barriers by Conducting Atomic Force Microscopy," *Applied Physics Letters,* vol. 89, no. 17, 2006.

[190] L. A. Félix, M. Sirena, L. A. Agüero Guzmán, J. González Sutter, S. Pons Vargas, L. B. Steren, R. Bernard, J. Trastoy, J. E. Villegas, and J. Briático,

"Structural and Electrical Characterization of Ultra-Thin $SrTiO_3$ Tunnel Barriers Grown over $YBa_2Cu_3O_7$ Electrodes for the Development of High Tc Josephson Junctions," *Nanotechnology,* vol. 23, no. 49, p. 495715, 2012.

[191] M. Lanza, A. Bayerl, T. Gao, M. Porti, M. Nafría, G. Y. Jing, Y. F. Zhang, Z. F. Liu, and H. L. Duan, "Graphene-Coated Atomic Force Microscope Tips for Reliable Nanoscale Electrical Characterization," *Advanced Materials (Deerfield Beach, Fla.),* vol. 25, no. 10, pp. 1440-1444, 2012.

[192] Y. Shi, Y. Ji, F. Hui, V. Iglesias, M. Porti, M. Nafría, E. Miranda, G. Bersuker, and M. Lanza, "Elucidating the Origin of Resistive Switching in Ultrathin Hafnium Oxides Through High Spatial Resolution Tools," *ECS Transactions,* vol. 64, no. 14, p. 19, 2014.

[193] L. Aguilera, M. Lanza, A. Bayerl, M. Porti, M. Nafría, and X. Aymerich, "Development of a Conductive Atomic Force Microscope with a Logarithmic Current-to-Voltage Converter for the Study of Metal Oxide Semiconductor Gate Dielectrics Reliability," *Journal of Vacuum Science & Technology B: Microelectronics and Nanometer Structures Processing, Measurement, and Phenomena,* vol. 27, no. 1, pp. 360-363, 2009.

[194] F. Palumbo, X. Liang, B. Yuan, Y. Shi, F. Hui, M. A. Villena, and M. Lanza, "Bimodal Dielectric Breakdown in Electronic Devices Using Chemical Vapor Deposited Hexagonal Boron Nitride as Dielectric," *Advanced Electronic Materials,* vol. 4, no. 3, p. 1700506, 2018.

[195] J. Xu, J. Xu, P. Zhang, W. Li, and K. Chen, "Nanoscale Quantification of Charge Injection and Transportation Process in Si-Nanocrystal Based Sandwiched Structure," *Nanoscale,* vol. 5, no. 20, pp. 9971-9977, 2013.

[196] J.-C. Bolsée, W. D. Oosterbaan, L. Lutsen, D. Vanderzande, and J. Manca, "CAFM on Conjugated Polymer Nanofibers: Capable of Assessing One Fiber Mobility," *Organic Electronics,* vol. 12, no. 12, pp. 2084-2089, 2011.

[197] W. Frammelsberger, G. Benstetter, J. Kiely, and R. Stamp, "C-AFM-Based Thickness Determination of Thin and Ultra-Thin SiO_2 Films by Use of Different Conductive-Coated Probe Tips,", *Appl Surf Sci,* vol. 253, no. 7, pp. 3615-3626, 2007.

[198] M. Lanza, M. Porti, M. Nafría, G. Benstetter, W. Frammelsberger, H. Ranzinger, E. Lodermeier, and G. Jaschke, "Influence of the Manufacturing Process on the Electrical Properties of Thin (< 4 nm) Hafnium Based High-K Stacks Observed With CAFM," *Microelectronics Reliability,* vol. 47, no. 9-11, pp. 1424-1428, 2007.

[199] L. Larcher, F. M. Puglisi, A. Padovani, L. Vandelli, and P. Pavan, "Multiscale Modeling of Electron-Ion Interactions for Engineering Novel Electronic Devices and Materials," in *2016 26th International Workshop on Power and Timing Modeling, Optimization and Simulation (PATMOS),* 2016: IEEE, pp. 128-132.

[200] A. Padovani, L. Larcher, F. M. Puglisi, and P. Pavan, "Multiscale Modeling of Defect-Related Phenomena in High-K Based Logic and Memory Devices," in *2017 IEEE 24th International Symposium on the Physical and Failure Analysis of Integrated Circuits (IPFA),* 2017: IEEE, pp. 1-6.

[201] H. Wu and L. S. Wang, "Electronic Structure of Titanium Oxide Clusters: TiO_y ($y= 1-3$) and $(TiO_2)_n$ ($n= 1-4$)," *The Journal of Chemical Physics,* vol. 107, no. 20, pp. 8221-8228, 1997.

[202] Y. C. Nah, I. Paramasivam, and P. Schmuki, "Doped TiO_2 and TiO_2 Nanotubes: Synthesis and Applications," *ChemPhysChem,* vol. 11, no. 13, pp. 2698-2713, 2010.

[203] D. Mardare and G. Rusu, "Comparison of the Dielectric Properties for Doped and Undoped TiO_2 Thin Films," *Journal of Optoelectronics and Advanced Materials,* vol. 6, no. 1, pp. 333-336, 2004.

[204] C. Pan and T. Ma, "Work Function of In_2O_3 Film as Determined From Internal Photoemission," *Applied Physics Letters,* vol. 37, no. 8, pp. 714-716, 1980.

[205] T. DiStefano and D. Eastman, "The Band Edge of Amorphous SiO_2 by Photoinjection and Photoconductivity Measurements," *Solid State Communications,* vol. 9, no. 24, pp. 2259-2261, 1971.

[206] M. Morales-Acosta, M. Quevedo-Lopez, H. N. Alshareef, B. E. Gnade, and R. Ramírez-Bon, "Dielectric Properties of PMMA-SiO_2 Hybrid Films," in *Materials Science Forum,* 2010, vol. 644: Trans Tech Publ, pp. 25-28.

[207] B. Cappella and G. Dietler, "Force-Distance Curves by Atomic Force Microscopy," *Surface Science Reports,* vol. 34, no. 1-3, pp. 1-104, 1999.

[208] Azom Materials. "Platinum (Pt) - Properties, Applications." Azom.com. Accessed: Nov. 16, 2023 [Online]. Available: https://www.azom.com/article.aspx?ArticleID=9235.

[209] Azom Materials. "Titanium Dioxide - Titania (TiO_2)." Azom.com. Accessed: Nov. 16, 2023 [Online]. Available: https://www.azom.com/properties.aspx?ArticleID=1179.

[210] O. Pirrotta, L. Larcher, M. Lanza, A. Padovani, M. Porti, M. Nafría, and G. Bersuker, "Leakage Current Through the Poly-Crystalline HfO_2: Trap Densities at Grains and Grain Boundaries," *Journal of Applied Physics,* vol. 114, no. 13, p. 134503, 2013.

[211] F. Ambrosio, G. Miceli, and A. Pasquarello, "Electronic Levels of Excess Electrons in Liquid Water," *The Journal of Physical Chemistry Letters,* vol. 8, no. 9, pp. 2055-2059, 2017.

[212] J. V. Coe, A. D. Earhart, M. H. Cohen, G. J. Hoffman, H. W. Sarkas, and K. H. Bowen, "Using Cluster Studies to Approach the Electronic Structure of Bulk Water: Reassessing the Vacuum Level, Conduction Band Edge, and Band Gap of Water," *The Journal of Chemical Physics,* vol. 107, no. 16, pp. 6023-6031, 1997.

[213] J. Kolb, Y. Minamitani, S. Xiao, X. Lu, M. Laroussi, R. P. Joshi, K. H. Schoenbach, E. Schamiloglu, and J. Gaudet, "The Permittivity of Water Under High Dielectric Stress," in *2005 IEEE Pulsed Power Conference,* 2005: IEEE, pp. 1266-1269.

[214] U. Celano, F.-C. Hsia, D. Vanhaeren, K. Paredis, T. E. M. Nordling, J. G. Buijnsters, T. Hantschel, and W. Vandervorst, "Mesoscopic Physical Removal of Material Using Sliding Nano-Diamond Contacts," *Scientific Reports,* vol. 8, no. 1, pp. 1-10, 2018.

[215] S. Rahpeima, E. M. Dief, S. Ciampi, C. L. Raston, and N. Darwish, "Impermeable Graphene Oxide Protects Silicon From Oxidation," *ACS Applied Materials & Interfaces,* vol. 13, no. 32, pp. 38799-38807, 2021.

[216] S. H. Chang, S. B. Lee, D. Y. Jeon, S. J. Park, G. T. Kim, S. M. Yang, S. C. Chae, H. K. Yoo, B. S. Kang, M.-J. Lee, and T. W. Noh, "Oxide Double-Layer Nanocrossbar for Ultrahigh-Density Bipolar Resistive Memory," *Advanced Materials,* vol. 23, no. 35, pp. 4063-4067, 2011.

[217] Bruker. "NCHV-A." Brukerafmprobes.com. Accessed: Nov. 17, 2023 [Online]. Available: https://www.brukerafmprobes.com/p-3364-nchv-a.aspx.

[218] Q. Zhong, D. Inniss, K. Kjoller, and V. Elings, "Fractured Polymer/Silica Fiber Surface Studied by Tapping Mode Atomic Force Microscopy," *Surface Science Letters,* vol. 290, no. 1-2, pp. L688-L692, 1993.

[219] S. Huang and Y. Tian, "Study on Characterization Methods of Tip Radius of AFM Worn Probe," in *2022 IEEE International Conference on Manipulation, Manufacturing and Measurement on the Nanoscale (3M-NANO),* 2022: IEEE, pp. 289-294.

[220] K. S. Novoselov, D. Jiang, F. Schedin, T. J. Booth, V. V. Khotkevich, S. V. Morozov, and A. K. Geim, "Two-Dimensional Atomic Crystals," *Proceedings of the National Academy of Sciences,* vol. 102, no. 30, pp. 10451-10453, 2005.

[221] S. Chen, M. R. Mahmoodi, Y. Shi, C. Mahata, B. Yuan, X. Liang, C. Wen, F. Hui, D. Akinwande, D. B. Strukov, and M. Lanza, "Wafer-Scale Integration of Two-Dimensional Materials in High-Density Memristive Crossbar Arrays for Artificial Neural Networks," *Nature Electronics,* vol. 3, no. 10, pp. 638-645, 2020.

[222] E. A. Irene, "Ultra-Thin SiO_2 Film Studies: Index, Thickness, Roughness and the Initial Oxidation Regime," *Solid-State Electronics,* vol. 45, no. 8, pp. 1207-1217, 2001.

[223] W. Wu, L. Wang, Y. Li, F. Zhang, L. Lin, S. Niu, D. Chenet, X. Zahng, Y. Hao, T. F. Heinz, J. Hone, and Z. L. Wang, "Piezoelectricity of Single-Atomic-Layer MoS_2 for Energy Conversion and Piezotronics," *Nature,* vol. 514, no. 7523, pp. 470-474, 2014.

[224] V. V. Korolkov, A. Summerfield, A. Murphy, D. B. Amabilino, K. Watanabe, T. Taniguchi, and P. H. Beton, "Ultra-High Resolution Imaging of Thin Films and Single Strands of Polythiophene Using Atomic Force Microscopy," *Nature Communications,* vol. 10, no. 1, p. 1537, 2019.

[225] Y. L. Lyubchenko, "Preparation of DNA and Nucleoprotein Samples for AFM Imaging," *Micron,* vol. 42, no. 2, pp. 196-206, 2011.

[226] Y. Xiao, W. Zheng, B. Yuan, C. Wen, and M. Lanza, "Highly Accurate Thickness Determination of 2D Materials," *Crystal Research and Technology,* vol. 56, no. 6, p. 2100056, 2021.

[227] R. Garcia, A. W. Knoll, and E. Riedo, "Advanced Scanning Probe Lithography," *Nature Nanotechnology,* vol. 9, no. 8, pp. 577-587, 2014.

[228] F. Palumbo, C. Wen, S. Lombardo, S. Pazos, F. Aguirre, M. Eizenberg, F. Hui, and M. Lanza, "A Review on Dielectric Breakdown in Thin Dielectrics: Silicon Dioxide, High-K, and Layered Dielectrics," *Advanced Functional Materials,* vol. 30, no. 18, p. 1900657, 2020.

[229] M. Porti, L. Aguilera, X. Blasco, M. Nafrı, and X. Aymerich, "Reliability of SiO_2 and High-K Gate Insulators: A Nanoscale Study with Conductive Atomic Force Microscopy," *Microelectronic Engineering,* vol. 84, no. 3, pp. 501-505, 2007.

[230] X.-D. Dang, M. Dante, and T.-Q. Nguyen, "Morphology and Conductivity Modification of Poly (3, 4-Ethylenedioxythiophene): Poly (Styrene Sulfonate) Films Induced by Conductive Atomic Force Microscopy Measurements," *Applied Physics Letters,* vol. 93, no. 24, 2008.

[231] O. Douhéret, L. Lutsen, A. Swinnen, M. Breslge, K. Vandwal, L. Goris, and J. Manca, "Nanoscale Electrical Characterization of Organic Photovoltaic Blends by Conductive Atomic Force Microscopy," *Applied Physics Letters,* vol. 89, no. 3, 2006.

[232] S. Besendörfer, E. Meissner, F. Medjdoub, J. Derluyn, J. Friedrich, and T. Erlbacher, "The Impact of Dislocations on AlGaN/GaN Schottky Diodes and on Gate Failure of High Electron Mobility Transistors," *Scientific Reports,* vol. 10, no. 1, p. 17252, 2020.

[233] F. Giannazzo, G. Greco, S. Di Franco, P. Fiorenza, I. Deretzis, A. La Magna, C. Bongiorno, M. Zombone, F. La Via, M. Zielinski, and F. Roccaforte, "Impact of Stacking Faults and Domain Boundaries on the Electronic Transport in Cubic Silicon Carbide Probed by Conductive Atomic Force Microscopy," *Advanced Electronic Materials*, vol. 6, no. 2, p. 1901171, 2020.

[234] F. Giannazzo, S. E. Panasci, E. Schilirò, G. Greco, F. Roccaforte, G. Sfuncia, G. Nicotra, M. Cannas, S. Agnello, E. Frayssinet, Y. Cordier, A. Michon, A. Koos, and B. Pécz, "Atomic Resolution Interface Structure and Vertical Current Injection in Highly Uniform MoS_2 Heterojunctions with Bulk GaN," *Appl Surf Sci*, vol. 631, p. 157513, 2023.

[235] F. Giannazzo, E. Schilirò, G. Greco, and F. Roccaforte, "Conductive Atomic Force Microscopy of Semiconducting Transition Metal Dichalcogenides and Heterostructures," *Nanomaterials*, vol. 10, no. 4, p. 803, 2020.

[236] C. R. Peiris, S. Ferrie, S. Ciampi, W. D. Rickard, and N. Darwish, "Memristor Arrays Formed by Reversible Formation and Breakdown of Nanoscale Silica Layers on Si–H Surfaces," *ACS Applied Nano Materials*, vol. 5, no. 5, pp. 6609-6617, 2022.

[237] Y. Zhang, Y. Miyahara, N. Derriche, W. Yang, K. Yazda, X. Capaldi, Z. Liu, P. Grutter, and W. Reisner, "Nanopore Formation via Tip-Controlled Local Breakdown Using an Atomic Force Microscope," *Small Methods*, vol. 3, no. 7, p. 1900147, 2019.

[238] M. R. Nellist, Y. Chen, A. Mark, S. Gödrich, C. Stelling, J. Jiang, R. Poddar, C. Li, R. Kumar, G. Papastavrou, M. Retsch, B. S. Brunschwig, Z. Huang, C. Xiang, and S. W. Boettcher, "Atomic Force Microscopy With Nanoelectrode Tips for High Resolution Electrochemical, Nanoadhesion and Nanoelectrical Imaging," *Nanotechnology*, vol. 28, no. 9, p. 095711, 2017.

[239] F. Nardi, D. Deleruyelle, S. Spiga, C. Muller, B. Bouteille, and D. Ielmini, "Switching of Nanosized Filaments in NiO by Conductive Atomic Force Microscopy," *Journal of Applied Physics*, vol. 112, no. 6, 2012.

[240] Bruker. "ScanAsyst-Air." Brukerafmprobes.com. Accessed: Nov. 18, 2023 [Online]. Available: https://www.brukerafmprobes.com/p-3726-scanasyst-air.aspx.

[241] P. Mur, M. N. Semeria, M. Olivier, A. M. Papon, C. Leroux, G. Reimbold, P. Gentile, N. Magnea, T. Baron, R. Clerc, and G. Ghibaudo, "Ultra-Thin Oxides Grown on Silicon (1 0 0) by Rapid Thermal Oxidation for CMOS and Advanced Devices," *Appl Surf Sci*, vol. 175, pp. 726-733, 2001.

[242] M. Maestro-Izquierdo, M. Gonzalez, F. Campabadal, J. Suñe, and E. Miranda, "A New Perspective Towards the Understanding of the Frequency-Dependent Behavior of Memristive Devices," *IEEE Electron Device Letters*, vol. 42, no. 4, pp. 565-568, 2021.

[243] R. Y. Tay, M. H. Griep, G. Mallick, S. H. Tsang, R. S. Singh, T. Tumlin, E. H. T. Teo, and S. P. Karna, "Growth of Large Single-Crystalline Two-Dimensional Boron Nitride Hexagons on Electropolished Copper," *Nano Letters*, vol. 14, no. 2, pp. 839-846, 2014.

[244] C. Ionescu-Zanetti, A. Mechler, S. A. Carter, and R. Lal, "Semiconductive Polymer Blends: Correlating Structure With Transport Properties at the Nanoscale," *Advanced Materials*, vol. 16, no. 5, pp. 385-389, 2004.

[245] J.-Y. Mao, L. Zhou, Y. Ren, J.-Q. Yang, C.-L. Chang, H.-C. Lin, H.H. Chou, S.-R. Zhang, Y. Zhou, and S.-T. Han, "A Bio-Inspired Electronic Synapse Using Solution Processable Organic Small Molecule," *Journal of Materials Chemistry C*, vol. 7, no. 6, pp. 1491-1501, 2019.

[246] Onsemi. "BSS138L, BVSS138L." Onsemi.com. Accessed: Nov. 27, 2023 [Online]. Available: https://www.onsemi.com/pdf/datasheet/bss138lt1-d.pdf.

B List of Abbreviations

°C	Degree Celsius
2D	Two-Dimensional
3C-SiC	Cubic Silicon Carbide
3D	Three-Dimensional
A^{**}	Effective Richardson Constant
A_C	Contact Area
A_{eff}	Electrically Effective Area
$A_{eff,PFTUNA}$	Electrically Effective Area PFTUNA
$A_{eff,SCM-PIT}$	Electrically Effective Area SCM-PIT
AFM	Atomic Force Microscopy
Ag	Silver
AHI	Anode Hole Injection
AHR	Anode Hydrogen Release
AI	Artificial Intelligence
ALD	Atomic Layer Deposition

AlGaN/GaN	Aluminium Gallium Nitride / Gallium Nitride
AlO_x	Aluminum Oxide
AM-AFM	Amplitude Modulation Atomic Force Microscopy
Au	Gold
B_4C	Boron Carbide
C-AFM	Conductive Atomic Force Micrsocopy
CCS	Constant Current Stress
CMOS	Complementary Metal-Oxide Semiconductor
CoCr	Cobalt Chromium
Cu	Copper
CuO_x	Copper Oxide
CVD	Chemical Vapor Deposition
CVS	Constant Voltage Stress
DB	Dielectric Breakdown
DMT	Derjaguin Muller Toporov Model

d_{ox}	Oxide Thickness
DS	Deflection Setpoint
E_1	Elasticity Modulus Tip
$E_{1,Pt}$	Elasticity Modulus Platinum
E_2	Elasticity Modulus Tip
E_{2,TiO_2}	Elasticity Modulus Titanium Dioxide
E_C	Conduction Band
E_F	Fermi Level
E_g	Band Gap
E_{g,H_2O}	Band Gap Water
E_m	Electrical Field Maximum
E_{ox}	Electrical Field Across the Oxide
E_V	Valence Band
$F(t_B)$	Cumulative Failure Probability
F_c	Contact Force
FIB	Focused Ion Beam
FinFETs	Fin Field Effect Transistors

FM-AFM	Frequency Modulation Atomic Force Microscopy
FN	Fowler Nordheim Tunneling
GAA	Gate-All-Around
Ge	Germanium
H_2O	Water
HBD	Hard Breakdown
h-BN	Hexagonal Boron Nitride
HfO_x	Hafnium Oxide
HSDC	High-Speed Data Capture
I	Current
I_0	Schottky Saturation current
I_{FNT}	Fowler Nordheim Tunneling Current
IoT	Internet of Things
k	Boltzmann Constant
K	Reduced Young’s Modulus
K_C	Spring Constant
$K_{C,NOM}$	Nominal Spring Constant

$K_{C,SCM-PIT}$	Spring Constant PFTUNA Probe
$K_{C,SCM-PIT}$	Spring Constant SCM-PIT Probe
KOH	Potassium Hydroxide
LPCVD	Low Pressure Chemical Vapor Deposition
M	Mean Value
m_e	Free Electron Mass
MoS_2	Molybdenum Disulfide
m_{ox}	Effective Charge Carrier Mass in the Oxide
N	Semiconductor Doping Density
n	Electron Concentration in the Conduction Band of Electrons at Trap Sites
NA	Numerical Aperture
N_{CV}	Density of States
Ni	Nickel
NiO	Nickel Oxide
PCB	Printed Circuit Board
R_z	Resolution Limit for Optical Systems in z
PEALD	Plasma Enhanced Atomic Layer Deposition
Pt	Platinum
Pt/Ir	Platinum Iridium
PtSi	Platinum Silicide
q	Electron charge
r_C	Radius of the Contact Area
$R_{DS(ON)}$	Drain Source Resistance in the ON State
RF	Radio Frequency
RH	Relative Humidity
RMS	Root Mean Squared
R_{TIP}	Tip Radius
$R_{TIP,NOM}$	Nominal Tip Radius
$R_{TIP,PFTUNA}$	Tip Radius PFTUNA
$R_{TIP,SCM-PIT}$	Tip Radius SCM-PIT
RVS	Ramped Voltage Stress

TiO_2	Titanium Dioxide
SBD	Soft Breakdown
SD	Standard Deviation
Si	Silicon
Si_3N_4	Silicon Nitride
SiGe	Silicon Germanium
SiO_2	Silicon Dioxide
SiO_x	Silicon Oxide
SPA	Semiconductor Parameter Analyzer
SPM	Scanning Probe Microscope
STM	Scanning Tunneling Microscope
T	Absolute Temperature
TaO_x	Tantalum Oxide
t_B	Time to Breakdown
TEM	Transmission Electron Microscope
Ti	Titanium
$Ti(NMe_2)_4$	Tetrakis(dimethylamido) titanium
$R_{x,y}$	Resolution Limit for Optical Systems in x and y
TiN	Titanium Nitride
TiO_x	Titanium Oxide
t_{MoS_2}	MoS_2 Step Height
TUNA	Tunneling Atomic Force Microscope
UHV	Ultra-High Vacuum
UV	Ultraviolet
V_{bi}	Build in Voltage
V_f	Forward Bias
V_{MAX}	Maximum Voltage
$-V_{MAX}$	Maximum Negative Voltage
V_{on}	Onset Potential
V_{ox}	Voltage Across the Oxide
V_r	Reverse Bias
V_{STOP}	Stop Voltage
WC	Tungsten Carbide
ZnO_x	Zinc Oxide
ZrO_x	Zirconium Oxide

C List of Symbols

α	Mean Spacing Between Trap Sites
α_B	Time-to-Breakdown at Approximately 63 % Breakdown Occurrence
α_l	Cone Half Angle of Light from the Specimen Plane Accepted by the Objective
β	Weibull Shape Parameter
δ_c	Cantilever Deflection
ΔE_a	Carrier Activation Energy
$\Delta E_{a,t}$	Carrier Activation Energy From Trap States to the Bottom of the Conduction Band
ε_{H_2O}	Dielectric Permittivity Water
ϵ_{ox}	Permittivity of the Oxide
ϵ_s	Semiconductor Permittivity
η	Ideality Factor

η_R	Index of Refraction between Point Source and Lens, Relative to Free Space
$\eta \cdot \sin \alpha_l$	Numerical Aperture (NA)
λ	Wavelength of Light
μ	Charge Carrier Mobility
ν_1	Poisson Ratio Tip
$\nu_{1,Pt}$	Poisson Ratio Platinum
ν_2	Poisson Ratio Sample
ν_{2,TiO_2}	Poisson Ratio Titanium Dioxide
v	Frequency of the Thermal Vibration of Electrons at Trap Sites
φ_{H_2O}	Electron Affinity Water
ϕ_B	Barrier Height

Φ_m	Metal Work Function			
χ	Electron Affinity			
ħ	Reduced Planck’s Constant			

D List of Tables

E List of Figures

F Acknowledgements

First and foremost, I would like to thank my director Prof. Dr. Mario Lanza Martinez, who not only inspired me to embark on the Ph.D. journey but also provided the opportunity for me to do so. His guidance was a beacon throughout the challenging path of doctoral research. He offered me vital support whenever needed, but also granted me the freedom to explore my own ideas. Despite his busy schedule, he consistently made time to discuss my results and suggest innovative approaches when experiments did not go as planned. Moreover, he provided me with the opportunity to spend a year at the King Abdullah University of Science and Technology (KAUST) in Saudi Arabia, not only granting me access to cutting-edge technology and laboratories but also allowing me to collaborate with an exceptional team. This experience not only improved my technical skills, but it also expanded my horizons by working in such an international environment and fostering friendships, that will endure well beyond my studies. His dedication and work ethic stand as a model of exemplary professorship. I am deeply grateful for his mentorship and feel privileged to have been his student.

I would also like to extend my heartfelt gratitude to my team leader at Deggendorf Institute of Technology (DIT) Prof. Dr. Günther Benstetter. His lecture on “Selected Topics of Micro and Nanoelectronics” was instrumental in steering my focus toward this fascinating field. By providing me with positions, first as a working student and later as a scientific employee, Prof. Dr. Benstetter played a crucial role in paving the way for my Ph.D. journey. I am immensely grateful for his expertise, continuous support, and his kind and approachable leadership style.

Furthermore, I would like to thank my tutor at the University of Barcelona, Prof. Dr. Juan Marcos Fernandez Pradas. His swift and kind responses were invaluable whenever I found myself lost in the intricate administrative aspects of the Ph.D. program at the University of Barcelona. His guidance and efficient coordination were instrumental in keeping me on track. I am deeply grateful for his support and assistance throughout my program.

Additionally, I would like to express my sincere appreciation to Prof. Dr. Werner Frammelsberger from DIT, who, in familiar fashion, supported me through this thesis in a reliable, kind, and prompt manner. Thank you very much for encouraging me, sharing your own Ph.D. insights, and especially all the productive discussions towards the first paper.

Moreover, I would like to thank my team at DIT, consisting of my fellow Ph.D. students Christoph Metzke and Fabian Kühnel, our laboratory engineers Heiko Ranzinger and Edgar Lodermeier, our scientific employees Bidyut Saha and Ammar Alahmad, and our master student Fabian Zak for their all-time helpful and friendly support. Thank you for all the engaging discussions, the collective struggle in repairing equipment malfunctions, and the camaraderie that brought life and energy to our office atmosphere.

Finally, I wish to convey my heartfelt gratitude to my colleagues at KAUST, including our Postdoctoral Fellows Sebastian Pazos, Marco Vilena, and Kaichen Zhu, as well as our Ph.D. Students Osamah Alharbi, Yue Yuan, Wenwen Zheng, Yaqing Shen, and Yue Ping. My time at KAUST was an enriching learning experience, and thanks to you all, even long hours in the office were a pleasure. I am immensely thankful for the warm welcome and the wonderful times we shared inside and outside of the office's walls.

G Scientific vita

Personal data

Name: Jonas Weber

Address: Spitalhofstr. 22a
94032 Passau

Phone: +49 178/1479759

E-Mail: jonas.weber1991@gmail.com

Birthdate/ -place: 19th of October 1991,
Nuremberg

Nationality: German

Languages: German (Native), English

Work Experience

Since 08/2023	Deggendorf Institute of Technology (DIT) Faculty of Electrical Engineering and Information Technology Scientific employee (100%)
07/2020 – 06/2022	Deggendorf Institute of Technology (DIT) Project AlhoiS - Scientific employee (100%)
10/2019 – 06/2022	Deggendorf Institute of Technology (DIT) Lecturer for Micro & Nanoelectronics
10/2018 – 08/2020	Deggendorf Institute of Technology (DIT) Project TRIO - Scientific employee (50%)

Education

Since 03/19	PhD in Nanoscience University of Barcelona, Spain
10/2016 – 07/2018	Master in Electrical Engineering & Information Technology Deggendorf Institute of Technology (DIT), Germany
10/2011 – 03/2016	Bachelor in Mechatronics Deggendorf Institute of Technology (DIT), Germany

International Experience

07/2022 – 07/2023	Consultant King Abdullah University of Science and Technology (KAUST), Kingdom of Saudi Arabia
10/2017 – 04/2018	Visiting Master Student Soochow University, China

Journal Publications

Weber, J., Yuan, Y., Pazos, S., Kühnel, F., Metzke, C., Schätz, J., Frammelsberger, W., Benstetter, G. & Lanza, M. (2023). Current-Limited Conductive Atomic Force Microscopy. *ACS Applied Materials & Interfaces 15* (48), 56365-56374.

Hui, F., Zhang, C., Yu, H., Han, T., **Weber, J.**, Shen, Y., Xiao, Y., Li, X., Zhang, Z. & Liu, P. (2023). Self-Assembly of Janus Graphene Oxide via Chemical Breakdown for Scalable High-Performance Memristors. *Advanced Functional Materials*, 2302073.

Weber, J., Yuan, Y., Kühnel, F., Metzke, C., Schätz, J., Frammelsberger, W., Benstetter, G. & Lanza, M. (2023). Solid Platinum Nanoprobes for Highly Reliable Conductive Atomic Force Microscopy. *ACS Applied Materials & Interfaces*, *15*(17), 21602-21608.

Kühnel, F., Metzke, C., **Weber, J.**, Schätz, J., Duesberg, G. S., & Benstetter, G. (2022). Investigation of heater structures for thermal conductivity measurements of SiO2 and Al2O3 thin films using the 3-omega method. *Nanomaterials*, *12*(11), 1928.

Metzke, C., Kühnel, F., **Weber, J.**, & Benstetter, G. (2021). Scanning thermal microscopy of ultrathin films: Numerical studies regarding cantilever displacement, thermal contact areas, heat fluxes, and heat distribution. *Nanomaterials*, *11*(2), 491.

Metzke, C., Frammelsberger, W., **Weber, J.**, Kühnel, F., Zhu, K., Lanza, M., & Benstetter, G. (2020). On the limits of scanning thermal microscopy of ultrathin films. *Materials*, *13*(3), 518.

Jiang, L., **Weber, J.**, Puglisi, F. M., Pavan, P., Larcher, L., Frammelsberger, W., Benstetter, G. & Lanza, M. (2019). Understanding current instabilities in conductive atomic force microscopy. *Materials*, *12*(3), 459.

Invited talks

02/2023	KAUST – BRUKER Scientific Forum Thuwal, Kingdom of Saudi Arabia

Reviewing

Since 10/2020	Reviewer Microelectronic Engineering by Elsevier

Conferences

06/2022	Nanobrücken 2022: Bruker Nanomechanical Testing Conference Poster contribution Prague, Czech Republic
10/2020	International Integrated Reliability Workshops (IIRW) 2020 Poster contribution online
06/2019	Nano Today 2019 Poster contribution Lisbon, Portugal

H Statutory Declaration

I hereby declare that I have written this dissertation independently without the help of third parties and without using any sources other than those indicated. All passages taken verbatim or in spirit from the sources used are identified as such individually.

This work has not been submitted to any other examination authority and has not been published.

I am aware that a false declaration will have legal consequences.

Deggendorf, 8th of January 2024

Jonas Weber

Place, date, signature